INERTIAL CONFINEMENT FUSION

Lawrence Livermore National Laboratory

ICF Semiannual Report *October 1999—March 2000, Volume 1, Number 1*

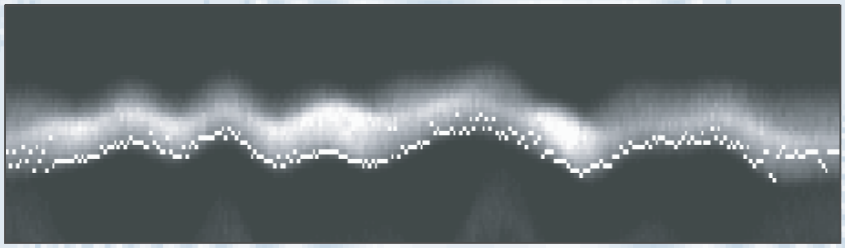

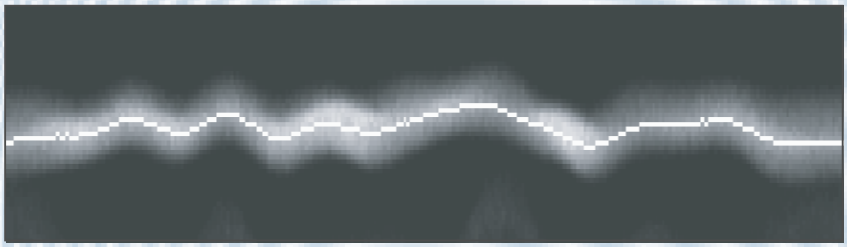

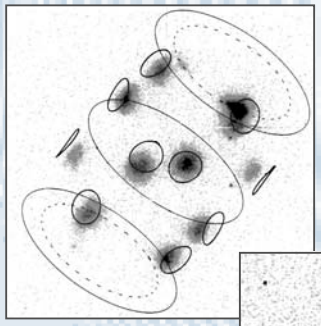

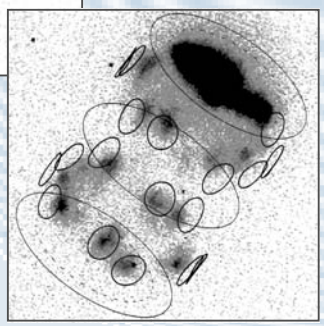

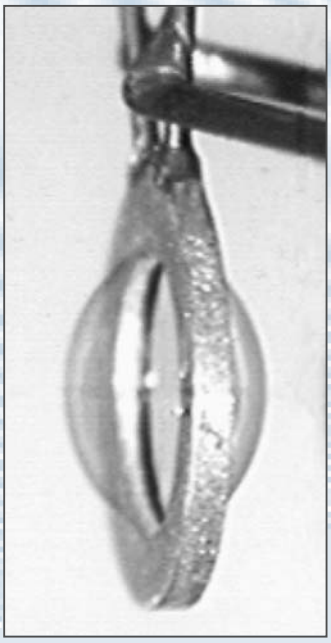

UCRL-LR-105821-00-1

The Cover: The two top figures (see p. 20) show the comparison between using a Gaussian-fit and edge-fit (bright thin lines) to map the location of the bright band (bright diffuse region) obtained in a simulated shadowgraph image from DT ice in a target capsule. Shadowgraphy is the primary technique currently in use to determine the roughness of the fuel ice layer in transparent shells. The edge-fit (upper figure) introduces significantly more noise into the modal analysis of the bright band as compared to the Gaussian-fit and therefore does not give an accurate representation of the ice roughness. The lower-right figure shows a Nova gasbag target (p. 36) that was used to produce a long-scalelength, high-density, and high-temperature plasma. This type of target provided a vast range of important atomic physics and plasma physics information. The lower-left figures (p. 44) show gated x-ray images (5 keV) at 0.8 ns (1.2 ns) of where the early (late) OMEGA laser beams are interacting with the wall plasma. The deviation of the x-ray spots from the original location of the beams (small circles) is due to wall motion. The rippling, satin-like background (p. 24) is a simulated transmission interferogram of a two-dimensionally rough fuel ice surface.

The *ICF Semiannual Report* is published by the Inertial Confinement Fusion (ICF) Program at the Lawrence Livermore National Laboratory. The journal reports selected current research within the ICF Program. Major areas of investigation include fusion target theory and design, target fabrication, target experiments, and laser and optical science and technology. In addition, the Laser Science and Technology program element of LLNL's NIF Programs serves as a source of expertise in developing laser and electro-optics capabilities in support of the ICF mission and goals and also develops new lasers for government and commercial applications. To keep our readers informed of these new capabilities, the *ICF Semiannual Report*, which replaces the *ICF Quarterly Report*, covers additional non-ICF funded, but related, laser research and development and associated applications. Succeeding issues of this journal will not be in print but will be posted on the ICF Program website. Questions and comments relating to the technical content of the journal should be addressed to ICF/NIF and HEDES Program, Lawrence Livermore National Laboratory, P.O. Box 808, L-475, Livermore, CA 94551.

On the Web:
http://www.llnl.gov/nif/icf.html

UCRL-LR-105821-00-1
October 1999–March 2000

Printed in the United States of America
Available from
National Technical Information Service
U.S. Department of Commerce
5285 Port Royal Road
Springfield, Virginia 22161
Price codes: printed copy A03, microfiche A01.

This work was performed under the auspices of the U.S. Department of Energy by University of California Lawrence Livermore National Laboratory under Contract No. W–7405–Eng–48.

INERTIAL CONFINEMENT FUSION

ICF Semiannual Report *October 1999–March 2000, Volume 1, Number 1*

In this issue:

Scientific Editor
John Moody

Publication Editor
Al Miguel

Designer
Stacy Bookless

Technical Editors
Jason Carpenter
Cindy Cassady
Al Miguel

Classification Editor
Roy Johnson

Art Staff
Clayton Dahlen
Stacy Bookless
Pam Davis
Amy Henke

Cover Design
Stacy Bookless

FOREWORD

This first issue of the *ICF Semiannual Report* contains articles whose diverse subjects attest to the broad technical and scientific challenges that are at the forefront of the ICF program at LLNL.

The first article describes the progress being made at solving the surface roughness problem on capsule mandrels. All NIF capsule options, except machined beryllium, require a mandrel upon which the ablator is deposited. This mandrel sets the baseline sphericity of the final capsule. Problems involving defects in the mandrel have been overcome using various techniques so that 2-mm-size mandrels can now be made that meet the NIF design specification.

The second article validates and provides a detailed numerical investigation of the shadowgraph technique currently used to diagnose the surface roughness of a fuel ice layer inside of a transparent capsule. It is crucial for the success of the indirect-drive ignition targets that the techniques used to characterize ice-surface roughness be well understood. This study identifies methods for analyzing the bright band that give an accurate measure of the ice-surface roughness.

The third article describes a series of realistic laser and target modifications that can lead to 3–4 times more energy coupling and 10 times greater yield from a NIF indirect-drive ignition target. Target modifications include using various mixtures of rare-earth and other high-Z metals as hohlraum wall material and adjusting the laser-entrance-hole size and the case-to-capsule size ratio. Each option is numerically examined separately and together.

The fourth article reviews how detailed x-ray and Thomson scattering measurements from a high-density and high-temperature gasbag plasma are used to test spectroscopic modeling techniques. There is good agreement between the model and experimental dielectronic capture satellite intensities. However, improvements are required in the modeling of inner shell collisionally populated satellite states. These improvements can have important implications for the interpretation of inertial confinement fusion capsule implosions.

The fifth article reports on experiments using the OMEGA laser that investigate symmetry control in hohlraums. The experiments explore a control method where different pointings are used for different groups of beams and the beams are staggered in time. This gives a dynamic beam pointing adjustment during the laser pulse. Measurements of the capsule symmetry show agreement with simulations and show the ability to control low-mode drive asymmetries.

The sixth article reports on the observation of an intense high-energy proton beam produced by irradiating a thin-foil target with the petawatt laser. This experiment is important for understanding new mechanisms of ion acceleration using high-intensity short-pulse lasers. Proton beams of the type observed here could be of interest for applications ranging from medicine to fast ignition.

John Moody
Target Ignition Physics Program
Scientific Editor

The Development of Plastic Mandrels for NIF Targets

Robert Cook *Masaru Takagi*

*Barry McQuillan** *Richard Stephens**

All National Ignition Facility (NIF) capsule options except machined Be require a mandrel upon which the ablator is deposited. This mandrel, a thin-walled plastic shell, sets the baseline sphericity of the final capsule, especially over the low modes. Subsequent ablator coating operations may degrade the capsule surface finish and are unlikely to improve it. For Nova capsules, the mandrels were historically ~0.5-mm-diam polystyrene thin-walled microshells produced by solution droptower methods.[1] However, these methods are limited to shell sizes of less than 1-mm diameter. In 1997, Lawrence Livermore National Laboratory and General Atomics began to explore the use of microencapsulation techniques to produce NIF-scale capsule mandrels. These techniques had been largely developed for inertial confinement fusion (ICF) capsule fabrication by researchers at Osaka University for small polystyrene shells;[2] however, the techniques were easily extended to produce shells with 2-mm diameters needed for the NIF. At issue was whether the required symmetry and sphericity could be achieved. The NIF capsule design sphericity specifications are essentially taken from the best sphericities achieved for Nova capsules.[3] Not only are the techniques to be used different, but the capsules are to be four times larger.

The basic microencapsulation process (see Figure 1) involves encapsulating a water droplet with a nonaqueous polymer

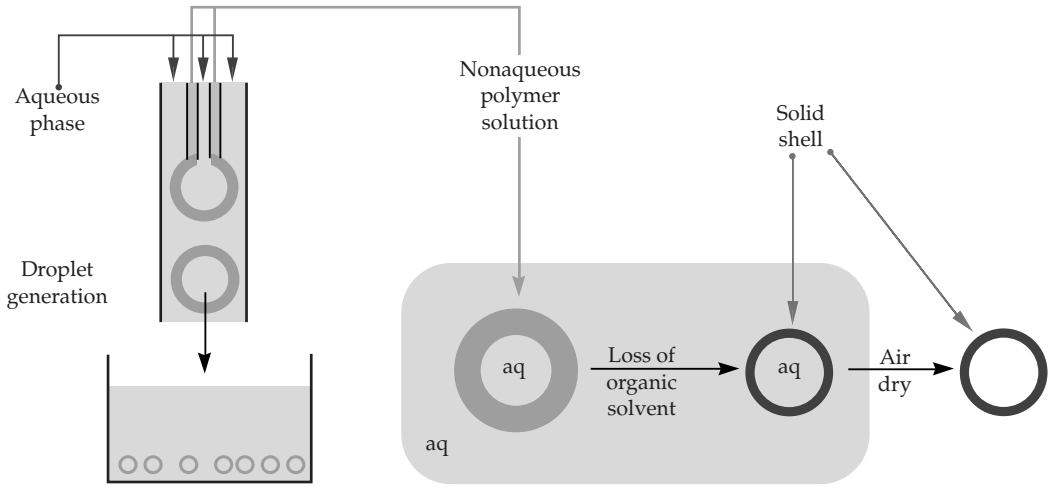

FIGURE 1. Cartoon of microencapsulation process. (NIF-0401-02076pb01)

*General Atomics

solution and suspending this encapsulated droplet in a stirred aqueous bath. During a multihour curing phase, the organic solvent slowly dissipates into the bath, leaving a solid polymer shell filled with water, which can be removed by slow air drying. Shells in the 2-mm-diam (or larger) size could be easily prepared; however, the quality of these shells did not satisfy the NIF specifications.

Figure 2 illustrates in cartoon fashion the types of defects, their manifestation in example atomic force microscope (AFM) equatorial traces of the shell, and the related effect on the surface power spectra.[4] First, shells had significant wall thickness variation, a nonconcentricity (NC) or P_1 defect that does not manifest itself in AFM traces, but which can affect subsequent fabrication steps, as well as a large mode-2 out-of-round. These lowest-mode asymmetries were thought to originate in the basic hydrodynamics of the curing process, coupled with density differences between the bath, oil phase, and inner water phase. Second, the mandrel surface also had significant amplitude in modes 10 to 50 (defects on length scales of 100s of microns). Wall thickness measurements generally showed these represented "ripples" in the wall rather than thickness variations. It was suspected that these defects had multiple causes: collisions of the mandrels with each other and/or the bath stirring device, surface distortions caused by large vacuoles (voids) within the mandrel wall, and some kind of modulated stress resulting

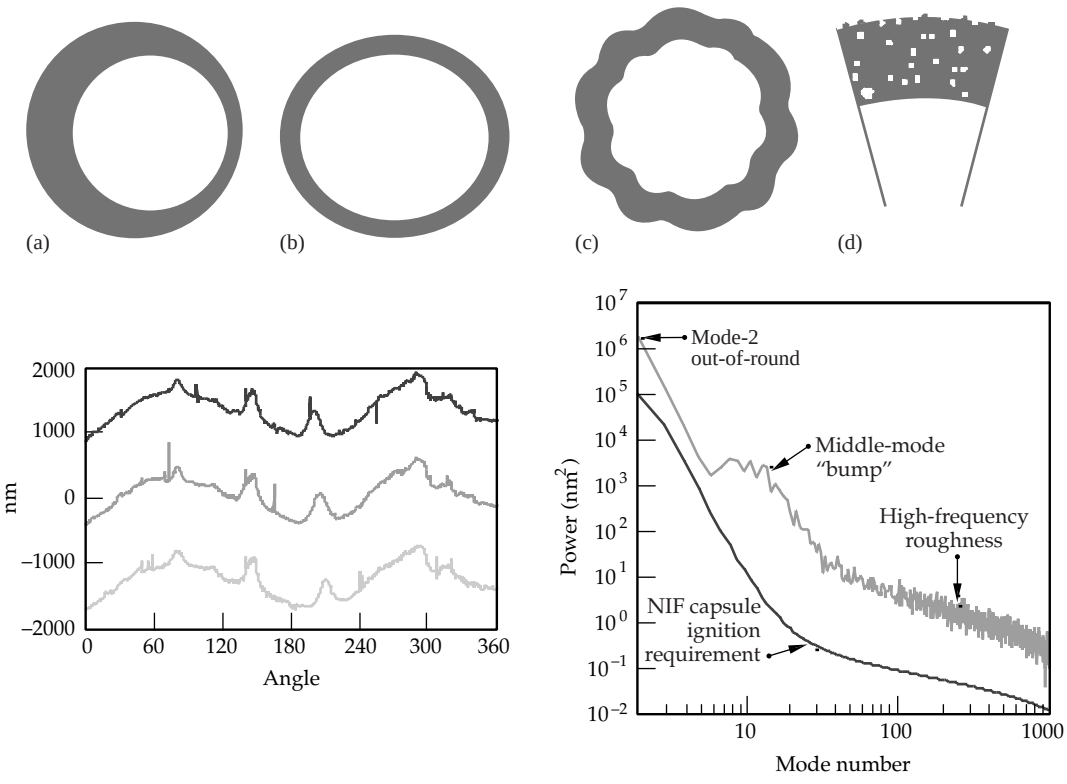

FIGURE 2. Shown at the top are exaggerated drawings of microencapsulated shell defects: (a) mode-1 wall thickness variation, (b) mode-2 out-of-round, (c) middle-mode roughness, and (d) high-frequency roughness due to surface debris and surface or near-surface vacuoles. Below left are example AFM SphereMapper traces (three parallel traces 40 μm apart). For a NIF shell, 1 degree represents about 17.5 μm of a surface trace. Thus the prominent features at about 75, 145, 210, and 290 degrees are "bumps" that are 0.2 to 0.4 μm high and 100s of μm wide. These give rise to the power over modes 10 to 50 in the power spectrum on the right. The features in the traces that appear as "narrow spikes" are due either to surface debris or surface vacuoles and are responsible for the high-frequency power.
(NIF-0401-02077pb01)

in shell wall buckling. Third, the shell surface had a rather high amplitude in modes >100. These high-frequency defects were due in part to surface debris and the presence of small-diam vacuoles in the polymer wall, some of which disrupted the surface.

In this article, we describe how these problems were overcome or at least reduced, so that we are now able to produce 2-mm mandrels that are beginning to meet the design specifications. Our objective is not to provide detailed procedures, but rather to discuss the scientific basis of the approaches we have taken and to document their effectiveness in meeting our objectives. In the final section, we summarize the current mandrel status.

Microencapsulation Method

The initial microencapsulated droplets are prepared using a triple orifice droplet generator.[5,6] As schematically shown in Figure 1, the innermost orifice that delivers pure water is inside a larger orifice that delivers a nonaqueous polymer solution resulting in the encapsulation of the inner droplet. This compound droplet is then stripped off the orifice by an outer aqueous flow that carries it into an aqueous bath. The compound droplet size is controlled by the rate of this flow and the orifice dimensions, while the relative amounts of inner water and oil phases, which determine the wall thickness, are precisely controlled by syringe pumps. NIF-scale shells can be generated at a rate of about 2.5 s^{-1}, and though metastable, are remarkably robust. They can, for instance, be squeezed down a tube whose inner diameter is ~20% smaller than the shell outside diameter (OD) without loss of the inner water phase. The typical batch size is about 3000 shells, and the variation in final diameter (~2000 μm) and wall thickness (~15 μm) within a batch is less than 0.5% and 3%, respectively. The polymer used in our work is poly(α-methylstyrene) (PαMS); its structure is shown in Figure 3. The polymer has a very narrow

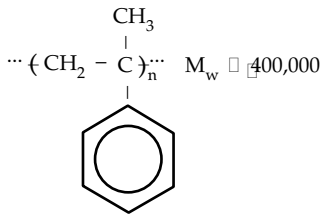

FIGURE 3. PαMS structure.
(NIF-0401-02078pb01)

molecular weight distribution centered at about 400,000. PαMS is used because it can be thermally decomposed to gaseous products at 300°C, a step in subsequent capsule preparation.[7] The polymer is dissolved in fluorobenzene, a solvent picked primarily for its reasonably close density match [ρ(25°C) = 1.024 g/cm^3] to the aqueous media. The aqueous bath and stripping fluid must contain a "protective colloid" to prevent interaction and agglomeration of the compound droplets. This has typically been about 2 wt% poly(vinyl alcohol) (PVA), but for reasons that will be discussed later, we currently use poly(acrylic acid) (PAA) at a much lower concentration.

Following droplet generation, the compound fluid shells must be agitated for some period of time to center the inner aqueous droplet in the oil shell. The exact mechanism of this centering is not well understood, but Norimatsu[8] has shown in model calculations that fluid droplet deformation causes core centering. Experimentally, we have found that centering can be achieved rapidly with various bath agitation methods. Initially, we used a simple open beaker with a stir propeller, but have since moved to a rotating drum device as pictured in Figure 4. This approach tumbles the shells very effectively, but at the same time more gently, giving higher batch yields of mandrels with very uniform walls and also allows us to easily control the rate of solvent loss from the fluid shells; that latter feature has important consequences as described later.

When the shells have cured, the interior water phase must be removed. Shells are put in 25% ethyl alcohol solution to create an osmotic pressure and diffuse some of the water out of the interior water phase. This water removal puts a compressive stress on the shell that will increase until

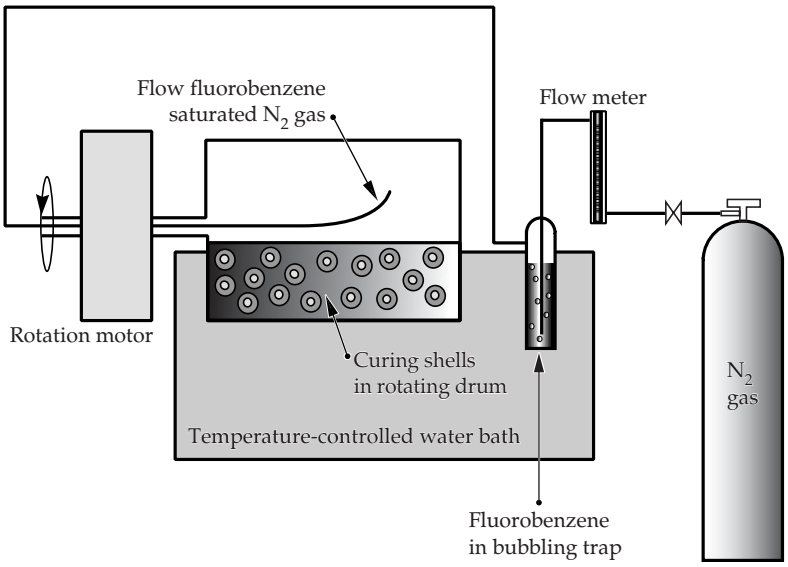

FIGURE 4. Shown is the temperature-controlled rotating drum curing device. A flow of N_2 gas partially saturated with fluorobenzene vapor controls the rate of curing. (NIF-0401-02079pb01)

the shell buckles or a gas bubble nucleates in the interior water phase and relieves the pressure. After two or three days, we must nucleate the gas bubble with an ultrasonic bath to avoid the cracking or collapse of thin wall (<20 μm) shells; thick-wall shells are strong enough to nucleate a bubble on their own. Once bubbles have formed in the shells, they are put in a vacuum oven at low temperature to remove the rest of the interior water phase. At room temperature, that can take 5 to 7 weeks.

The Mode-2 Out-of-Round Problem

Theoretical Considerations

Below is a review of some of the relevant modeling results that have formed the framework for our experimental work. The model used was initially a simple homogeneous fluid droplet suspended in a second immiscible fluid,[9] though more detailed consideration of the compound droplet has also been undertaken, both at LLNL[10] and elsewhere.[8] For the homogeneous droplet, the only force promoting sphericity is due to the interfacial tension γ. The distorting forces examined included (a) deformation due to a density mismatch between the droplet and the supporting bath and (b) deformation due to hydrodynamic interaction between the bath fluid and the droplet. For the first case one can show that maximum out-of-round (MOOR), equal to the difference between the maximum and minimum droplet diameters, is given by

$$\mathrm{MOOR} \cong \frac{5gr^3\Delta\rho}{4\gamma}, \qquad (1)$$

where g is the acceleration of gravity, r the droplet radius, and $\Delta\rho$ is the density difference between the droplet and supporting fluid. This calculation, which assumes an ellipsoidal deformation, was done for a droplet sitting on a surface, but is also accurate for situations in which the droplet deformation is more rapid than translational droplet motion. As an example of the effects of hydrodynamic interactions, the case of the fluid droplet in a linear shear gives

$$\mathrm{MOOR} \cong \frac{8\mu G r^2}{\gamma}, \qquad (2)$$

where μ is the bath viscosity and G is the linear shear field experienced by the droplet, related to both the method and intensity of the bath agitation method. In both examples note the greater-than-linear

dependence on the droplet size and that the distortion scales with $1/\gamma$. It is clear from these simple models that good density matching (low $\Delta\rho$), attention to bath agitation, and maximization of the interfacial tension γ are critical to minimizing MOOR.

Density Matching

Our initial studies showed us that the basic mode-2 out-of-round was sensitive to the density match of the bath to the compound droplet (inner water core plus oil phase), consistent with Eq. 1. Careful measurements of the density of fluorobenzene solutions of PαMS as a function of temperature and concentration were made to determine the optimal density matching conditions, at least at the time of droplet generation. Since the thermal expansion coefficient of fluorobenzene is greater than water, it was possible to use temperature to adjust the density of the compound droplet to that of the bath density. However, the density of the compound drop is time dependent due to the continuous loss of the fluorobenzene during cure. Careful modeling calculations showed that the variation in compound droplet density would be limited to a few thousandths of a g/cm^3, [6] probably about as good as our absolute control given small variations in the droplet to droplet size and wall thickness.

Application of these density-matching controls and more gentle bath agitation techniques certainly improved the quality of our shells, but still left us somewhat above the specification we were trying to meet. Specifically, the mode-2 out-of-round was still a few microns in the best shells, somewhat larger than the desired one micron. In addition, middle-mode roughness was still high, with shells generally showing a clear bump in the power centered at modes 10 to 20, and vacuoles near the surface as well as surface debris were still causing significant high-frequency roughness. The ultimate solution to the mode-2 problem is detailed in the next section; the middle- and higher-mode problems are discussed in the sections "Solutions to the Mode-10 to –50 Bump Problem" and "Solutions to the High-Frequency Roughness" that follow.

Interfacial Tension

It was clear that an additional handle to control the mode-2 out-of-round was to increase the interfacial tension γ. We began by considering other organic solvents for the oil phase,[6] but the requirements for density matching, water insolubility, and polymer solubility drastically limited our choices, and we determined there was not much to gain by this approach. Thus, effort was focused on modification of the aqueous bath phase.

As noted above, PVA has historically been used as the protective colloid additive to the bath. PVA acts as an entropically driven steric stabilizer, resisting the approach of two encapsulated droplet surfaces because of the entropic consequences of deforming the PVA random coils in the aqueous phase between them. This action, however, is independent of the effect that PVA or any other polymeric stabilizer might have on the oil/aqueous interfacial tension. A typical value of the interfacial tension between a pure nonpolar organic fluid such as benzene and pure water is about 35 dynes/cm, about half the value of pure water against air. Interfacial tension measurements showed that our relatively impure systems (fluorobenzene containing PαMS vs water containing PVA) had an interfacial tension about twenty times less (Table 1).

We have discovered that high molecular weight PAA is an equally effective protective colloid, while significantly increasing the droplet/bath interfacial tension. The differences between PAA and PVA with respect to interfacial tension were clearly demonstrated in a series of experiments based on homogeneous

TABLE 1. Interfacial tension measurements by droplet deformation of 2.5-mm-diam PαMS/fluorobenzene drops in various aqueous solutions. Measurements made at 45°C.[11]

Additive	wt%	Δ diam (μm)	Δρ (g/cm^3)	γ (dyne/cm)
None	(0)	165	0.021	3.0
PVA	2	221	0.016	1.7
PAA	0.025	17	0.021	30.
PAA	0.00625	29	0.021	17.
PAA	0.00156	18	0.021	28.

droplet deformation.[11] Droplets 2.5 mm diam of 15 wt% PαMS in fluorobenzene were placed on a flat glass support in an aqueous bath containing pure water, 2 wt% PVA, or PAA at a variety of concentrations as shown in Table 1. The droplet shape was recorded photographically, and from this image the horizontal and vertical drop diameters were measured. Eq. 1 was then used to evaluate the value of the interfacial tension γ using independently measured values of the fluid densities.[6] This method is a rough approximation to the sessile drop method of determining interfacial tension,[12] and is adequate to demonstrate the marked difference between PVA and PAA solutions. We find that the interfacial tension of the oil/PAA system is a factor of 10 or more higher than that of the oil/PVA system, in fact near to the expected value for a pure nonpolar solvent against water.

The structures of PVA and PAA are shown in Figure 5a. The effectiveness of PAA as a protective colloid at very low concentrations (0.01 to 0.05 wt%) may be due in large part to the very high molecular weight, but the polymer molecular weight should have little effect on the interfacial tension. The differences may be due to the weak ionic character of PAA (in contradistinction to PVA) in aqueous media (Figure 5b). This polyelectrolyte character leads to strong interactions between the macromolecules in solution, with the result that for concentrations at or above 0.05 wt%, the quiescent solution forms a thixotropic gel. Another manifestation of this strong interaction is in measurements of solution viscosity as shown in Figure 6. We have found that microencapsulated shells can only be produced at a bath viscosity of less than about 10 to 20 cP (PAA concentrations no greater than 0.05 wt%); at higher viscosity the shear from mixing causes the encapsulated droplet to lose its inner aqueous core.

The increase in interfacial tension manifests itself in the microencapsulation process in shells with distinctly reduced mode-2 out-of-rounds as illustrated in Figure 7, where we show in histogram form the best PVA and PAA batch results. Also shown is the nonconcentricity (NC), which also shows a significant improvement. Figure 7 also demonstrates the significant increase in consistency made possible by the use of PAA.

Solutions to the Mode-10 to -50 Bump Problem

Almost all microencapsulation PαMS shells regardless of size have had a prominent peak or shoulder in the power spectrum near modes 10 to 20, often 2 to 3 orders of magnitude higher than the NIF specification. Frequently, this defect can be seen clearly as oscillations in the AFM

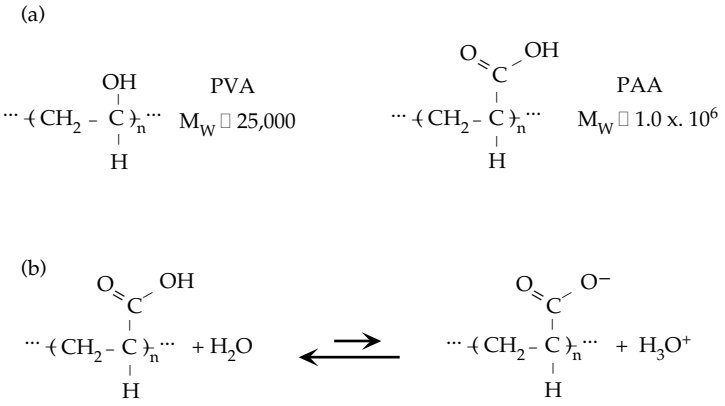

FIGURE 5. (a) Structures of PVA and PAA. (b) Partial ionization of PAA. (NIF-0401-02080pb01)

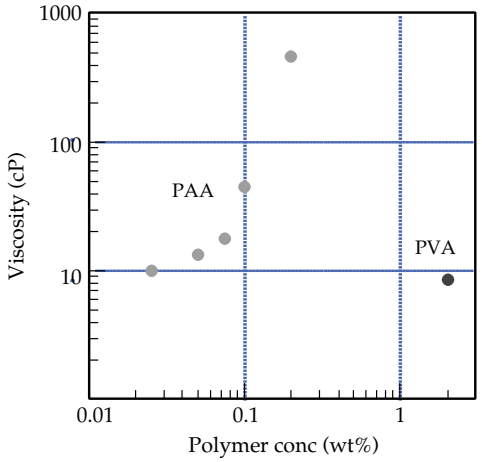

FIGURE 6. Viscosity of PAA and PVA as a function of polymer concentration. (NIF-0401-02081pb01)

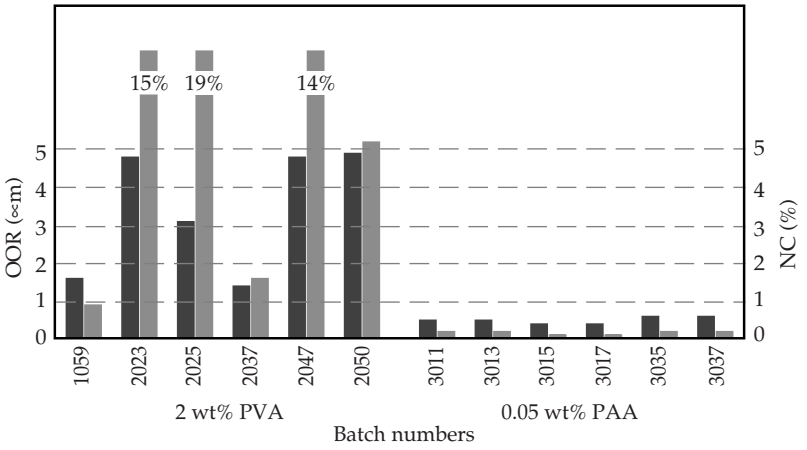

FIGURE 7. Histogram picture of OOR (black) and NC (gray) for 6 batches each of PVA and PAA processed shells. (NIF-0401-02082pb01)

equatorial traces with amplitudes of 100s of nm and wavelengths of ~500 μm. Simultaneous wall thickness measurements usually show that the largest component of the defect is a wall "wrinkle" rather than a thickness variation. Since power in modes between 10 and 50 is the major driver of Rayleigh–Taylor instability in the implosion, it was essential to identify the origin of the defect and eliminate its presence.

There have been multiple hypotheses for the origin of this mode-10 to -20 power, among them buckling due to osmotic stress during the curing[13] or due to unspecified shrinking stresses in the drying (the focus on stress being motivated by the very long wavelength nature of the defect and the view that this was the product of some global rather than local cause). We now believe that the seeds of this low-mode structure are set by convection cells that form in the fluid shell wall during the curing phase. The existence of convection cells is well known in the drying of thin flat films. This phenomenon is called Marangoni convection and is driven by surface tension gradients at the surface of the film.[14] These gradients can be generated by temperature (heat flow) or concentration (mass flow) differences. In our situation, we have a variation of surface tension with polymer concentration. This convection is analogous to Rayleigh convection in thicker films, where density gradients due to temperature are the source.[15]

Marangoni convection for heat transfer has been studied in thin flat films for many years, but application of these principles to the drying of spherical shells is new. Two important results can be derived.[16] First, the theory yields the conditions under which Marangoni convection is "turned on," namely that the Marangoni number M be greater than some critical value M_C. The Marangoni number for our situation of a shell losing solvent from its outer wall is defined as

$$M = \frac{\Delta C w (d\gamma / dC)}{\eta D}, \qquad (3)$$

where ΔC is the difference in polymer concentration C from the inside to the outside of the fluid wall of thickness w, $(d\gamma/dC)$ is the change of the outer surface interfacial tension with respect to polymer concentration, η is the oil phase viscosity, and D is the diffusivity of fluorobenzene in the oil phase. Second, the theory allows the prediction of the spherical harmonic mode that should characterize the lateral length scale of the convection cells. In a flat film there is only one characteristic length, the thickness of the film, and this determines both the critical Marangoni number and the dimension of the convection cell. However, for a spherical shell,[17] there are two length scales of interest, the thickness of the oil phase wall w and the circumference $2\neq r$ of the oil phase shell. These two length scales give rise to a set of solutions of the hydrodynamic equations, each solution corresponding to a different spherical harmonic mode l characterizing the relative

size of the convection cells. However, for each mode, there is a unique critical Marangoni number. Thus, the physically observed l mode will be the one that gives the *minimum* critical Marangoni number. Using our best estimates for our experimental process parameters, we find that this mode is approximately given by

$$l_{ob} \cong \frac{2\pi r}{4w}, \quad (4)$$

Thus the characteristic size of the observed convection cell is very close to four times the initial film thickness w. The value of r/w is dependent only on the ratio of the inner water and oil phase flow rates, and we find for typical encapsulation conditions that the predicted mode based upon the *initial* encapsulation conditions is between 8 and 17, consistent with the experimental results we have seen.

These shells are not in steady state but rather are continually changing during cure. As the solvent is removed, the interfacial tension and probably also its gradient are changing, the wall thickness is decreasing, the viscosity is dramatically increasing, and the diffusivity of fluorobenzene probably decreasing. Thus, primarily because of the decrease in w and increase in η, the Marangoni number for the shell is decreasing during curing. Assuming M starts off above M_C, at some time later its value drops below the critical value and convection stops. If the oil phase shell is too viscous at this point to "relax out" distortions caused by the convection cells, their imprint will remain in the final dry shell. Experimentally, we find that the mode structure we see corresponds roughly with the compound droplet conditions at the time when the droplet is initially formed, when the convection is easiest due to low viscosity, rather than at some later time when M is still greater than M_C, but the calculated l_{ob} has changed due primarily to the thinning wall. The failure of the shell convection cells to "adjust" to the changing geometry by decreasing their size (and simultaneously increasing their number) is possibly due to an activation barrier.

Although we do not have quantitative values for many of the relevant terms, the functional relationships developed clearly point to processing changes that can decrease M and thus potentially shut off Marangoni convection while the shell is still fluid enough to relax, or perhaps prevent it entirely. As described below, the easiest parameters to control are the polymer concentration difference across the wall ΔC and the initial wall thickness w.

We can decrease ΔC by slowing the removal of fluorobenzene during curing. Control of the rate of fluorobenzene removal is achieved by providing a flow of nearly saturated fluorobenzene vapor to the space above the curing bath as shown in Figure 4. In principle, the level of saturation can be controlled exactly; however, in the experiments described here, we have simply bubbled the N_2 flow through a tube containing fluorobenzene at the same temperature as the bath. As shown in Figure 8, we find that 2-mm OD shells cured in one day (without a fluorobenzene vapor flow) show a substantial mode-10 feature compared to shells in which the curing was extended to four days using fluorobenzene vapor. By extending the drying, we have decreased ΔC and presumably dropped the shell Marangoni number below the critical value, eliminating convection, either from the time of compound droplet formation or while the oil layer was still fluid enough to relax.

Decreasing w also dramatically decreases the mode-10 power. Thinner-walled shells can be made by starting with more dilute polymer in the oil phase and/or by encapsulating with a thinner initial oil phase layer. The latter is preferable from the point of view of minimizing the initial shell M value, hopefully to a value below M_C so that convection is not turned on. However, the use of more dilute solution is often necessary for the formation of stable initial compound droplets by the droplet generator. In these cases, the initial value of M may, in fact, be greater due to the lower viscosity of the oil phase; however, we believe M drops below M_C while the shell is still fluid enough to relax away the convection cell imprint. To demonstrate the effect of decreasing w, in Figure 9 we plot the observed mode-10 power for

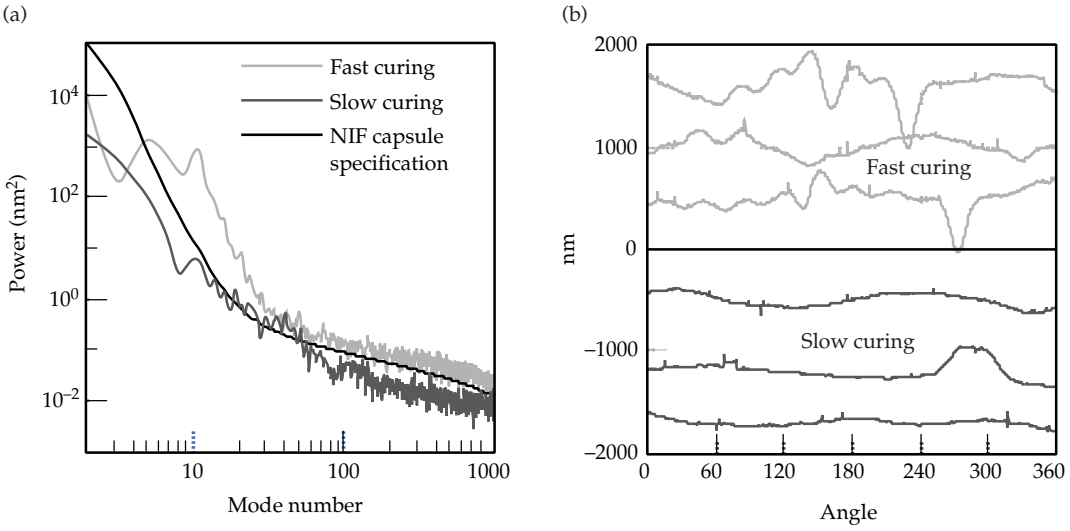

FIGURE 8. (a) Power spectra for two shells are shown, the light gray data for a shell cured rapidly in one day, the dark gray data for a shell cured more slowly over four days. (b) Examples of AFM traces taken from the two shells clearly show a dramatic difference in long-length scale surface oscillations. (NIF-0401-02083pb01)

individual shells as a function of the final dry shell wall thickness for a set of 950-µm-diam shells all made with 8 wt% PαMS in fluorobenzene. For these shells, the variation in wall thickness was controlled by varying the relative oil to inner core water flow rates. Although shell-to-shell results vary significantly, the mode-10 power clearly increases dramatically (note log scale) with thicker-walled shells.

These recent experiments, though qualitative in nature, demonstrate that we have identified Marangoni convection as the controlling mechanism that leads to the mode-10 to -20 power seen on previously fabricated mandrels. Further, we have shown that by process control of slowing the curing process and/or reducing *w*, we can either prevent the onset of Marangoni convection or insure that it turns off while the shell is still fluid enough to relax.

Solutions to the High-Frequency Roughness

Vacuoles

Polymer shells made by microencapsulation have historically had a problem with vacuoles. The vacuoles are present as a dispersion of voids or bubbles in the final shell wall with diameters up to several microns. They affect the high-frequency surface finish by either perturbing the surface if they lie close to it or by creating small "pits" if they break through the surface as the shell dries. These very-high-frequency defects are then amplified in subsequent coating operations to produce unacceptably rough surfaces.

It had long been understood that the vacuoles were caused by phase separation of water in the oil phase wall during the curing step. However, the specific mechanism of this phase separation was unknown. Initially, it was thought that when the concentration of polymer increased as the organic solvent dissipated

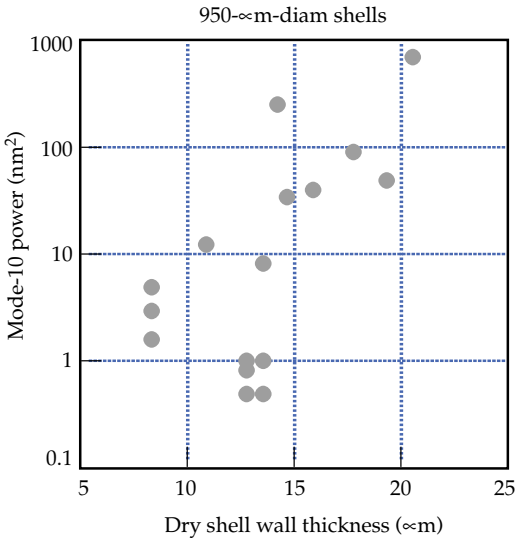

FIGURE 9. Shown are measurements of mode-10 power as a function of final shell wall thickness for a number of 950-µm-diam shells. Wall thickness was controlled by varying the relative oil to inner core water flow rates. (NIF-0401-02084pb01)

into the bath, the solubility of water in the oil phase wall would decrease, resulting in supersaturation. Modeling of this process demonstrated that this was the case; however, the predicted degree of supersaturation was very low, effectively precluding homogeneous nucleation and suggesting that heterogeneous nucleation promoted by particulate or ionic impurities was responsible for vacuole formation.[18] Subsequent to this modeling work, it was discovered that the addition of inorganic salts to the aqueous bath would suppress vacuole formation, presumably by lowering the water activity in the bath relative to possible water droplets in the oil phase.[19] It was also observed that water droplets would spontaneously form in a fluorobenzene solution of PαMS when placed in contact with water, indicating that supersaturation caused by solvent removal was unnecessary and supporting the concept of the presence of a hydrophilic impurity in the organic phase driving aqueous droplet formation. Further analysis showed that the PαMS contained 20 to 50 parts per million lithium salts, a residue from the butyl lithium initiator used to prepare the polymer from monomer. Removal of this ionic impurity by multiple reprecipitations now allows us to produce nearly vacuole-free shells without the use of inorganic salts in the bath. There remain a variable but small number of generally larger vacuoles that seem to have different origins—their elimination is the subject of ongoing efforts.

Surface Debris

The presence of small amounts of surface debris on the mandrels is problematic. Although a 1-μm piece of dust on the surface may be thought to add roughness to the shell surface power spectrum at only very high frequency, subsequent coating operations can lead to a significant broadening of the bump resulting in unacceptable dome formation.[20] Thus, cleanliness is of extreme importance. Not only are all solutions carefully filtered, but the entire fabrication operation is conducted in a Class-100 clean-room environment. With these techniques and the use of PVA as the bath protective colloid, we have been able to produce shells essentially free of surface debris.

However, as discussed previously, the interfacial tension benefits of using very high molecular weight PAA as the bath additive are significant. Unfortunately, we have found that shells produced in these baths have what appears to be areas of thinly deposited PAA on their surfaces. In general, these deposits have only a very minor effect on the bare shell power spectra, but are manifest more seriously in subsequent coatings.

We are currently developing techniques to remove these deposits. Our initial attempt involves making use of the highly functionalized PAA structure. When used in the baths, PAA is dissolved into pure water, thus it is only weakly ionized (Figure 5). However, in the presence of base, the molecule becomes a completely ionized polyelectrolyte, and because of this, its chain conformation changes radically.[21] Likewise, it can be completely protonated by treatment with acid. In initial experiments, we have used washes with acid and base to loosen and remove PAA from fully cured shell surfaces, expecting that the changes in chain conformation will facilitate the process. Some success has been achieved, as is shown in Figure 10. Shown on the left are both SphereMapper traces and an AFM patch scan of a PαMS shell that was produced in a PAA bath and rinsed only with water before drying. Note the high-frequency roughness in the traces as well as the mottled appearance of the patch scan. On the right is a shell from the same batch that was also rinsed with dilute NaOH (2%), rinsed again with water, and then rinsed with dilute HCl (0.5%) followed by a final rinse with water. The trace profiles are clearly improved, and the patch scan shows significantly reduced deposits. However, capsules made from these washed PαMS mandrels are still too rough to meet our requirements, so development of techniques to prevent or remove these deposits is an ongoing activity.

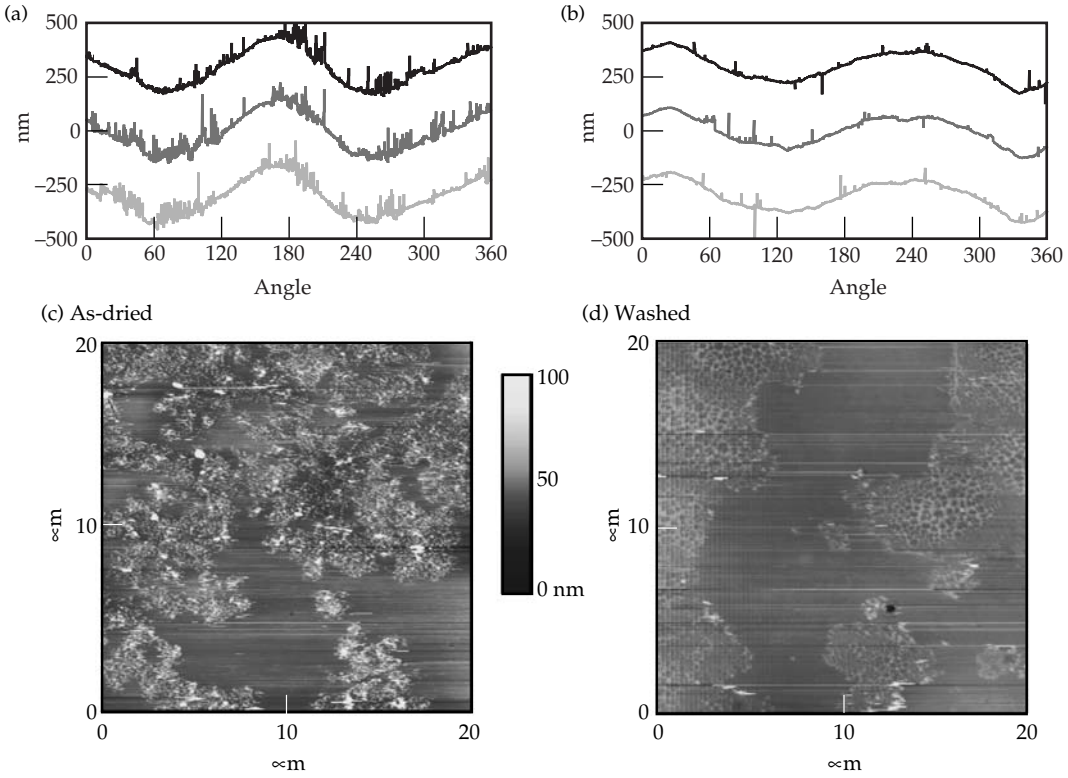

FIGURE 10. Three parallel AFM SphereMapper traces 40 μm apart [top, (a) and (b)] and AFM patch scans (bottom) of a PαMS mandrel cured in a PAA solution (c) as-dried and (d) after washing in dilute NaOH and HCl solutions. (NIF-0401-02085pb01)

Current Status

In the course of solving the surface roughness problems, we have substantially modified the mandrel production process, making use of our understanding of the important materials and processing parameters. Part of the solution involved new chemical interactions and mechanical processes, and part was due to better materials and processing control. Clearly, all aspects of the process are interrelated, and in some cases, the solutions to one problem have had consequences for another.

In Figure 11, we show five power spectra from representative 2-mm PαMS shells. Clearly, we are at or below the *final* capsule design requirements. However, as noted at the beginning of this article, these are just the initial mandrels, and one must be concerned with subsequent coating operations. Of particular importance is the PAA deposit roughness described above, which is spread over the high-frequency modes.

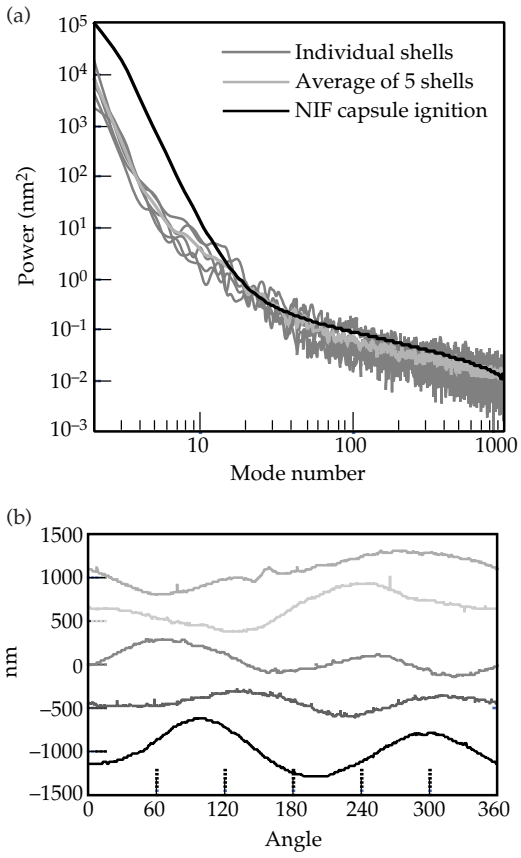

FIGURE 11. (a) Shown are power spectra for five of the best shells from recent batches. The very light gray line in the power spectrum graph is the average of the five-shell power spectra; it is at or below the final capsule design specification (shown in black). (b) A representative trace from each of the shells is shown. Visible on these traces is evidence of PAA surface contamination. (NIF-0401-02086pb01)

We have found that coatings on these shells produce lower-frequency power in the critical central part of the spectrum, and for this reason, this is our primary concern at this time.

Notes and References

1. R. Cook, "Production of Hollow Microspheres for Inertial Confinement Fusion Experiments," *Mat. Res. Soc. Symp. Proc.* **372**, 101 (1995).
2. M. Takagi et al., "Development of Deuterated Polystyrene Shells for Laser Fusion by Means of a Density Matched Emulsion Method," *J. Vac. Sci. Technol. A* **9**, 2145 (1991).
3. R. Cook, R. McEachern, and R. B. Stephens, "Representative Surface Profile Power Spectra from Capsules Used in Nova and Omega Implosion Experiments," *Fusion Technol.* **35**, 198 (1999).
4. R. L. McEachern, C. E. Moore, and R. J. Wallace, "The Design, Performance, and Application of an Atomic Force Microscope-Based Profilometer," *J. Vac. Sci. Technol. A* **13**, 983 (1995).
5. T. Norimatsu et al., "Cryogenic Targets and Related Technologies at ILE Osaka University," *J. Vac. Sci. Technol. A* **12**, 1293 (1994).
6. R. C. Cook et al., *Mandrel Development Update—1/98 to 12/98*, Lawrence Livermore National Laboratory, Livermore, CA, UCRL-ID-133144, February 1, 1999.
7. S. A. Letts et al., "Fabrication of Polymer Shells Using a Depolymerizable Mandrel," *Fusion Technol.* **28**,1797 (1995); B. W. McQuillan et al., "The PαMS/GDP Process for Production of ICF Target Mandrels," *Fusion Technol.* **31**, 381 (1997).
8. T. Norimatsu et al., "Modeling of the Centering Force in a Compound Emulsion to Make Uniform Plastic Shells for Laser Fusion Targets," *Fusion Technol.* **35**, 147 (1999).
9. R. C. Cook, P. M. Gresho, and K. E. Hamilton, "Examination of Some Droplet Deformation Forces Related to NIF Capsule Sphericity," *J. Moscow Phys. Soc.* **8**, 221 (1998).
10. P. M. Gresho, "Some Aspects of the Hydrodynamics of the Microencapsulation Route to NIF Mandrels," *Fusion Technol.* **35**, 157 (1999).
11. M. Takagi et al., "Decreasing Out-of-Round in Poly(α-methylstyrene) Mandrels by Increasing Interfacial Tension," *Fusion Technol.* **38**, 46 (2000). We note that the computed values of γ in this paper are high by a factor of 10 due to a calculation error. They have been corrected in Table 1.
12. A. W. Adamson, "Physical Chemistry of Surfaces," John Wiley & Sons, New York, pp. 27–36 (1982).
13. M. Takagi et al., "The Effects of Controlling Osmotic Pressure on a PαMS Microencapsulated Mandrel During Curing," *Fusion Technol.* **38**, 54 (2000).
14. M. J. Block, "Surface Tension as the Cause of Benard Cells and Surface Deformation in a Liquid Film," *Nature* **178**, 650 (1956); C. V. Sternling and L. E. Scriven, "Interfacial Turbulence, Hydrodynamic Instability and the Marangoni Effect," *AICHE Journal* **5**, 514 (1959); J. C. Berg, A. Acrivos, and M. Boudart, "Evaporative Convection," in *Advances in Chemical Engineering* **6**, 61, (1966).
15. Lord Rayleigh (John W. Strutt, *Phil. Mag.* (6) **32**, 529 (1916); P. G. Drazin and W. H. Reid, "Thermal Instability," Chapter 6 in *Hydrodynamic Stability*, Cambridge University Press, 1981. Work on Rayleigh convection in spherical shells is given in S. Chandrasekhar, "The Thermal Instability of a Fluid Sphere Heated Within," *Phil. Mag.* (7) **43**, 1317 (1952); S. Chandrasekhar, "The Onset of Convection by Thermal Instability in Spherical Shells," *Phil. Mag.* (7) **44**, 233 (1953); S. Chandrasekhar, "The Onset of Convection by Thermal Instability in Spherical Shells—A Correction," *Phil. Mag.* (7) **44**, 1129 (1953).
16. B. W. McQuillan, to be published.
17. The essential hydrodynamics for this analysis can be found in three papers: (a) O. Pirotte and G. Lebon, "Surface-Tension Driven Instability in Spherical Shells," *Appl. Microgravity Technology*, I(4), 175–9 (1988); (b) H. C. J. Hoefsloot and H. W. Hoogstraten, "Marangoni Instability in Spherical Shells," *Appl. Microgravity Technology*, II(2), 106–8 (1989); and (c) O. Pirotte and G. Lebon, "Comments on the Paper 'Marangoni Instability in Spherical Shells,'" *Appl. Microgravity Technology*, II(2), 108–9 (1989).
18. G. Wilemski et al., "Prediction of Phase Separation During the Drying of Polymer Shells," *Fusion Technol.* **28**, 1773 (1995).
19. B. W. McQuillan et al., "The Use of $CaCl_2$ and Other Salts to Improve Surface Finish and Eliminate Vacuoles in ICF Microencapsulated Shells," *Fusion Technol.* **35**, 198 (1999).
20. S. A. Letts, D. W. Myers, and L. A. Witt, "Ultrasmooth Plasma Polymerized Coatings for Laser Fusion Targets," *J. Vac. Sci. Technol.* **19**, 739 (1981).
21. R. Y. Lochhead, J. A. Davidson, and G. M. Thomas, "Poly(acrylic acid) Thickeners," in *Polymers in Aqueous Media*, J. E. Glass, Ed., American Chemical Society, Chapter 7 (1989).

Validating DT Ice-Surface Roughness Diagnostics for NIF Inertial Confinement Fusion

J. A. Koch
T. P. Bernat
D. N. Bittner
B. J. Kozioziemski
J. D. Sater
A. J. MacKinnon
G. W. Collins
C. H. Still

Ignition of thermonuclear burn in inertial confinement fusion (ICF) experiments[1] will require extremely precise control of many laser and target parameters. The type of target currently envisioned for ignition experiments at the National Ignition Facility (NIF) has a frozen deuterium-tritium (DT) ice layer adhering to the inner surface of an ablator shell, and the specifications for the inner surface quality of this ice layer are extremely demanding.[2,3] To achieve ignition on NIF, the DT ice layer must be well-characterized. In some target designs, the ablator shell is transparent to visible light, greatly facilitating ice-surface characterization, while in other designs, the ablator shell is opaque. Formation of suitably smooth ice layers in opaque shells will probably rely heavily on the experience gained from the characterization of ice layers in transparent shells. Optical characterization of ice layers in transparent shells will, therefore, be critical to achieving ignition on NIF, and reliable diagnostics are required.

Currently, the primary optical diagnostic of DT ice-surface quality in spherical shells is backlit shadowgraphy,[4] and the geometry of this technique is shown in Figure 1. In this technique, light that is totally internally reflected from the inner ice surface is imaged in transmission as a bright band, and the power spectrum of the radial variations of the bright-band position is assumed to be equal to the power spectrum of the ice-surface radial profile in the great-circle plane perpendicular to the shadowgraph optical axis. The square of the rms surface roughness is then inferred by summing the mode coefficients of the bright-band power spectrum.

The details of how the bright band maps to the inner ice surface are complex

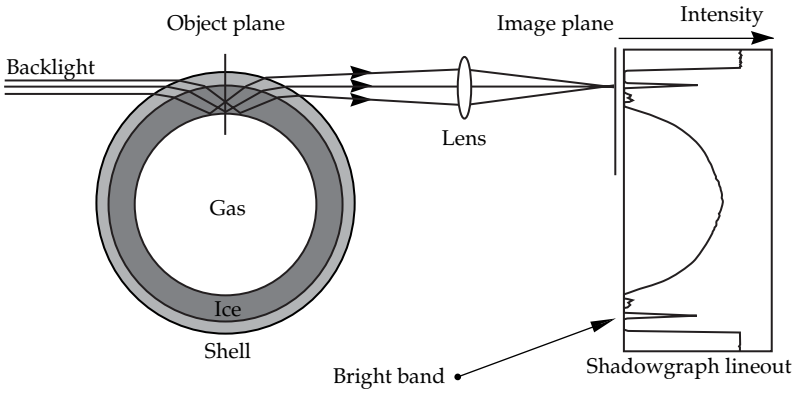

FIGURE 1. Schematic of backlit shadowgraphy, illustrating how light totally internally reflected from the inner ice surface forms a bright band in transmission. Other ray groups form weaker inner bands near the bright band; these inner bands appear concentric and nearly circular when the ice surface is very smooth. (NIF-0401-02035pb01)

and depend on many factors. Earlier ray-tracing work examined the behavior of the bright-band position in the presence of localized surface imperfections and found that the correlation depends on the height and curvature of the imperfection.[5] In general, a first-principles mathematical analysis is intractable, and ray tracing utilizing localized surface imperfections does not obviously illuminate the general case of many coupled surface modes. In the present work, we therefore take a different approach; we ignore the details of how the local bright-band position correlates to individual imperfections, and instead, we use exact numerical ray tracing to examine how well the overall power spectrum derived from the bright-band analysis corresponds to the actual ice-surface power spectrum inside the spherical shell. This approach directly addresses the validity of backlit shadow graphy, since ignition capsules will ultimately be qualified against specifications on the basis of power spectra and rms measurements.

We considered experimental characterization of a fabricated surrogate capsule as an approach to validating shadowgraphy, but this approach presents significant difficulties. First, one must rely on calibrations from a separate inner-ice-surface diagnostic that is known to be more reliable than shadowgraphy, and no such diagnostic exists over the full range of mode numbers accessible with shadow graphy; ray tracing through a simulated capsule eliminates this problem by allowing mathematical ice surfaces to be specified to arbitrary precision. Second, an experiment would only allow validation with a single surrogate ice-surface profile, and other profiles would require separate surrogate shells to be fabricated; ray tracing provides infinite flexibility for choices of simulated ice-surface parameters. Third, a diagnosable fabricated capsule would necessarily have different characteristics than a real ignition-qualifiable cryogenic ICF capsule (and would likely need to be a noncryogenic multilayer hemisphere), and the impact of these differences upon the conclusions of the experiments could not be known without ray tracing to verify that the differences are quantifiable. Finally, a simulation capability allows alternative optical diagnostic techniques to be investigated and compared with shadowgraphy, and allows for detailed analysis of any subtleties that might arise.

We have therefore developed a numerical ray-trace code, SHELL3D, to address this issue.[6] With SHELL3D, we simulate ice surfaces with specified spherical-harmonic modal imperfections, and we produce simulated shadowgraphs that are interpreted with the same data analysis code used to interpret real experimental data. We find that shadowgraph-derived power spectra are reliable indicators of ice-surface power spectra and total rms out to Fourier mode numbers as high as 80, *provided* the radial position of the bright band is defined with an appropriately fitting algorithm. We also find that the position fit previously used to define the bright-band position produces erroneously high power in the higher modes and overestimates the total rms by factors as large as 2; as a corollary, we find that our experimentally produced ice surfaces are smoother than we once thought they were. Finally, we find that experimental diagnostic improvements may be obtained by changing the illumination geometry and analyzing other shadowgraph features, and that enhanced information may be obtained by utilizing backlit transmission interferometry instead of simple backlit imaging. The results have significantly improved our understanding of how DT ice surfaces may be characterized in order to qualify them for ICF experiments on NIF.

Simulating Backlit Imaging Data with SHELL3D

We begin by reviewing the operation of SHELL3D. The simulated capsule geometry is shown in Figure 2. In SHELL3D, the outer and inner shell surfaces are defined as perfect cocentered spheres, and the inner ice surface is defined as the sum of

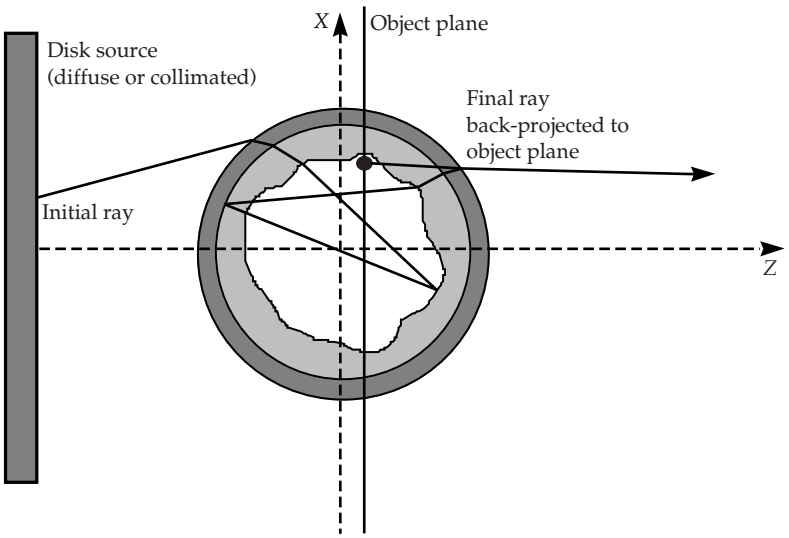

FIGURE 2. Schematic of the ray-tracing geometry used in SHELL3D. The simulation is nonsequential in that each ray can reflect from or transmit through the surfaces in any order before leaving the capsule and being back-traced. (NIF-0401-02036pb01)

real-valued spherical harmonics with arbitrary values of l and m:

$$x^2 + y^2 + z^2 =$$

$$R_1^2\left[1+\sum_{l=1}\left\{\begin{array}{l}A_{l,0}\sqrt{2l+1}P_{l,0}(\cos\theta)+\\ \sum_{m=1}^{l}\sqrt{\frac{2(2l+1)(l-m)!}{(l+m)!}}P_{l,m}(\cos\theta)*\\ \left(A_{l,m}\cos m\phi + A_{l,-m}\sin m\phi\right)\end{array}\right\}\right] \quad (1)$$

where R_1 is the $A_{0,0}$ coefficient, and the associated Legendre functions $P_{l,m}$ are defined by the usual recursion relations.[7,8] The outer ice surface is assumed to be identical to the inner shell surface, and the code does not permit topological changes such as cracks or gaps between the outer ice surface and the inner shell surface. Furthermore, each layer is assumed to be homogeneous, nonpolarizing, and nonabsorbing. The x-axis in Figure 2 is typically used for referencing θ in the spherical harmonics, and all results discussed in this paper use this orientation.

The general approach followed in the simulation is shown schematically in Figure 3. SHELL3D is essentially an analytical ray-tracing code; starting from an initial source point (x_0, y_0, z_0) and an initial ray vector $<a, b, c>$, the intersection point (x_1, y_1, z_1) with the outer surface $F(x, y, z) = 0$ is determined by substituting the parametric equations $F(x_0+at, y_0+bt, z_0+ct) = 0$ and solving for t. The transmitted and reflected ray vectors are determined based on the incident vector, the surface normal $\nabla F(x_1, y_1, z_1)$, and the indices of refraction. The choice of reflection or transmission is probabilistic based on the ray polarization, angle of incidence, and indices of refraction; the process then repeats from the new point and ray vector. Several features and subtleties are important to note:

a. The choice of spherical-harmonic recursion relations can have a significant impact on the numerical accuracy of the code, and in particular, it is easy to generate spurious high-frequency structures near the poles ($\theta \oplus 0$ and π) when using recursion relations that involve the term $\sqrt{1 - \cos^2\theta}$ in the denominator. We have taken care to eliminate these instabilities from our algorithms, which arise from round-offs and divide-by-zero errors.
b. The polarization of each ray is randomly chosen and fixed as S or P. In fact, the polarization with respect to the local surface will generally evolve as the ray propagates through the capsule if the inner ice surface is not spherical. This effect is not treated in the code, but the practical result of this simplification will be negligible for nearly smooth surfaces.

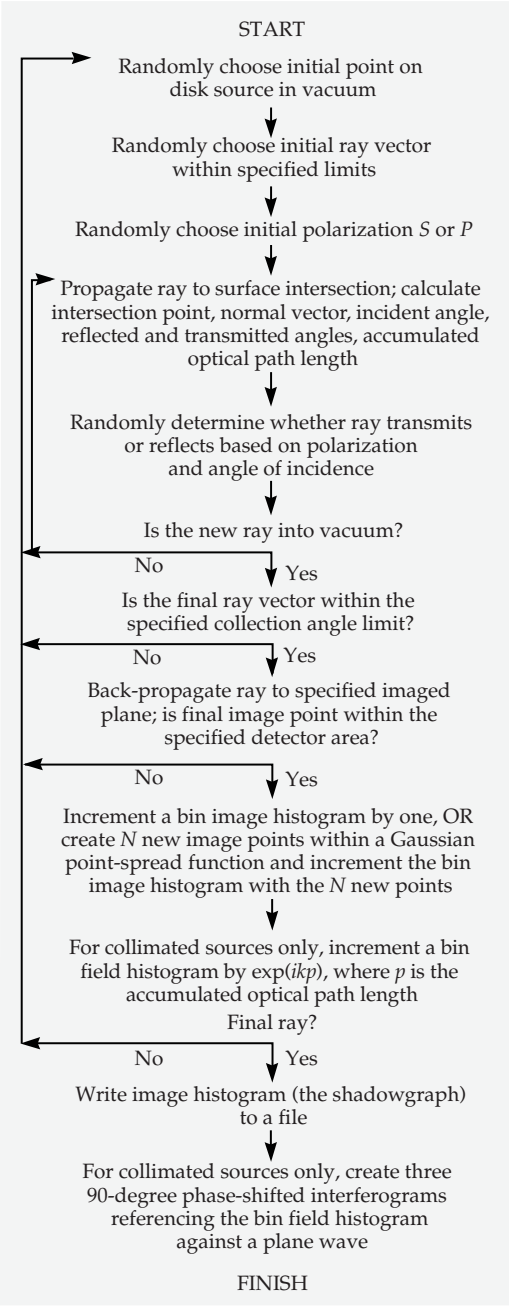

FIGURE 3. Logical flowchart of SHELL3D. (NIF-0401-02037pb01)

c. A wrapped transmitted phase map is generated along with the image array, and this map can be postprocessed by phase-unwrapping software to generate a transmitted wavefront map, as will be discussed below.
d. The maximum number of surfaces each ray can intersect is 16. This is sufficient to pass all forward-scattered, twice-reflected rays.
e. The effective imaging lens is perfect and has no distortion, but can be specified to have an effective point-spread function. In all cases discussed here, the imaged plane is the midplane of the capsule.
f. For the spherical surfaces, intersection points are determined analytically; there are generally two roots for each intersection, and the correct choice can be determined logically. For the spherical-harmonic surface, there are an unknown number of intersection points that cannot be determined analytically and that fall in an unknown order. For this surface, the code instead propagates the ray forward in small incremental steps in the region of the inner ice surface[9] until the first root is passed; this bounds the position of the root, which is then determined iteratively using an implementation of Brent's algorithm.[8]

The output shadowgraph array is a 1024×1024 pixelized image, which can be analyzed as if it were real data by the same analysis code, LAYER,[10] which is used to analyze experimental bright-band data. For comparison to the bright-band-derived power spectrum and surface rms, a separate code calculates the actual radial variations of the mathematically generated ice surface[11] as a function of θ in the great-circle plane perpendicular to the shadowgraph axis, and Fourier-transforms $\Delta R(\theta)$ to obtain a one-sided power spectrum. In both cases, the Fourier-mode coefficients sum to the square of the rms surface deviation in one dimension, which in turn can be related to the two-dimensional rms power spectrum most relevant to ICF ignition capsule simulations.[12]

All codes currently run on the Livermore Computing Center DEC 8400 machines. The central processing unit (CPU) time required to produce simulated images through two-dimensionally rough ice surfaces with SHELL3D scales approximately as L^2, where L is the maximum cut-off mode number. Good signal-to-noise ratios (>10 throughout the full field of view) for $L = 40$ can be obtained after approximately 750 CPU hours. For such large problems, multiple versions of SHELL3D can be run simultaneously using different random number seeds, and the results can be added to minimize the actual clock time required.

SHELL3D Validation of DT Ice Data

We described preliminary results obtained using a simplified rotationally symmetric version of SHELL3D in an earlier paper;[6] here we describe more recent results we obtained using the full capabilities of the code to validate real experimental DT data. In these simulations, we specify the spherical-harmonic mode coefficients $|A_{l,m}|$ to be functions of l only, but with randomly chosen signs for each value of l, m, and $-m$, and we use several functional scalings for $|A_{l,m}|(l)$ in order to vary the one-dimensional power spectrum and total rms. In the simulations described in this section, we assume an isotropically emitting, nonpolarized, incoherent, broadband diffuse backlight source that subtends $f/4$ as viewed from the capsule center; this is comparable to current experimental configurations. In all cases, we image the midplane of the capsule with an $f/4$ lens having a 3-μm-diameter (full width at half-maximum intensity) point-spread function.

Shadowgraph analysis is performed with LAYER.[10] In this analysis, the radial position of the bright band can be defined by a steepest-slope fit to the inside edge of the bright band, or by a Gaussian centroid fit to the center of the bright band. The edge fit has historically been used to analyze experimental data, while the Gaussian fit was only recently implemented. LAYER outputs a linearly unfolded bright-band curve and a one-dimensional bright-band–derived power spectrum in units of pixels-squared. The bright-band–derived power spectra can then be converted to units of μm-squared using the known scaling of the shadowgraph data for direct comparison to the known input ice-surface power spectrum.

Figures 4a and 4b show two simulated shadowgraphs from SHELL3D, both of which assume a 1-mm-diameter capsule with a 10-μm-thick plastic shell and a 100-μm-thick DT ice layer. Figure 4a specifies 10 modes of one-dimensional (rotationally symmetric about the x-axis in Figure 2) surface structure, while Figure 4b specifies 10 modes of two-dimensional surface structure with a comparable value for the total rms. Figures 4c and 4d show the power spectra of the actual ice-surface profiles from Figures 4a and 4b, respectively, together with bright-band–derived power spectra using both the edge fit and the Gaussian fit to define the bright-band position.

Several features are important to note in these figures. First, both the edge fit and the Gaussian fit to the bright-band position in the rotationally symmetric case of Figure 4c yield bright-band–derived power spectra that are in excellent agreement with the known input spectrum over the 10 modes that are actually present, but the edge fit diverges from the input spectrum for mode numbers >10 while the Gaussian-fit power spectrum falls rapidly above mode 10, in agreement with the input spectrum. This behavior is generally reproduced in the two-dimensional example in Figure 4d; however, the bright-band–derived power spectra do not match the input spectrum as well over the first 10 modes using either fit algorithm. We have found this to be a general feature of the two-dimensionally rough surfaces we have modeled and analyzed and to represent a difference from the rotationally symmetric results reported earlier.[6] This poorer peak-by-peak agreement likely results from polar-angle averaging (in the z-direction of Figure 2), which has a much stronger effect in the two-dimensionally rough case than in the rotationally symmetric case, and is dominated by the effective $f/\#$ of the diffuse backlight, as will be discussed below. We return to the reasons for the generally poorer agreement between the input spectra and the edge-fit bright-band spectra later in this section.

Recent experimental DT ice data[13] has shown approximately 1.5-μm total rms roughness for modes 1–60 and approximately 0.5-μm rms roughness for modes 3–60, using beta layering in a 2-mm-diameter capsule with a 30-μm-thick shell and a 200-μm-thick ice layer. This data was analyzed using a Gaussian centroid fit to define the bright-band position, and the results are significantly smoother than earlier data (analyzed with an edge fit to define the bright-band position) appeared

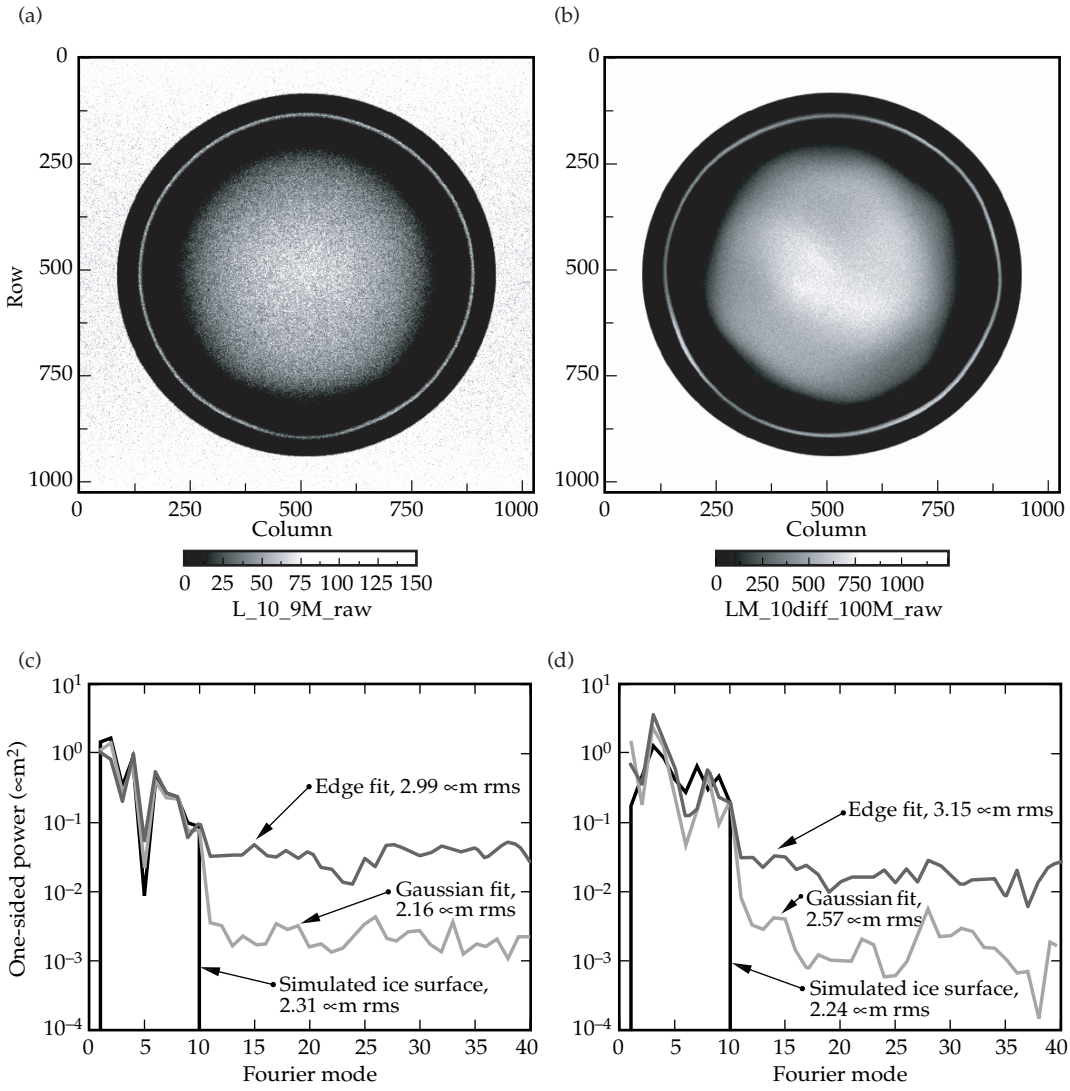

FIGURE 4. (a) Simulated shadowgraph of a rotationally symmetric ice surface with 10 L-modes of (one-dimensional) asymmetry; (b) simulated shadowgraph of a two-dimensionally rough ice surface with 10 LM-modes of asymmetry; (c) great-circle ice-surface power spectrum for the simulation of Figure 4a together with edge-fit and Gaussian-fit bright-band power spectra; (d) great-circle ice-surface power spectrum for the simulation of Figure 4b together with edge-fit and Gaussian-fit bright-band power spectra.
(NIF-0401-02038pb01)

to indicate. We show here that the current results are almost certainly correct, and that the earlier results were in error because the edge fit analysis yielded spurious high-mode power.

Figure 5a is an experimental shadowgraph of a DT ice layer in a capsule,[13] and Figure 5b shows bright-band–derived power spectra from both the Gaussian centroid fit and the edge fit. The edge-fit power spectrum clearly shows higher power in the higher modes and has an rms that is 86% higher. As noted above, the Gaussian centroid fit spectrum was expected to be correct based on earlier simulation results.[6] To verify this conclusion for the present case, we performed two simulations that are shown in Figures 5c and 5e. The first simulation is derived from a mathematical ice surface (with the same capsule and ice thickness parameters), which was specified to have a known power spectrum that nearly matches the *Gaussian-fit* spectrum from Figure 5b over the first 40 modes; the second simulation is derived from a mathematical ice surface (again with the same capsule and ice thickness parameters), which was specified to have a known power spectrum that nearly matches the *edge-fit* spectrum from Figure 5b over the first 40 modes. Qualitatively, the shadowgraph in Figure 5c appears fairly smooth, whereas the shadowgraph in Figure 5e

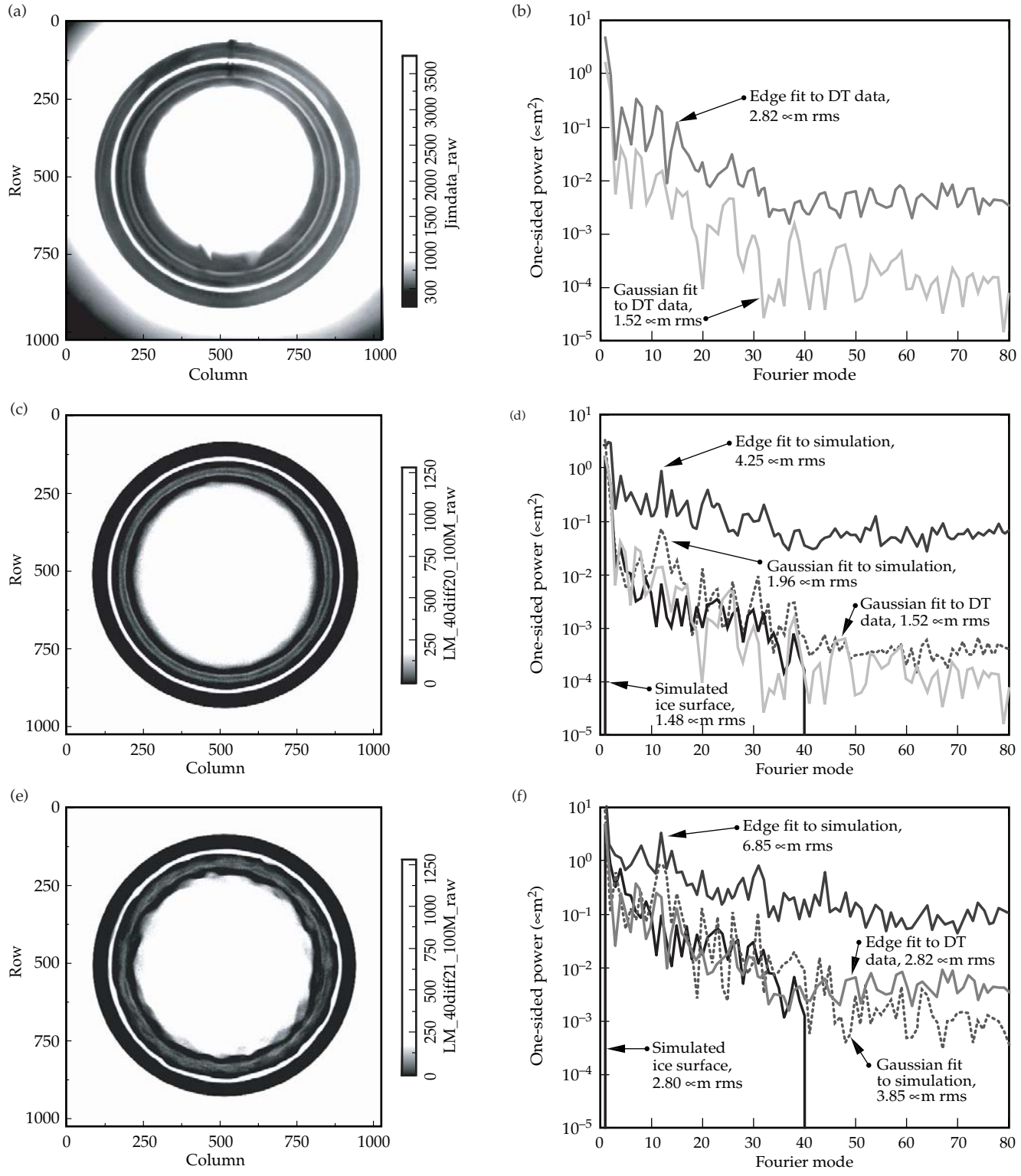

FIGURE 5. (a) Experimental shadowgraph of DT ice; (b) edge fit and Gaussian-fit bright-band power spectra from the data of Figure 5a; (c) simulated shadowgraph of an ice surface with a great-circle ice-surface power spectrum nearly equal to the Gaussian-fit bright-band power spectrum from the experimental data over the first 40 modes; (d) great-circle ice-surface power spectrum for the simulation of Figure 5c together with edge-fit and Gaussian-fit bright-band power spectra; (e) simulated shadowgraph of an ice surface with a great-circle ice-surface power spectrum nearly equal to the edge-fit bright-band power spectrum from the experimental data over the first 40 modes; (f) great-circle ice-surface power spectrum for the simulation of Figure 5e together with edge-fit and Gaussian-fit bright-band power spectra. The shadowgraph image intensity scales have been adjusted to bring out the bright band and inner bands more clearly. (NIF-0401-02039pb01)

appears substantially more mottled than the experimental ice surface shown in Figure 5a. This suggests that the experimental ice surface cannot be as rough as the edge-fit spectrum would indicate; this is quantitatively supported by the results from analysis of the two simulated shadowgraphs, which are shown in Figures 5d and 5f respectively. In *both* cases, the Gaussian centroid fit to the bright-band position matches the input spectrum very well, with total rms errors <35%, while in *both* cases the edge fit to the bright-band position seriously overestimates the power in modes >1 and overestimates the rms by factors of 1.5–2. We have reached similar conclusions from all other simulations we have analyzed; we therefore conclude that the Gaussian centroid fit to the experimental data is essentially correct, and that the edge fits used to analyze older experimental data were consistently overestimating both the higher-mode power and the total rms.

There appear to be two reasons for the poor accuracy of the older edge-fit analysis algorithm. First, the edge fit appears to be more susceptible to noise in the data, resulting in large spurious variations in the fitted position of the bright band. This is clear from Figure 6, which shows a known great-circle ice-surface profile for a 10-mode two-dimensionally rough simulation (that of Figure 4b) together with linearly unfolded shadowgraph bright bands and the corresponding Gaussian- and edge-fit profiles. The edge fit clearly shows spurious power in higher modes that is not actually present in the simulated ice surface, while the Gaussian fit

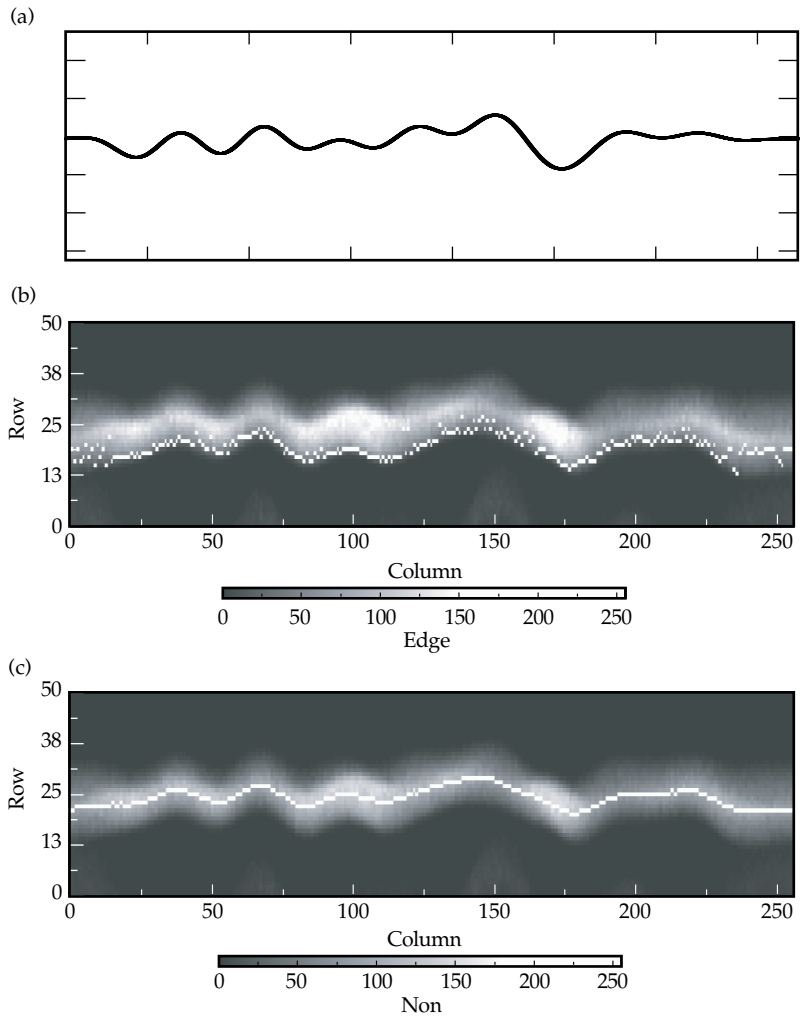

FIGURE 6. (a) Great-circle ice-surface profile from the 10-mode simulation of Figure 4b; (b) unfolded bright band and edge-fit profile (thin white line) from the simulation of Figure 4b; (c) unfolded bright band and Gaussian-fit profile (thin white line) from the simulation of Figure 4b. The horizontal axis is the azimuth angle from 0° to 360°, and the vertical axis is the radius. The vertical scale varies in these plots.
(NIF-0401-02040pb01)

matches the known input spectrum much more closely. The reason for this difference may be related to the lack of sharp edges in the bright band that would tend to help define the bright-band position for the edge fit. However, even the Gaussian fit does not exactly match the input profile, for reasons discussed below.

The second reason for the poorer accuracy of the edge-fit analysis is averaging along the surface in the direction of the optical axis. Figure 7 is a map of bright-band radius vs polar angle on the ice surface (relative to the z-axis in Figure 2) showing where rays that contribute to the bright band at a particular radius have intersected the ice surface. Each radius of the bright band consists of many rays that have intersected the ice surface at various polar angles; for this example of an $f/4$ diffuse backlight and $f/4$ imaging, a particular radius in the shadowgraph bright band corresponds to light that reflects off the ice surface over an ~12°-wide circular ribbon symmetric about the z-axis in Figure 2. Surface structure on the ice surface along this direction (particularly with mode numbers greater than ~30, corresponding to the 12° width) will therefore broaden the bright band, and the edge fit will track the inner edge of this broadened distribution. This adds spurious power to higher surface modes by confusing structure in the polar direction with structure in the azimuthal direction.

This effect is clear from Figure 8, which shows a known great-circle ice-surface profile for a 40-mode two-dimensionally rough simulation (that of Figure 5e) together with linearly unfolded shadowgraph bright bands and the corresponding Gaussian- and edge-fit profiles. The edge fit tracks scattering artifacts in the bright band along the lower boundary that do not correspond to actual great-circle-plane ice-surface features along the azimuth, but rather correspond to structure in the polar direction that has been averaged, resulting in a locally broadened band. The Gaussian fit, in contrast, is less affected by polar averaging and tracks the center of the distribution regardless of its width. This averaging does affect the absolute accuracy of the Gaussian fit, however, and is likely to be the reason why the Gaussian-fit power spectrum does not exactly match the input spectrum in two-dimensionally rough simulations (this is clear, e.g., in Figure 6).

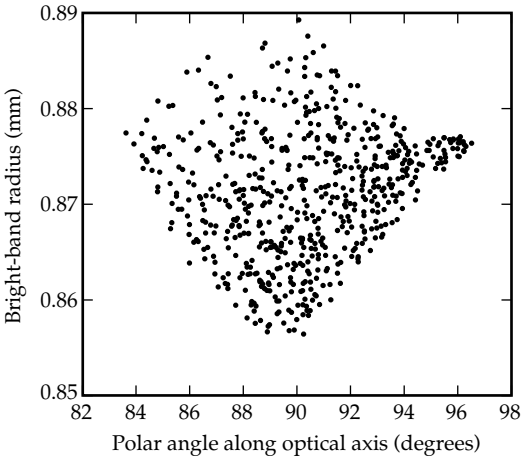

FIGURE 7. Points correspond to rays that appear at a particular radius in the bright band and that have reflected off the inner ice surface at a particular polar angle relative to the z-axis of Figure 2. This particular example is for an $f/4$ diffuse backlight and $f/4$ imaging, a 2-mm-diameter capsule, a 30-μm-thick shell, and a 150-μm-thick ice layer. The bright band clearly averages over an ~12°-wide circular ribbon in this case. (NIF-0401-02041pb01)

Progress towards Improved DT Ice Characterization

Based on the simulation work described above, we believe that diffuse-backlit shadowgraphy is a valid diagnostic of currently achievable DT ice-surface power spectra for great-circle mode numbers at least as high as 40, and perhaps[6] as high as 80, *provided* a Gaussian centroid-position fit is used to define the local bright-band radius. We also find that the edge fit previously used to define the local bright-band radius yields erroneously high power and overestimates the total rms by factors as large as 2; as a corollary, we find that our experimentally produced ice surfaces are smoother than we once thought they were.

Despite these successes, there are several reasons to seek improved characterization

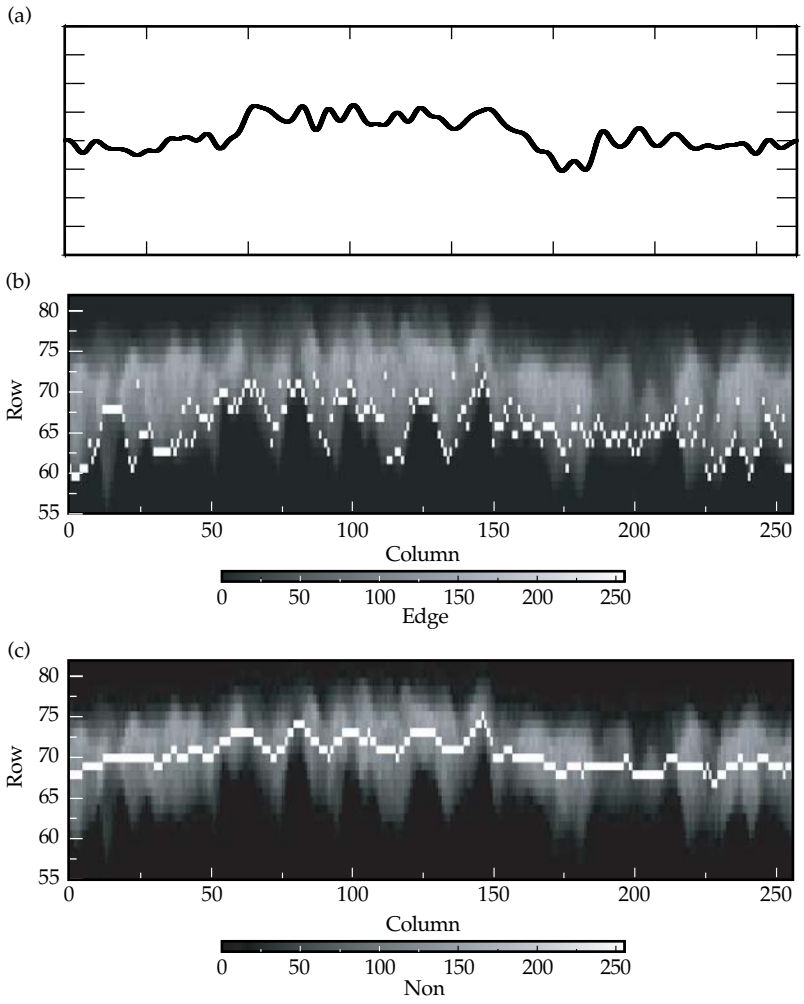

FIGURE 8. (a) Great-circle ice-surface profile from the 40-mode simulation of Figure 5e; (b) unfolded bright band and edge-fit profile from the simulation of Figure 5e; (c) unfolded bright band and Gaussian-fit profile from the simulation of Figure 5e. (NIF-0401-02042pb01)

techniques. Imaging with a diffuse backlight naturally increases polar averaging and eliminates any one-to-one correspondence between bright-band position and ice thickness in a single perpendicular plane (see Figure 7). This averaging broadens the bright band, degrades the achievable position-fitting precision, and limits our ability to observe and diagnose short–scale-length features. In addition, extremely smooth ice surfaces will become increasingly difficult to quantitatively diagnose since the radial variations in the bright-band position will become unobservably small. Finally, we anticipate a need to characterize DT ice surfaces in situ, in a hohlraum in the NIF target chamber prior to an ignition experiment, and restricted access to the capsule will constrain our ability to utilize existing characterization techniques.

One simple improvement to current backlit shadowgraphy is to use a collimated backlight rather than a diffuse backlight. Figure 9 shows SHELL3D simulated sections of a bright band that would be observed from the same ice surface under $f/4$ diffuse backlight conditions and under collimated (e.g., laser) backlight conditions. The collimated-backlight geometry clearly produces a sharper bright band, the position of which can be defined more precisely. Perhaps more importantly, however, the effects of polar averaging are minimized in the case of a collimated backlight, and a one-to-one relationship can be identified between ice-surface features in a single perpendicular plane and features in the bright band, particularly along the outer edge (see Figure 10). This suggests that higher-frequency spatial structure will be more easily observed at

(a)

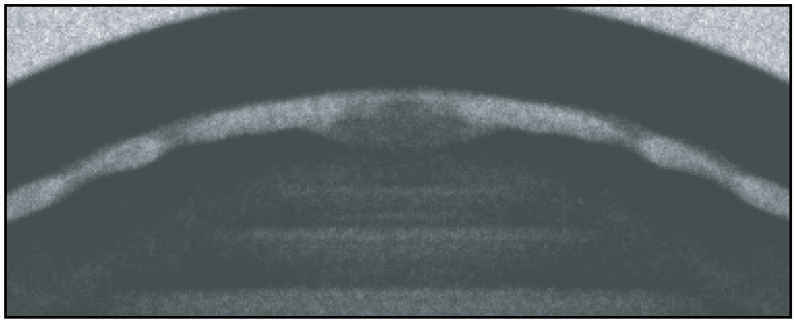

(b)

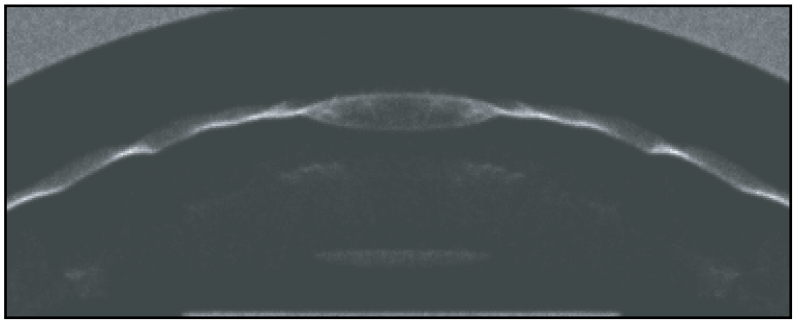

FIGURE 9. Close-up of the bright-band structure; (a) uses a diffuse backlight, while (b) uses a collimated backlight. The collimated backlight produces a sharper bright band, the position of which can be more precisely defined. (NIF-0401-02043pb01)

the outer edge of the bright band using a collimated-backlight geometry.

We also note that most shadowgraphs (e.g., Figures 5c and 5e) clearly show inner bands that are weaker but more distorted than the bright band. These bands result from other multiple-reflection ray paths and appear visually to be more sensitive indicators of ice-surface asymmetry than the bright band itself; however, the more complicated ray paths suggest that discerning a quantitative correspondence between inner-band structure and ice-surface structure will be difficult. Additionally, the central portions of the shadowgraphs (e.g., in Figure 4b) show mottled structure that is clearly related to ice-surface asymmetry; this structure may provide additional surface-quality information (particularly with a collimated backlight), though again the quantitative correspondence will probably be difficult to discern.

Finally, we note that bright-band transmission interferometry might be utilized to provide ice-surface–quality information. A simple implementation of this technique would be to interfere a plane-wave reference beam with a collimated-backlight shadowgraph image; in this case, the ray paths are already understood from the above analysis, and the quantitative

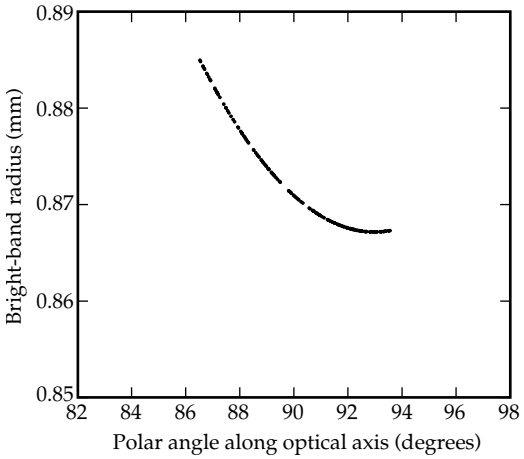

FIGURE 10. Points correspond to rays that appear at a particular radius in the bright band and that have reflected off the inner ice surface at a particular polar angle relative to the z-axis of Figure 2. This particular example is for a collimated backlight and $f/4$ imaging, a 2-mm-diameter capsule, a 30-μm-thick shell, and a 150-μm-thick ice layer. The inner edge of the bright band averages over an ~3°-wide circular ribbon in this case, while the outer edge of the bright band tracks a single trace along the ice surface. (NIF-0401-02044pb01)

correspondence between bright-band phase and surface structure is straightforward to derive for a given shell thickness, nominal ice thickness, and capsule diameter. In Figure 11 we show a simulated bright-band interferogram obtained by interfering a shadowgraph image (that of Figure 4b) with a plane-parallel reference beam. The bright-band phase varies significantly in azimuth and radius, and this phase correlates to the same surface structure that affects the radial position of the peak bright-band intensity (in this particular case, one wave of phase corresponds to 1.4 μm of ice-thickness radial variation). These phase variations may be more easily measured than radial variations of the position of the bright band, particularly for cases where the ice surface is nearly perfect.

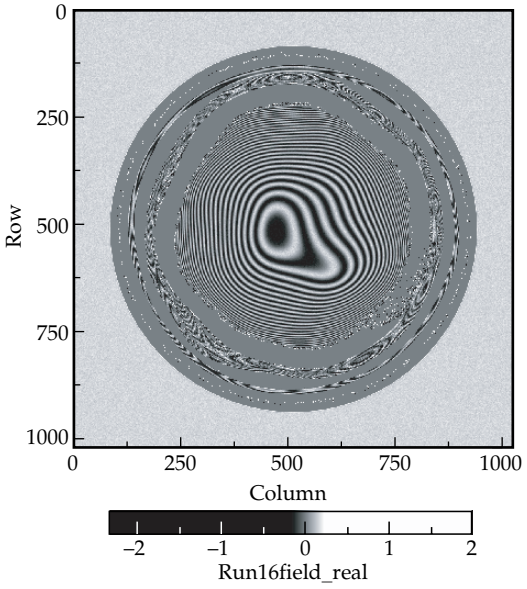

FIGURE 11. Simulated transmission interferogram of a two-dimensionally rough ice surface with 10 LM-modes of asymmetry, using a collimated backlight but otherwise using the same model parameters as used for the simulated diffuse-backlight shadowgraph shown in Figure 4b. Phase information in the bright band relates to optical path length difference; this can be related to surface roughness and can perhaps be observed more easily than radial position variations. (NIF-0401-02045pb01)

We are working towards developing phase unwrapping software that can be used to analyze bright-band interferograms, and we plan to perform experiments to develop this and other ice-surface characterization techniques in the coming year.

Acknowledgments

We thank J. Burmann, E. M. Campbell, S. Haan, B. Hammel, J. Hoffer, R. Jones, E. Mapoles, J. Pipes, and W. Unites for their contributions and support.

Notes and References

1. J. D. Lindl, *Inertial Confinement Fusion* (Springer-Verlag, New York, 1998).
2. T. R. Dittrich et al., *Phys. Plasmas* **5**, 3708 (1998).
3. T. R. Dittrich et al., *Phys. Plasmas* **6**, 2164 (1999).
4. J. K. Hoffer et al., *Fusion Technol*. **30**, 529 (1996).
5. Y. Lee, Lawrence Livermore National Laboratory, Livermore, CA, personal communication.
6. J. A. Koch et al., *Fusion Technol*. (in press).
7. E. Butkov, *Mathematical Physics* (Addison-Wesley, Reading, 1968).
8. W. H. Press et al., *Numerical Recipes in C* (Cambridge University Press, Cambridge, 1994).
9. The region of the inner ice surface is defined by two spheres that entirely contains the ice-surface profile; ray tracing within this region must be done carefully to avoid possible errors caused by multiple intersection points.
10. E. R. Mapoles et al., *Phys. Rev. E* **55**, 3473 (1997).
11. We calculate the great-circle-plane, one-dimensional power spectrum numerically using the same spherical-harmonic algorithms that are used in SHELL3D; this approach minimizes the potential impact of numerical errors in the algorithms on the comparison with the bright-band-derived power spectra.
12. S. M. Pollaine et al., *1994 ICF Annual Report*, Lawrence Livermore National Laboratory Report No. UCRL-LR-105820-94 (June 1995).
13. J. D. Sater, data from Lawrence Livermore National Laboratory beta-layered DT ice experiments.

Exploring the Limits of the National Ignition Facility's Capsule Coupling

L. Suter *S. Haan*

D. Munro *J. Rothenberg*

B. Van Wonterghem

Our original ignition "point designs"[1] (circa 1992) for the National Ignition Facility (NIF)[2] were made energetically conservative to provide margin for uncertainties in laser absorption, x-ray conversion efficiency, and hohlraum–capsule coupling. Since that time, extensive experiments on Nova[3] and OMEGA[4] and their related analysis indicate that NIF coupling efficiency may be almost "as good as we could hope for." Given close agreement between experiment and theory/modeling, we can credibly explore target enhancements which couple more of NIF's energy to an ignition capsule. These include using optimized mixtures of materials to reduce x-ray wall losses, slightly reduced laser entrance holes, and laser operation strategies that increase the amount of energy we can extract from NIF. We find that 3–4× increases in absorbed capsule energy appear possible, providing a potentially more robust target and ~10× increase in capsule yield.

The NIF in the United States and Laser Megajoule (LMJ)[5] in France, the next generation of high-energy, high-power ICF laser drivers, have the potential of achieving thermonuclear ignition and gain in the laboratory. One key element of achieving that goal is coupling a significant fraction of the laser's energy to a fuel capsule. We can relate the quantity of x-rays absorbed by an indirect-drive ignition capsule E_{cap} to the laser energy E_{NIF} via the expression

$$E_{cap} = \eta_{abs}\eta_{CE}\eta_{HR\text{-}cap}E_{NIF} \quad (1)$$

As indicated schematically in Figure 1, η_{abs} is the fraction of incident laser energy absorbed by the hohlraum, η_{CE} is the conversion efficiency of laser light into x-rays, and $\eta_{HR\text{-}cap}$ is the fraction of generated x-rays that are actually absorbed by the capsule. Typically, η_{abs} is assumed to be 1 – (SBS + SRS) where SBS is the fraction of incident laser light reflected or scattered out of the hohlraum by stimulated Brillouin scattering and SRS is the fraction reflected by stimulated Raman scattering.[6] Since E_{NIF} for NIF is nominally 1.8 MJ, standard "point design" capsules[1,7] that absorb 150 kJ of x-rays require $\eta_{abs}\eta_{CE}\eta_{HR\text{-}cap} = 0.083$. Additional constraints[1] are that the hohlraum be gas filled, the laser pulse shape be carefully tailored, and the peak radiation temperature (T_R) be 250 to 300 eV.

Numerical simulations of the ignition point design's hohlraum and capsule show

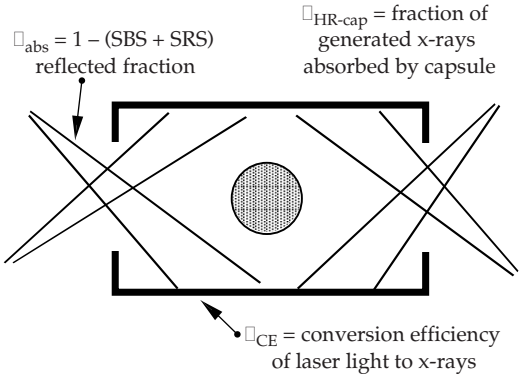

FIGURE 1. The x-ray energy absorbed by a capsule is the product of the three efficiencies shown and the laser energy.
(NIF-0401-02046pb01)

a theoretical conversion efficiency of ~80% and an $\eta_{HR\text{-}cap}$ of ~14%, producing a theoretical $\eta_{CE}\eta_{HR\text{-}cap}$ of 0.11. Compared to the 0.083 required efficiency, this provides a 25% margin. This margin was intentionally incorporated into the ignition program in the early '90s in order to compensate for uncertainties, allowing us to be off somewhat in our assumptions and still be able to achieve ignition. For example, if $\eta_{abs} = 1$ and $\eta_{CE}\eta_{HR\text{-}cap} = 0.11$, then $E_{NIF} = 1.35$ MJ would successfully drive our ignition design. Or if stimulated backscattering losses proved to be as much as 25% but $\eta_{CE}\eta_{HR\text{-}cap} = 0.11$, then the expected 1.8 MJ will successfully drive the ignition design. Similarly if $\eta_{abs} > 0.75$ and $E_{NIF} = 1.8$ MJ, then values of $\eta_{CE}\eta_{HR\text{-}cap} < 0.11$ would also work.

Since the original point design was specified, an extensive experimental effort, first on Nova[3] and, more recently, on the OMEGA[4] laser, has significantly reduced the uncertainties in coupling. Indeed, these experiments and their related analysis indicate that NIF coupling efficiency will be almost as good as we had hoped for. Ongoing experiments studying stimulated Brillouin and Raman backscattering (also known as Laser Plasma Interactions or LPI) in ignition hohlraum "plasma emulators" imply that the total backscattered losses from these two processes should be <~5% [Ref. 8]. Complementing this work are experiments studying the radiation drive[9-11] and symmetry[12-14] in laser-heated hohlraums. Analysis of these experiments shows that x-ray production and capsule coupling is very close to our modeling. We conclude that for a capsule of given area and albedo, an ignition hohlraum's $\eta_{CE}\eta_{HR\text{-}cap}$ will be ~1.04±0.12 of coupling predicted by our simulations. Applying that to the NIF point design gives an estimated coupling of 0.115±0.012 [Ref. 10].

Given coupling that is close to modeling, we can credibly explore ways to increase capsule absorbed energy. Referring to Equation 1, we can increase capsule energy by increasing η_{CE}, $\eta_{HR\text{-}cap}$, and/or E_{NIF}. In the section below, we describe improvements to the hohlraum that allow us to increase the overall hohlraum coupling efficiency $\eta_{CE}\eta_{HR\text{-}cap}$. In the section "Increasing E_{NIF}," we describe strategies that allow us to increase the laser energy.

Improving Hohlraum Coupling Efficiency

The energy that a capsule absorbs is just one part of the overall hohlraum energy balance. For a given amount of total x-ray production in the hohlraum, $\eta_{CE}(\eta_{abs}E_{NIF})$, we can write

$$\eta_{CE}(\eta_{abs}E_{NIF}) =$$

$$E_{WALL} + E_{LEH} + E_{CAP} =$$

$$(E_{WALL}/E_{CAP} + E_{LEH}/E_{CAP} + 1)E_{CAP} \quad (2)$$

where E_{WALL} is the the x-ray energy absorbed by the high-Z walls of the hohlraum (a diffusive, radiative heat flow) and E_{LEH} is the radiation losses through the laser entrance hole (LEH). We use ratios in Equation 2 to emphasize that we can increase capsule coupling by decreasing the fractional energy absorbed by the wall relative to the capsule absorption, and by decreasing the fractional energy that escapes the LEH relative to the capsule absorption. Since the wall losses are proportional to the hohlraum area, we can reduce E_{WALL}/E_{CAP} by making changes that decrease the heat flow/unit area as well as by decreasing the total area of the wall while leaving the capsule size fixed (the need to maintain good implosion symmetry limits the degree to which we can shrink the hohlraum). Similarly, we can reduce E_{LEH}/E_{CAP} by decreasing the area of the laser entrance hole while leaving the capsule size fixed. Finally, we note that hohlraum improvements that either directly or indirectly increase x-ray conversion efficiency η_{CE} or hohlraum absorption η_{abs} will also increase E_{CAP}.

To understand the improvements that can be made to ignition hohlraum coupling efficiency, consider as a case study a target based on a 600-kJ variant of a

250-eV target with a beryllium ablator[1] as shown in Figure 2. This capsule has an outer radius of 1.77 μm and produces 70–120 MJ of yield, depending on the detailed drive profile and the amount of DT fuel assumed. We can drive this target with a continuous radiation temperature vs time as shown in Figure 3. At 600-kJ absorbed energy, the target is rather forgiving to changes in timing. The capsule produces high yield for drive profiles with plateau-time parameter τ ranging between 11 and 16 ns. The hohlraum size and, therefore, the wall area for this target depends on our choice of "case-to-capsule ratio," $R_{CC} = (A_{hohl}/A_{cap})^{0.5}$. Virtually all the NIF point design work, to date, has been done at $R_{CC} = 3.65$. This case:capsule ratio would place the capsule in a hohlraum 8.8 mm diameter and ~13.3 mm long (this is approximately a 5.55× scale-up of a standard Nova hohlraum, or "scale 5.55"). Standard NIF design practice calls for the laser entrance holes to have a diameter of 50% of the hohlraum diameter.

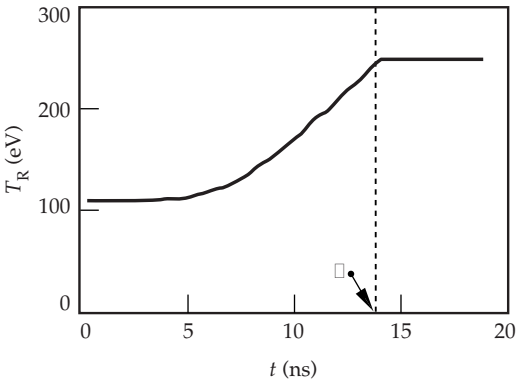

FIGURE 3. The 250-eV Be capsule can be driven with a continuous pulse shape parameterized by a "plateau time" τ. The functional form is $T^4 = T_0^4 + (T_F^4 - T_0^4)(t/\tau)^n$ for $t < \tau$. $n = 5$ typically allows ignition over the widest range of τ. (NIF-0401-02048pb01)

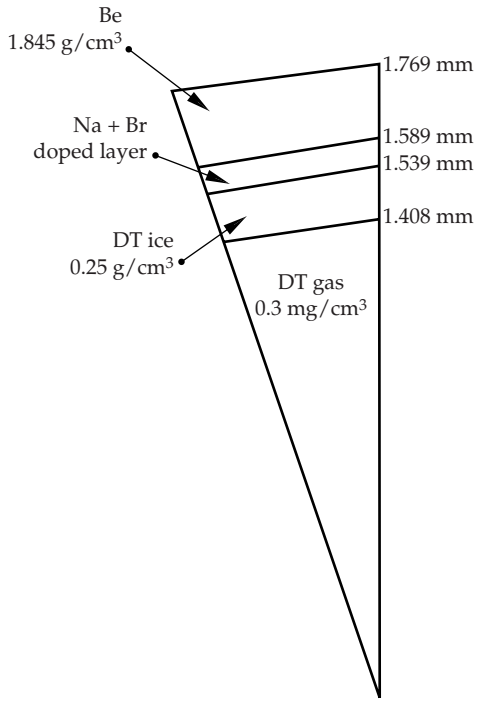

FIGURE 2. Be ignition capsule designed to operate at 250 eV. The 50-μm-thick doped layer next to the DT ice is Be with 2% (atomic fraction) Na and 0.4% Br on the inside of the layer, linearly decreasing to 0.5% Na and 0.1% Br on the outside of the layer. The yield is ~75 MJ with the amount of DT ice shown and the pulse shape of Figure 3. By increasing the ice thickness and adjusting the pulse shape, yields up to 120 MJ are achieved in simulations. (NIF-0401-02047pb01)

Had we examined this 600-kJ capsule in the early '90s when we were first exploring NIF possibilities, we would have concluded the capsule/hohlraum combination requires too much energy. At that time we would have assumed pure gold walls, a scale 5.55 hohlraum and 50% laser entrance holes. The energy budget for this target, Case A in Table 1, shows that it requires 3.3 MJ of x-rays. In the early '90s, when there was considerable uncertainty about hohlraum physics, we hoped that hohlraum x-ray conversion efficiency might be as high as 70%. Using that value, we would have concluded that this target would require ~4.7 MJ of laser energy—well beyond our expectations for NIF.

However, there are several improvements that can be made to the hohlraum

TABLE 1. Energy budget for three different assumptions of hohlraum wall material, laser entrance hole, and conversion efficiency. Capsule-absorbed energy remains fixed.

	Case A	Case B	Case C
E_{WALL}(MJ)	1.8	1.2	0.95
E_{LEH} (MJ)	0.9	0.55	0.4
E_{CAP} (MJ)	0.6	0.6	0.6
Total x-rays (MJ)	3.3	2.35	1.95
CE	0.7	0.9	0.9
Laser energy (MJ)	4.7	2.6	2.2

coupling. Wall losses/unit area can be significantly reduced by using hohlraums made of material mixtures. The basic idea is simple: single materials have opacity that is quite high in some parts of the x-ray spectrum but low elsewhere in the spectrum. Radiation will preferentially flow through these opacity "holes." However, by making the walls from mixtures of complementary materials these opacity holes can be filled in.[15-17] For example, experiments on Nova showed that ~240-eV radiation will flow through a mixture of gold and gadolinium more slowly than through pure gold.[16] The increase in Rosseland opacity inferred from the measurements is close to what was expected from theory.

For ignition pulse shapes that span a very large range in temperature, very significant decreases in wall losses can be achieved by using mixtures of several materials. For example, Figure 4 shows wall loss vs time for three different wall materials exposed to the T_R vs time of Figure 3. These estimated wall losses were calculated with the LASNEX[18] code using an average atom[19] of an atomic physics model. The losses plotted in Figure 4 correspond to the area of a scale 5.55 Nova hohlraum made out of the indicated materials. Mixtures can very significantly reduce losses throughout the pulse, including the foot of the pulse. Quantitatively, wall losses ~2/3 that of pure Au may be possible. Also shown in Figure 4 are plots of wall albedo vs time for a pure Au wall and the cocktail mixture. At early times there can be a very significant increase in albedo that not only saves energy but also serves to reduce the hot-spot:wall emission ratio. This, in turn, should reduce both intrinsic asymmetry and random asymmetry due to laser beam power imbalance.[20]

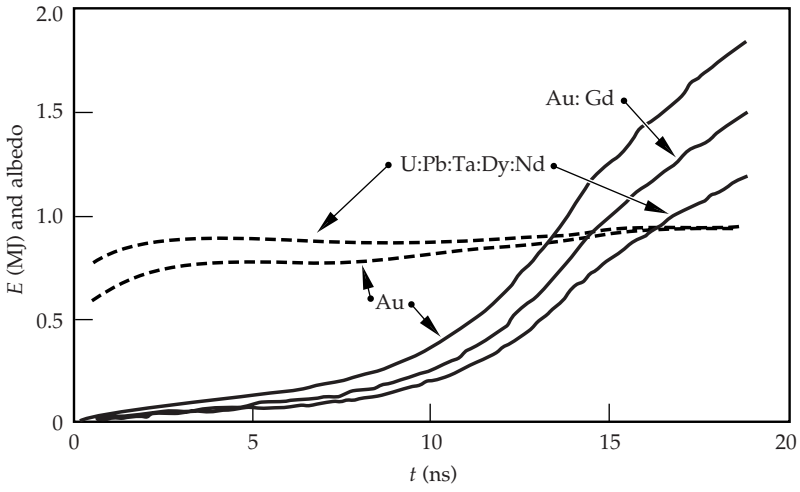

FIGURE 4. Solid lines: x-ray energy (MJ) absorbed by walls of various materials vs time when exposed to the temperature vs time of Figure 3. Area of all three corresponds to that of a scale 5.55 hohlraum. Dotted lines: albedo vs time for gold and for a multicomponent cocktail. (NIF-0401-02049pb01)

Table 2 lists a variety of cocktail mixtures we have explored and, in the second column, our estimated wall losses for the 600-kJ case-study capsule in a hohlraum with R_{CC} = 3.65. The third column shows the ratio of a given mixture's estimated wall loss to that of gold. The final row in the table is an estimate of the lower bound to wall loss, found by forcing the Rosseland opacity of a Z = 75 wall to be equal to the Bernstein-Dyson upper bound of opacity.[21] Although this suggests that further improvements may be found, it must be recalled that the Bernstein-Dyson limit is a very extreme upper bound.

Equation 2 also shows that we can also increase E_{CAP} by decreasing the energy lost through the laser entrance hole. In a hohlraum of fixed case:capsule ratio that means that we must decrease the laser entrance hole diameter from its standard value of 50% of the hohlraum diameter. There are at least two techniques for accomplishing this. One is to simply make the holes smaller. The other is to allow the holes to partially close as high-Z blowoff moves inward from the rim of the LEH. Our current work utilizes the latter technique. In our two dimensional (2D) LASNEX simulations of ignition hohlraums, we find that the simulated laser entrance holes partially close if we do not coat them with a low-Z layer (as was used in the original designs,[1] where it was assumed that hole closure should be avoided). The x-radiation losses through the LEH of all our integrated simulations of ignition hohlraums are consistently 50–60% of the losses we would expect from $\sigma T_R(t)^4 A_{geometric}$, where $T_R(t)^4$ is the radiation flux that is imploding the

TABLE 2. A variety of mixtures of materials can reduce x-ray wall losses to ~2/3 that of pure Au.

Material	Wall loss (kJ)	Wall loss/Au
Au	1850	1.00
Au:Gd	1540	0.83
U:At:W:Gd:La	1200	0.65
U:Bi:W:Gd:La	1200	0.65
U:Bi:Ta:Dy:Nd	1170	0.63
Th:Bi:Ta:Sm:Cs	1250	0.68
U:Pb:Ta:Dy:Nd	1170	0.63
U:Ta:Dy:Nd	1240	0.67
U:Au:Ta:Dy:Nd	1190	0.64
U:Au:Ta:Dy:Nd	1220	0.66
$U:Nb_{.14}$:Au:Ta:Dy	1230	0.66
Bernstein-Dyson	800	0.44

capsule, $A_{\text{geometric}}$ is the initial area of the LEH, and σ is the Stefan-Boltzmann constant. This corresponds to decreasing the effective LEH diameter from the standard 50% of the hohlraum diameter to ~35–40% of the hohlraum diameter. Independent calculations of LMJ ignition hohlraums by French researchers using their 2D code FCI-2 corroborate this finding.[22] The "automatic" decrease in the fractional LEH loss $E_{\text{LEH}}/E_{\text{cap}}$ reduces our case study's x-ray requirement by 350 kJ. Note that although the fractional diameter of the LEH may have decreased from 50% to 35–40% of the hohlraum diameter, the actual size of the hole in our case study is larger than the standard point design's[1,7] because the hohlraum is bigger.

The potential benefits of reducing the specific wall losses via cocktails and allowing the laser entrance hole to close to 60% of its geometric area are summarized in Table 1 as Case B. We see that these two changes reduce the x-ray energy requirement to ~2.35 MJ. Additionally, we can achieve further savings of x-ray energy by shrinking the hohlraum size while keeping the capsule fixed; i.e., reduce R_{CC}. Case C in Table 1 is for a hohlraum where we decreased R_{CC} to 3.28 (=90% of the conventional 3.65 value). The total x-ray requirements drop to ~2 MJ.

We convert hohlraum x-ray energy requirements to laser energy requirements by dividing by the average x-ray conversion efficiency. We mentioned above that in the early '90s we had hoped that the hohlraum x-ray conversion efficiency would be as high as 70%. Since then a broad range of experiments and the associated modeling have shown that hohlraum x-ray conversion efficiency can, in fact, be as high as 85% in Nova hohlraums.[9] In the 1D and 2D simulations of the ignition hohlraums described here, we find effective conversion efficiencies of approximately 90%. As described in Reference 9, such high conversion efficiencies are a result of the confined nature of the system; plasma blowoff energy that would be lost in open geometry remains in the hohlraum where it can "find" its way into becoming radiation. Using 90% conversion efficiency, the estimated laser requirements for Cases B and C of Table 1 are 2.6 and 2.2 MJ, respectively. This, as we shall see, puts such a target within NIF's design performance envelope.

Integrated Design Analysis

In addition to x-ray and laser energy estimates, as summarized by Table 1, our analysis of the hohlraums's x-ray budget also produces x-ray power requirements that we readily convert to laser power requirements using estimated time-dependent conversion efficiency. We validate and refine these laser power estimates with 1D and 2D LASNEX integrated simulations[1,7,14] that include detailed hohlraum specifications, wall materials, capsule, and laser irradiation. Figure 5 shows a laser

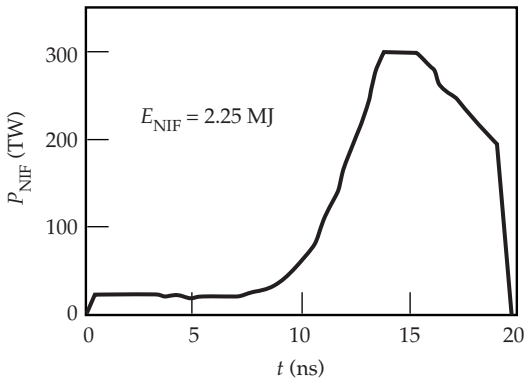

FIGURE 5. Laser power (which drives a 600-kJ, 250-eV capsule inside a scale 5.0 hohlraum made with cocktail walls) vs time.
(NIF-0401-02050pb01)

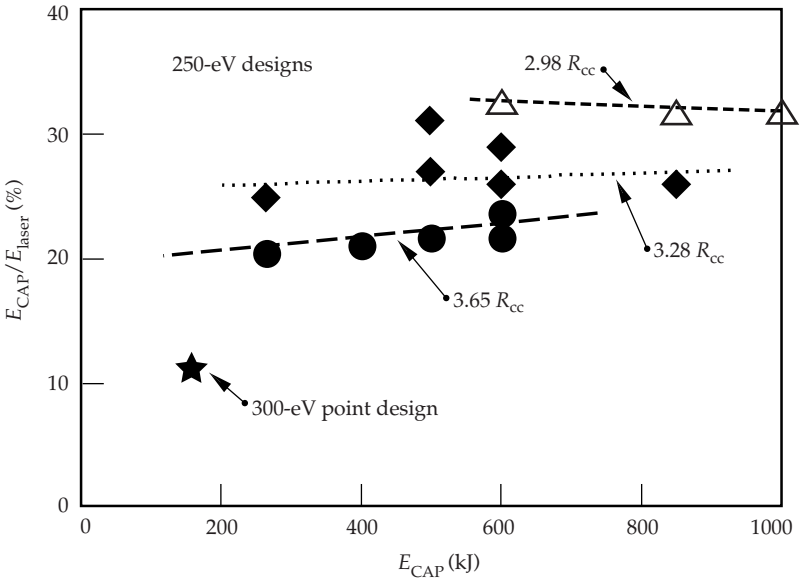

FIGURE 6. Hohlraum coupling efficiency ($\eta_{CE}\,\eta_{HR\text{-}cap}$) vs capsule-absorbed energy for various scales of the 250-eV Be capsule. The coupling efficiency ranges between 20 and 33%, depending on the case:capsule ratio. (NIF-0401-02051pb01)

power that successfully implodes our 600-kJ case-study capsule in a scale 5.0 hohlraum (R_{CC} = 3.28) made of cocktail materials such as the ones listed in Table 2. It has a total energy of 2.25 MJ. The yield from our 2D simulations of this target, which include the effect of time-dependent 2D asymmetries and non-Planckian spectra, is 65–70 MJ; comparable to the 75–80 MJ found for this capsule in 1D simulations using the Planckian drive of Figure 3. Although these design simulations at R_{CC} = 3.28 do show a somewhat greater tendency for an axial jet of fuel to develop at late time than is typically found at the more standard R_{CC} = 3.65, the simulated capsules consistently ignite and burn to high yield over a range of tunings.

Besides the 70-MJ–yield capsule, we have also been studying a 115-MJ–yield version of the same 250-eV, Be capsule. It has more DT fuel and is driven on a somewhat lower adiabat (i.e., the foot T_R is 90 eV vs the 110 eV shown in Figure 3). This capsule also absorbs ~600 kJ. It is driven by a 2.55-MJ laser pulse into a hohlraum of the more typical case:capsule ratio, R_{CC} = 3.65. This target consistently produces 110–115 MJ in our 2D simulations that include time-dependent asymmetries, giving a target gain of ~44. Our estimated laser power does not result in a perfect reproduction of the original drive; here the peak hohlraum radiation temperature is ~270 eV vs the 250 eV in the original design. The ease with which we are able to get our 2D simulations of this target to ignite is an indication that targets of this size may indeed be quite robust.

Besides the 600-kJ capsule used for our case study, we have examined scaled versions of this capsule, which absorb between 265 and 1000 kJ of x-rays for R_{CC} ranging between 3.65 and 2.98. Our analysis includes validating the estimated laser power with 1D and 2D integrated simulations. (Here the 2D simulations are done with the capsule flux numerically forced to be uniform. This allows us to rapidly assess the energetics of an extensive range of hohlraums without also needing to simultaneously control symmetry.) Figure 6 summarizes the hohlraum coupling efficiency, $\eta_{CE}\eta_{HR\text{-}cap}$ of Equation 1, for this survey. At the standard case:capsule ratio, cocktails and slightly reduced LEHs together with longer pulse lengths combine to produce coupling efficiencies ~20–22% vs the ~11% of the original point design. If we can successfully reduce the case-to-capsule ratio without introducing unacceptable asymmetry, then couplings ~26–28% are plausible at R_{CC} = 3.28 and ~30–33% at R_{CC} = 2.98.

In evaluating the increase of hohlraum coupling efficiency from ~11% to ~25%,

we find that it is due to the simultaneous combination of many relatively small improvements. We cannot point to any one key change. The steady accumulation of small improvements is summarized in Table 3. This collection of modest improvements produces, in concert, more than a factor of 2 increase in overall hohlraum coupling.

Increasing E_{NIF}

NIF is a glass laser that is capable of producing up to ~4.8 MJ (4MJ) of 1-µm (infrared) wavelength laser light when it is completed with 7 (5) slabs of glass in the final booster amplifiers. (The number of slabs that will ultimately be installed is under discussion. The amplifiers being built will accommodate seven.) This 1-µm light is converted to the 1/3-µm (blue) light used to irradiate hohlraums in the final optics assembly (FOA), where it is also focused and aimed onto the target. Two fundamental questions that must be answered in order to assess NIF's capability to produce any given pulse shape are:

1. Is there enough 1-µm light to create the needed blue pulse shape?
2. If so, how much "damage" will the blue light cause in the FOAs?

The answer to the first question depends not only on the intensity-dependent conversion efficiency of the potassium dihydrogen phosphate (KDP) crystals (which convert the infrared light to blue light) but also on the operational strategy that we use to produce a given pulse shape at the target. In the case of the 2.25-MJ pulse shape of Figure 5, if we elect to generate it by simply running an appropriately shaped, continuous 1-µm pulse shape through the KDP crystals, then we find that we need 4.5 MJ of 1-µm laser light. This is well within the energetics capability of NIF with seven booster slabs but not with five. However, there are operational strategies for significantly reducing the 1-µm requirements. These strategies are all based on the "picket fence" approach,[23] which replaces a continuous pulse with a train of short, high-power pulses that convert to blue light much more efficiently in the KDP crystals during the low-power, early time "foot" of the pulse. Now there is a concern, based on simulations, that hohlraums irradiated by widely spaced pickets will have symmetry problems related to cooling of the hohlraum's bulk plasma between pickets. However, it is possible to take advantage of NIF's architecture to produce temporally skewed pickets that convert well in the KDP crystals but provide a continuous pulse after being focused onto the target.[24] Moreover, by taking advantage of NIF's architecture in which a "quad" (a 2×2 array of four beams) can be treated as a single beam that irradiates the hohlraum, it is possible to interleave four relatively short pulses from each of the four beams to form a continuous pulse. Using techniques such as this, we can envision average 1/3-µm conversion efficiencies as high as 70%, as measured at the target. For the pulse shape of Figure 5, this "ultrafast picket" technique could lower the 1-µm energy requirement to ~3.5 MJ. Indeed, such advanced conversion schemes allow us to contemplate even larger capsules. Table 4 summarizes 1/3-µm and 1-µm energy requirements for several targets. Using advanced conversion schemes and reduced case:capsule ratios, we can consider driving capsules that absorb as much as 1 MJ of x-rays.

The second fundamental question about a given pulse shape is how much "damage" will it cause in the FOA? A basic problem is that surface imperfections will slightly

TABLE 3. Hohlraum efficiency can be significantly increased by a combination of many relatively small improvements.

Hohlraum	Efficiency (%)
300 eV, 150 kJ, 3 ns	11
250 eV, 600 kJ, 7.5 ns	14.5
Reduce LEH only	16.2
Cocktails only	17.7
Both cocktails and reduced LEH	20.3
CE rises from ~80% to ~90%	22.9
Reduce R_{cc} by 10%	25.3

TABLE 4. One-μm energy needed to drive various targets, assuming two different operational strategies, and 1/3-μm damage integral for each target's pulse shape.

Target E_{CAP}/Yield/R_{cc}	1/3-μm energy (MJ)	1-μm energy CW pulse (MJ)	1-μm energy fast pickets (MJ)	Damage integral (J/cm^2 3 ns equiv)
600 kJ/70 MJ/3.28	2.25	4.5	3.5	7.2
600 kJ/120 MJ/3.65	2.55	5	3.9	7.8
850 kJ/150 MJ/2.98	2.65	5.1	4	7.8
1000 kJ/380 MJ/2.98	3	6	4.5	8

absorb blue light causing local heating. Too much heating produces local damage. The figure of merit for this process, known as the "damage integral," increases with fluence (J/cm^2) but decreases with pulse length as $1/t^{0.5}$, since heat can diffuse away from the absorbing imperfections. NIF's specification for damage integral is 8 J/cm^2, 3 ns Gaussian equivalent. This means that a 3-ns Gaussian pulse of 8 J/cm^2 passing through the FOA would be acceptable. Likewise, the $t^{0.5}$ scaling means a 12-ns pulse of 16 J/cm^2 could also be acceptable. For an arbitrary pulse shape,[25]

$$\text{Damage integral} = 1.1 \times \int_0^t \frac{I(s)}{\sqrt{t-s}}\,ds \qquad (3)$$

where I is the blue-light intensity in units of GW/cm^2, t and s are in ns. The final column in Table 4 lists the damage integral values for several higher absorbed energy designs. All are within NIF's 8 J/cm^2 3 ns Gaussian equivalent damage specification.

Discussion

The 600-kJ capsule driven at 250 eV that we used as a case study is part of a larger study exploring the limits of capsule coupling energy. This work indicates that NIF may be able to drive some surprisingly energetic targets. Figure 7 is an "engineering plot" that summarizes our findings at 250 eV. It relates capsule absorbed energy to laser performance. The solid lines represent the three case:capsule ratios we studied: R_{CC} = 3.65, 3.28, and 2.98. The broken line at the upper right shows where we would run out of 1-μm energy using an advanced pulse-shaping technique such as the ultrafast pickets described above. At

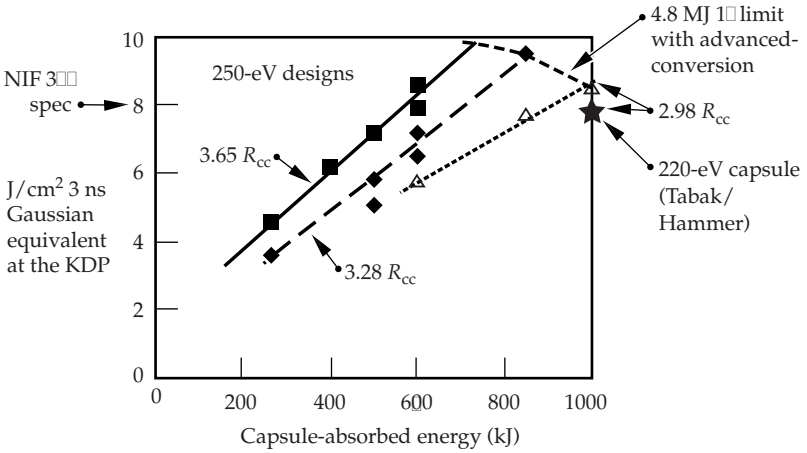

FIGURE 7. Energy absorbed by the 250-eV capsule vs 3ω damage integral (cf Equation 3). Solid lines indicate three different case:capsule ratios. Broken line indicates the limit set by NIF's available 1-μm energy, assuming seven booster amplifier slabs and advanced conversion schemes. NIF's design specification for 3ω damage integral is "8 J/cm^2 3 ns Gaussian equivalent." (NIF-0401-02052pb01)

R_{CC} = 3.65, we may be able to implode a capsule that absorbs 600 kJ before exceeding NIF's 8-J/cm^2 blue-light fluence specification. If we can successfully implode capsules in hohlraums with reduced case:capsule ratio, then absorbed energies approaching 800 kJ to 1 MJ are possible. The star on the plot indicates one 220-eV target we investigated. It is based on a 1000-kJ absorbed energy capsule that produced 380 MJ of energy.[26]

Although we allow the laser entrance hole to close to ~80% of its initial diameter, it is important to realize that these hohlraums are bigger than the typical point design hohlraum[1,7] (a scale 3.45 hohlraum). Consequently, the laser entrance holes are bigger, even after the partial closure. This, coupled with a lower peak power (~300–350 TW vs 450 TW) leads to the prospect of relatively low intensities in the LEH; ~2–4×10^{14} W/cm^2 may be possible.

Returning to Figure 7, we see that at 250 eV, there is a reasonably good match between NIF's damage specification and the 1-µm light potentially available. Figure 8 is a similar plot for 300-eV targets, based on a Cu-doped Be capsule design.[27] At 300 eV we find some mismatch between the damage specification and the 1-µm energy potentially available. We are beginning to explore ways to possibly redress this mismatch, including evaluating the use of green light, which is believed to have a damage limit considerably higher than that of blue light.

Finally, Figure 9 is a plot of yield vs capsule-absorbed energy, which demonstrates

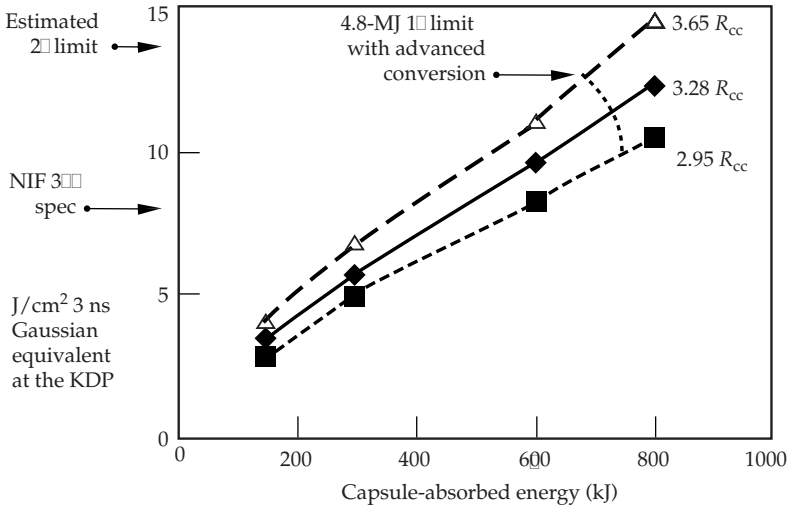

FIGURE 8. A similar plot to Figure 7 but for a capsule driven at 300 eV. (NIF-0401-02053pb01)

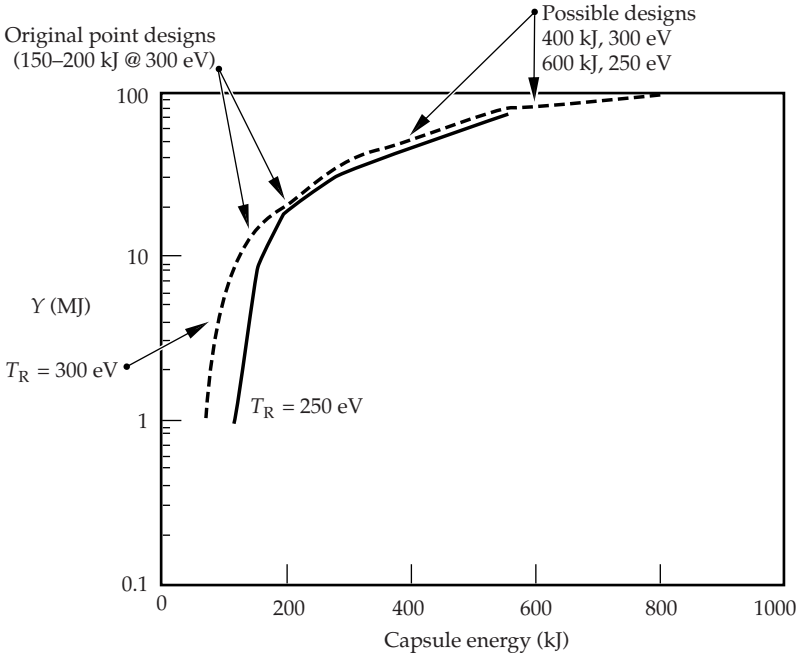

FIGURE 9. Yield vs capsule-absorbed energy from 1D simulations of a capsule driven at 250-eV peak radiation temperature and a capsule driven at 300 eV. Significantly increasing the capsule-absorbed energy will move us away from the ignition "cliff," thereby providing a more robust target.
(NIF-0401-02054pb01)

some of the benefits of increased absorption. We see that a factor of two to four increase in absorption over the original 150–200 kJ moves us much further from the "cliff" where the penalty for small errors in understanding can be very large. These increases in absorbed energy can also very significantly increase the capsule yield.

Acknowledgments

Much of this work was engendered during an evening's discussion with R. Kauffman and L. Powers. We would like to acknowledge useful discussions with J. Lindl, B. Hammel, M. Tabak, and J. Edwards. We would like to thank E. M. Campbell, in particular, for his enthusiastic support and encouragement.

Notes and References

1. S. W. Haan, S. M. Pollaine, J. D. Lindl, et al., *Phys. Plasmas* **2**, 2480 (1995).
2. J. A. Paisner, E. M. Campbell, and W. J. Hogan, *Fusion Technol*. **26**, 755 (1994).
3. J. T. Hunt and D. R. Speck, *Opt. Eng.* **28**, 461 (1989).
4. J. M. Soures, R. L. McCrory, C. P. Verdon, et al., *Phys. Plasmas* **3**, 2108 (1996).
5. M. Andre, M. Novaro, and D. Schirmann, "Technologie pour un Laser Megajoule," *Review Scientifique et technique de la direction des applications militaires*, Chocs, Numero 13, 73, Avril 1995.
6. See, for example, W. Kruer, *The Physics of Laser Plasma Interactions* (Addison-Wesley, New York, 1988).
7. W. J. Krauser, N. M. Hoffman, D. C. Wilson, et al., *Phys. Plasmas* **3**, 2084 (1996).
8. B. J. MacGowan, R. L. Berger, S. I. Glenzer, et al., "Laser Beam Smoothing and Backscatter Saturation Processes in Plasmas Relevant to National Ignition Facility Hohlraums," *Proceedings of the 17th IAEA Fusion Energy Conference*, Yokohama, Japan (October 1998), International Atomic Energy Agency, Vienna.
9. L. J. Suter, R. L. Kauffman, C. B. Darrow, et al., *Phys. Plasmas* **3**, 2057 (1996).
10. L. J. Suter et al., "Status of Our Understanding and Modeling of Ignition Hohlraum X-Ray Coupling Efficiency," *ICF Quarterly Report* **8** (4), 171–178, Lawrence Livermore National Laboratory, UCRL-LR-105821-98-4 (1998).
11. R. L. Kauffman, L. J. Suter, C. B. Darrow, et al., *Phys. Rev. Lett*. **73**, 2320 (1994).
12. A. Hauer et al., *Rev. Sci. Instrum*. **66**, 672 (1995).
13. P. Amendt et al., *Phys. Plasmas* **4,** 1862 (1997).
14. L. J. Suter et al., *Phys. Rev. Lett*. **73**, 2328 (1994).
15. H. Nishimura et al., *Appl. Phys. Lett*. **62**, 1344 (1993).
16. T. J. Orzechowski, M. D. Rosen, H. N. Kornblum, et al., *Phys. Rev. Lett.* **77**, 3545 (1996).
17. D. Colombant, M. Klapisch, and A. Bar-Shalom, *Phys. Rev. E* **57**, 3411 (1998).
18. G. B. Zimmerman and W. L. Kruer, *Comments Plasma Phys. Controlled Fusion* **2**, 51 (1975).
19. D. E. Post et al., *Atom. Data Nucl. Data Tables* **20**, 397 (1977).
20. O. J. Jones, Lawrence Livermore National Laboratory, Livermore, CA, private communication (1999).
21. See, for example, J. Bond, K. Watson, and J. Welch, *Atomic Theory of Gas Dynamics* (Addison-Wesley, New York, 1965) p. 371.
22. E. Dattolo, CEA Bruyeres-Le-Chatel, France, private communication (1999).
23. D. J. Kuzienga, *Opt. Commun*. **22**, 156 (1977).
24. J. Rothenberg, Lawrence Livermore National Laboratory, Livermore, CA, private communication (1999).
25. J. Trenholm, Lawrence Livermore National Laboratory, Livermore, CA, private communication (1998).
26. J. H. Hammer et al., *Phys. Plasmas* **6**, 2129 (1999).
27. T. R. Dittrich et al., *Fusion Technol*. **31**, 402 (1997).

On the Accuracy of X-Ray Spectra Modeling of Dense Inertial Confinement Fusion Plasmas

S. H. Glenzer *B. A. Hammel*

K. B. Fournier *R. W. Lee*

B. J. MacGowan

We have tested spectroscopic modeling of the helium-like and lithium-like argon x-ray emission in dense gasbag plasmas by comparing measured spectra with kinetics calculations using plasma parameters that have been accurately measured with Thomson scattering. In particular, we have measured the line radiation in the wavelength region of the He-like Ar $1s^2 - 1s3\ell$ transition (He-β). This spectrum is of interest to diagnose gas targets, $n_e \sim 10^{21}$ cm^{-3} (Refs. 1–3), laser ablation plasmas, $n_e \sim 10^{22}$ cm^{-3} (Ref. 4), and has previously been applied to diagnose electron densities and temperatures of inertial confinement fusion (ICF) capsule implosions, $n_e \sim 10^{24}$ cm^{-3} (Refs. 5,6).

The ICF implosions produce plasma conditions of extremely high densities similar to those of stars and therefore require x-ray emission or neutron diagnostics.[7] The spectrum of the He-β transition of Ar XVII together with its dielectronic satellites arising from the Li-like Ar states $1s^2\ n\ell - 1s\ n\ell\ n'\ell'$, referred to below as the He-β complex, has been found to be a valuable diagnostic of electron densities and temperatures. The He-β line is Stark-broadened so that densities can be inferred from the width of the spectral line. Moreover, the upper states of the observable dielectronic satellites on the red wing of the He-β line are predominantly populated by dielectronic recombination so that their relative intensity is sensitive to the electron temperature.[8,9] Some of the higher-n satellite features overlap with the He-β transition and consequently need to be self-consistently included in the fit of the whole line shape with a Stark-broadening code coupled to a kinetics (collisional-radiative) model.[10,11] This procedure applies kinetics modeling to very high densities where the codes have not been tested against independent measurements. In this study, we perform critical comparisons of kinetics calculations with experimental data from well-characterized plasmas at the highest possible densities where independent optical diagnostics, i.e., Thomson scattering, can be used to measure the electron temperature.[12,13] This is a necessary first step toward a critical evaluation of the diagnostic procedures used at the highest measured plasma density of $n_e > 10^{24}$ cm^{-3}.

We have performed our experiments in well-characterized gasbag plasmas at densities $n_e = 0.6 \times 10^{21}$ cm^{-3} and $n_e = 1.1 \times 10^{21}$cm^{-3}. The densities of these gasbag plasmas are independently diagnosed with stimulated Raman scattering,[1] and the electron temperatures are measured with temporally and spatially resolved Thomson scattering.[13] The Thomson scattering measurements indicate that the gasbags are homogeneous with slowly increasing electron temperatures during the first 0.6 ns of the 1-ns-long heater beam pulse. These data are also consistent with hydrodynamic LASNEX modeling[14] suggesting that gasbag plasmas are suitable sources to test our kinetics modeling capability.

To compare the experimental spectra with synthetic spectra, we employ the HULLAC suite of kinetics codes.[15] We find for the two different electron densities that the kinetics modeling accurately predicts the intensity ratio of the Li-like dielectronic capture satellite transitions and of the He-β transition (consisting of the sum of the resonance line, He-β_1: $1s^2\ {}^1S_0 - 1s3p\ {}^1P^0{}_1$, and the less intense intercombination line from the triplet to the singlet system of He-like argon, He-β_2: $1s^2\ {}^1S_0 - 1s3p\ {}^3P^0{}_1$). On the other hand, spectral line emission originating from levels whose population is primarily determined by electron collisional processes shows discrepancies of up to a factor of two compared to the modeling. In particular, this is observed for inner-shell excited satellite transitions that are populated from the Li-like ground state. We have examined possible explanations for this discrepancy and found that the most likely one is errors in the calculated ionization balance between the He- and Li-like state.

In spite of these remaining discrepancies between calculated and measured inner shell satellite intensities, the fact that the strongest satellite features (the dielectronic capture satellites) are well modeled by the HULLAC code may affect the interpretation of ICF capsule implosions experiments. Our findings indicate that we should revisit the analysis of the higher density implosions to find if the kinetics modeling is consistent with the results obtained here. Preliminary calculations for implosion conditions show that various kinetics codes result in a factor of two different prediction for the ratio of the capture satellites to the He-β transition. More analysis using line shape calculations will be required to investigate whether the previous interpretation of spectra from capsule implosions is affected.[6] Moreover, having proven the technique to benchmark kinetics calculations in laser-produced plasma conditions, one can hope to extend this method to verify critically important aspects of indirectly driven capsule physics by testing the conditions created inside of ICF hohlraums.

Experiment

The experiments were performed with the Nova laser facility at the Lawrence Livermore National Laboratory.[16] This Nd:glass laser was operating at 1.055 μm (1ω) and could be frequency converted to 3ω with energies of ~30 kJ. The application of these large laser energies has enabled us to produce large-scale–length and extremely homogeneous plasmas ($\Delta T_e/T_e$ < 20%). We used nine $f/4.3$ laser beams to illuminate gasbag targets from all sides. Gasbags consist of two 0.35-μm-thick polyimide ($C_{14}H_6O_4N_2$) membranes that are mounted on either side of a 0.4-mm-thick aluminum washer with an inner diameter of 2.75 mm (Figure 1). In this study, the membranes have been inflated with propane (C_3H_8) or neopentane (C_5H_{12}) plus a small amount of Ar (1% by atomic number in each case) as a spectroscopic test element. The concentration of Ar atoms of 1% was chosen to obtain optically thin conditions for the Li- and He-like Ar emission.The heater beams provided 2.3-kJ energy per beam at

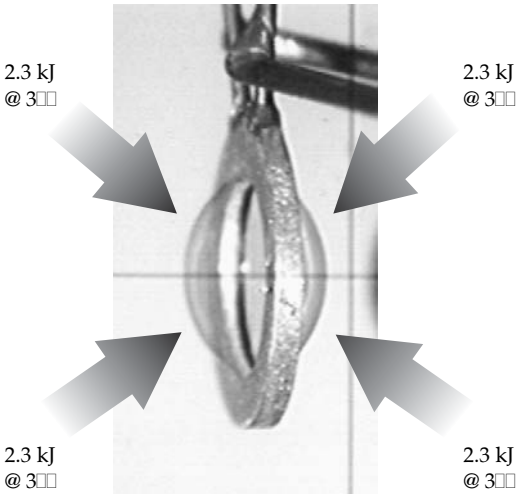

FIGURE 1. Gasbag target before it was pressurized with C_3H_8 or C_5H_{12}. The thickness and the inner diameter of the washer were 0.4 mm and 2.75 mm, respectively. The gasbags were heated with nine 1-ns-long heater beams of 2.3 kJ per beam at 3ω. (NIF-0401-02069pb01)

3ω (λ_0 = 351 nm) in a 1-ns-long square pulse. A diverging focus resulted in an intensity of $I = 10^{14}$ W cm^{-2} on target.

The x-ray spectra have been measured with a crystal spectrometer[17] coupled to a gated microchannel-plate detector (MCP).[18] The x-ray emission is observed through a slit cut in a copper shield and mounted on the target at a distance of 8 mm, effectively limiting the plasma size seen by the spectrometer. This slit allows a view through the gasbag center. We used a pentaerythritol (PET) crystal to spectrally disperse the plasma emission and detected the spectra with the MCP detector with a temporal resolution of 80 ps, a spatial resolution of 22 μm, and a resolving power of $\lambda/\Delta\lambda = 800$. Examples of the spectra measured in this way are presented in the next section. The gated MCP detector was further employed for 2D x-ray imaging of the gasbag emission with photon energies of $E > 2$ keV. For this purpose, we used 10-μm pinholes with a Be filter in front of the MCP camera. Figure 2 shows an example of three successive measurements. For early times ($t < 0.3$ ns) during the 1-ns-long heating pulse, the initial imprint of the heater beams can be identified. For $t >$ 0.4 ns, these measurements indicate that the gasbag plasmas become homogeneous.

For a more quantitative investigation of the plasma homogeneity, we measured the electron temperature at various distances from the target center with Thomson scattering. A 50-J, 4ω (λ_0 = 263 nm) probe beam has been used for the Thomson scattering experiments.[13] Due to the strong laser light absorption, stray light, and stimulated Raman side-scattering from the heater beams in the wavelength region around the longer Nd:glass wavelength harmonics: 2ω and 3ω, a short-wavelength probe is required to characterize open geometry large-scale–length ICF plasmas. The probe laser was focused into the gasbag target to a spot of 60 μm × 120 μm resulting in an intensity of $I \sim 3 \times 10^{14}$ W cm^{-2} (at 4ω). In separate experiments, we have shown that this probe does not influence the plasma when it is hot and heated by kJ-laser beams.

The Thomson scattered light has been imaged at an angle of 90° with f/10-optics onto the entrance slit of a 1-m (SPEX) spectrometer. We employed an S-20 streak camera to record spectra with a temporal resolution of 50 ps and a wavelength resolution of 0.05 nm. The imaging setup resulted in a cylindrical scattering volume with a scale length of ~100 μm. The scattering volume is small compared to the size of the plasma. The choice of the probe laser wavelength of 263 nm and of the scattering angle of 90° results in collective Thomson scattering from fluctuations characterized by wave numbers **k** such that the scattering parameter is $\alpha = 1/\mathbf{k}\lambda_D > 2$ for the gasbag electron densities and temperatures. The Thomson

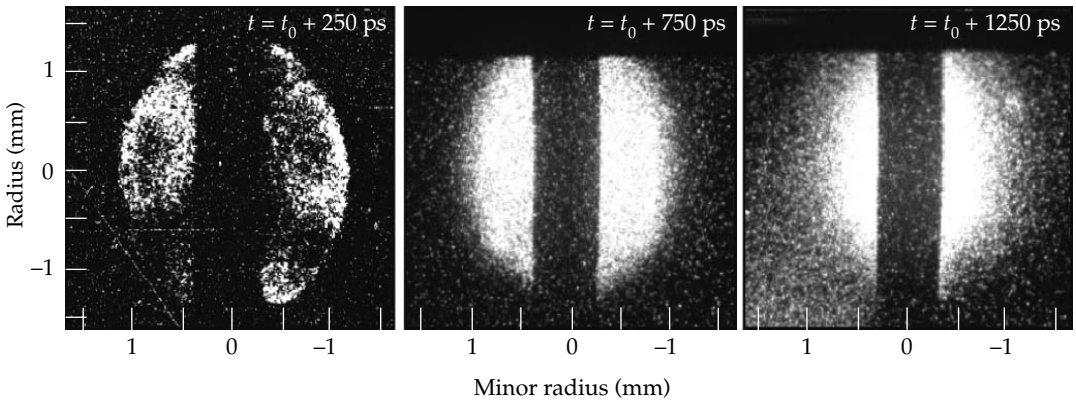

FIGURE 2. Temporally resolved 2D x-ray images of the gasbag emission with energies $E > 2$ keV. The gasbags show a homogeneous emission shortly after the beginning of the heater pulse (for $t > 0.4$ ns). (NIF-0401-02070pb01)

scattering spectra are dominated by the narrow ion feature which shows scattering resonances at the ion-acoustic wave frequencies shifted from the incident probe laser frequency on either side on the frequency scale (redshift and blueshift for waves copropagating and counterpropagating along the scattering vector **k**.

Figure 3 shows an example of Thomson scattering spectra at t = 0.35 ns and t = 0.9 ns measured at a radius of 800 μm from the gasbag center. The electron temperature can be inferred from the frequency separation of the two ion-acoustic peaks. Each peak consists of two unresolved ion-acoustic waves, one belonging to carbon (slow mode) and one belonging to hydrogen (fast mode) giving the ion temperature of the plasma from the relative damping of these waves. With increasing time, the ion-acoustic peaks show increased separation and broadening indicating increasing electron and ion temperatures during the heating of the gasbag plasma. To accurately infer temperatures from these spectra, we convolute the form factor $S(\mathbf{k},\omega)$ for multi-ion species[19] with the experimental instrument function and fit the resulting profile to the data. Examples of these fits are also shown in Figure 3. We obtain an error estimate for the electron temperature of <10% from the fitting procedure by varying the calculated profile within the noise of the experimental data.

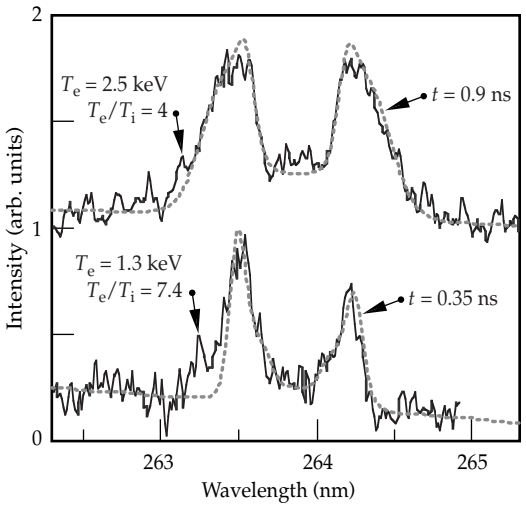

FIGURE 3. Experimental Thomson scattering spectra from a C_5H_{12}-filled gasbag measured from a radial distance of 0.8 mm from the gasbag center. The spectra show increasing electron temperatures and decreasing electron-to-ion temperature ratios. The parameters are inferred from the theoretical fits to the experimental data. (NIF-0401-02071pb01)

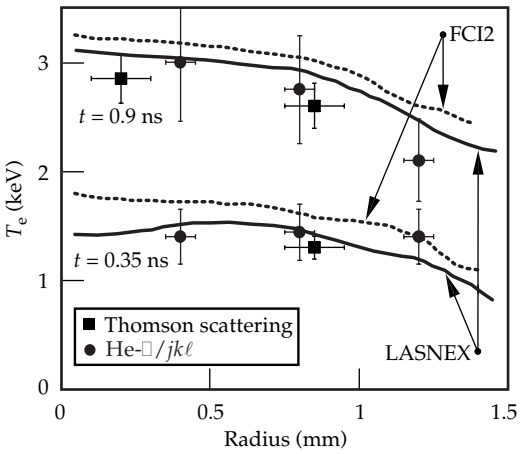

FIGURE 4. Experimental electron temperature data for various radial positions measured at t = 0.35 ns and at t = 0.9 ns. The temperatures from Thomson scattering show excellent agreement with the results from x-ray spectroscopy and are consistent with the hydrodynamic modeling using the codes LASNEX and FCI2. At t = 0.35 ns the electron temperature profile is flat indicating the utility of gasbags for spectroscopic investigations. (NIF-0401-02072pb01)

Figure 4 shows the electron temperature as a function of the radius for two different times during the heating of the gasbag plasma. The experimental data show mutual agreement between the results from the temporally and spatially resolved Thomson scattering technique and with temporally and spatially resolved x-ray spectroscopy using the intensity ratio of the He-like Ar $1s^2 - 1s2\ell$ (He-α) line to the Li-like $jk\ell$ dielectronic satellites.[2] These two techniques are compared together with hydrodynamic LASNEX and FCI2 simulations. The error bars for the spectroscopically derived temperatures are in the range of 15% to 20% depending on the noise amplitude of the individual spectra at various times. The Thomson scattering data are accurate to within 10%. We find that the results of the simulations are close to the experimental data. For this comparison, we include the heater beam scattering losses by stimulated Brillouin and stimulated Raman scattering. The results presented in Figure 4 clearly show a homogeneous plasma at the time of the measurements of the He-β transition plus satellites, i.e., 0.3 ns < t < 0.5 ns, with $\Delta T_e/T_e$ < 20%. At the time

close to peak temperature, i.e., t = 0.9 ns, we find a homogeneous center with a diameter of 2 mm, $\Delta T_e/T_e < 30\%$.

While the electron and ion temperatures in these gasbag plasmas are well known from the measurements described above, the electron density is principally known by the density of the gas fill. Measurements of the wavelength of the Raman scattered light that occurs at the frequency of the electron plasma wave give a value for the electron density that is consistent with the gas fill density.[1] The line intensity ratio of the resonance and intercombination line of He-like Ar has also been shown to be in agreement with the expected densities.[2] In summary, the detailed measurements and the general agreement with the simulations indicate that the plasma conditions in these gasbag targets are known with good accuracy so that it provides a spectroscopic source that is very suitable to test kinetics codes.

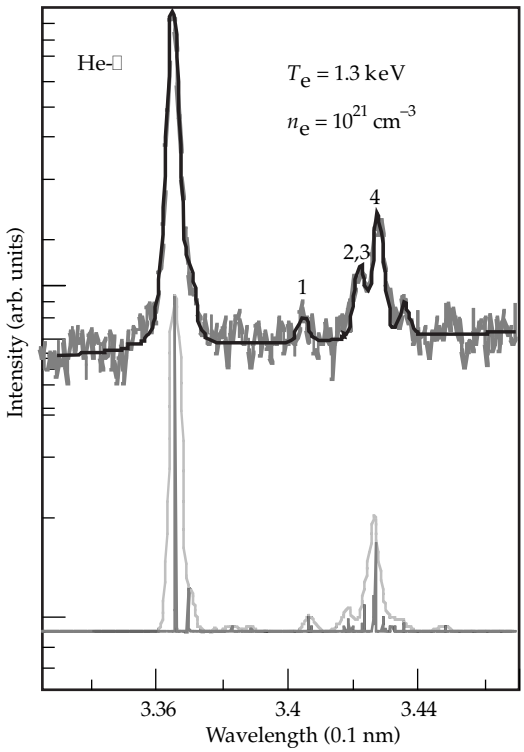

FIGURE 5. Experimental and synthetic spectra of the Ar He-β complex. (NIF-0401-02073pb01)

Experimental Results and Discussion

Figure 5 shows an example of a temporally resolved x-ray spectrum in the wavelength region 0.332 nm < λ < 0.345 nm measured at t = 0.35 ns from a gasbag that has been filled with C_5H_{12} and 1% Ar. The data have been measured spatially resolved along the slit height and averaged over the region r < 1.2 mm to reduce noise. The averaging does not influence the interpretation of plasma conditions because at the time of the measurements the gasbag plasma is homogeneous as shown above. In Figure 5 we also show a synthetic spectrum calculated with the experimental resolution and with a higher resolution using the HULLAC suite of codes for the experimental plasma parameters: T_e = 1.3 keV, $n_e = 1.1 \times 10^{21}$cm^{-3}.

The spectrum is dominated by the 1s – 3p resonance line of He-like argon Ar XVII at λ = 0.3364 nm, He-β, the theoretical transition energy of which has been used to determine the absolute wavelength scale of Figure 5. A number of spectral lines can be identified on the low-energy, or red, wing of the He-β transition. These are the intercombination line at λ = 0.337 nm, dielectronic satellites with a n = 3 spectator electron at λ = 0.3381 nm and four dielectronic satellites with a n = 2 spectator electron labeled 1 through 4 (Refs. 4, 20). For a quantitative comparison between the experiment and the spectra modeling, we fit the experimental data with a multi-Gaussian profile using a least-squares method (Figure 5). We obtain an estimate for the error bar of the experimental intensities of the various spectral lines by varying the fit within the noise of the data. This error is in the range of 5% for the intense transitions (e.g., feature 4) to 20% for the weak transitions (e.g., feature 1). In Figure 5, the n = 3 dielectronic satellites at 0.3381 nm have not been included in the fit since we do not compare it to modeling. However, we verified that the n = 3 feature, as well as n = 4 satellites,[11,20] do not influence the intensity of the He-β line for our conditions.

Figure 6 compares the measured intensity ratio with the results of the HULLAC calculations. It shows the ratio of the

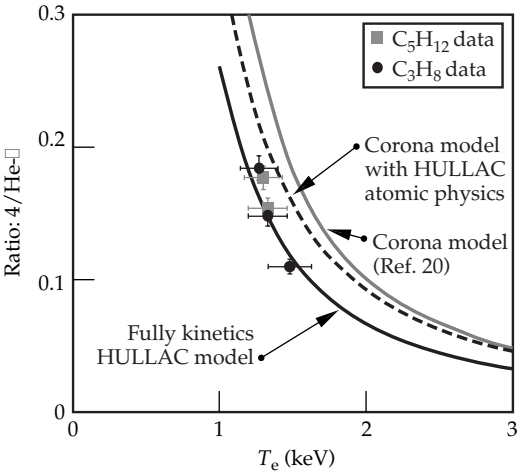

FIGURE 6. Comparison between the experimental line ratios from C_3H_8-filled ($n_e = 6 \times 10^{20}$cm^{-3}) and C_5H_{12}-filled ($n_e = 1.1 \times 10^{21}$cm^{-3}) gasbags with steady-state kinetics (collisional-radiative) modeling. The intensity ratio of the He-β transition (resonance plus intercombination line) to satellite feature 4, whose upper state is populated by dielectronic capture, shows excellent agreement with the fully kinetics modeling. (NIF-0401-02074pb01)

dielectronic capture satellite (labeled 4) to the He-β transition as function of the measured electron temperature for the two different electron densities. The dielectronic capture satellite $1s^2 + e^- \rightarrow 1s\,2\ell\,3\ell'$ is primarily populated by collisional excitation from the He-like ground state and simultaneous capture of a free electron into an excited bound state. This process is known to be sensitive to the electron temperature, and kinetics modeling shows no dependence on electron density for the density range of this study. We find that the experimental data are in excellent agreement with the kinetics modeling if the fully collisional-radiative HULLAC model is used.

The HULLAC calculations[15] include all singly and doubly excited energy levels with principal quantum number n ″ 5. The code generates atomic wave functions using a fully relativistic, parametric potential method that calculates the multiconfiguration, intermediate coupled level energies and radiative transition rates, A. In addition, the code also computes semirelativistic autoionization transition rates to the ground and excited levels of an adjacent ion. The electron-impact excitation rates between all levels of each charge state mentioned above are calculated in the distorted wave approximation. The ionic transition rates include the autoionization rates from the Li- to He-like and He-like to H-like ions, as well as direct, impact ionization and radiative recombination rate coefficients. Radiative recombination from and collisional ionization to the bare nucleus Ar^{18+} are also included. These rates are used to construct the collisional-radiative rate matrix. The inverse of each ionization process, namely dielectronic capture and three-body recombination have been found according to the principle of detailed balance. The relative populations of the four charge states and the population, N, in each level of each ion are then found in steady state.

From these calculations we obtain the intensity of the spectral line emission and thus the intensity ratios shown in Figures 6 and 7. In general, for optically thin plasmas, the intensity of a radiative transition $I_{u\ell}$ from the upper level u to the lower level ℓ is given by the integral of the emission coefficient ε over the plasma path length:

$$I_{u\ell}(\nu) = \int \varepsilon_{u\ell}(\nu, x)\, dx$$

where ε is given by the atomic transition probability $A_{u\ell}$, the population density of the upper atomic state N_u, and a line shape function Φ that is normalized to one if integrated over the whole line profile in frequency space.

$$\varepsilon_{u\ell}(\nu, x) = \frac{h\nu}{4\pi}\, A_{u\ell}\, N_u(x)\Phi(\nu, x)$$

The comparison shows that the HULLAC calculations agree on average within 6% with the experimental intensity of the dielectronic capture satellite. Also shown in Figure 6 are two simplified calculations using a coronal approximation, i.e., for low densities, the population of the upper states is determined by electron collisional excitation from the ground state N_g and de-excitation by radiative transitions.

$$N_u = \frac{N_g\, n_e \langle \sigma\nu \rangle}{\sum A_{u\ell}}$$

These two simplified models,[15,20] which use slightly different estimates for $A_{u\ell}$ and the averaged cross section for electron collisional excitation $<\sigma\nu>$, overestimate the experimental ratio by 12% to 22%. This

comparison indicates that a full kinetics calculation is required to model these spectra. We observe good agreement between the experimental dielectronic capture satellite intensities and the full kinetics model indicating that the populations of atomic states within one ionization stage are well understood.

On the other hand, we find that inner-shell collisional excited satellite lines are not as well modeled. These satellites are excited by collisions of free electrons with ions in the Li-like ionization state: $1s^2\,2\ell + e^- \rightarrow 1s\,2\ell\,3\ell' + e^-$. Figure 7 shows the ratio of the inner-shell excited satellite feature 1 with the fully collisional-radiative HULLAC kinetics modeling.

In this case, we observe discrepancies between the data and the modeling of up to a factor of two. To ascertain the potential effects of the hot electrons and non steady-state populations, we use time-dependent calculations to model the experimental conditions described above. Only for times $t < 0.1$ ns, when there is a significant fraction of Li-like ions in the plasma, do these calculations show that hot electrons increase the collisional excitation and therefore the intensity of the He-β transition as well as the inner-shell collisional excited satellites. However, at later times when the spectra have been measured, i.e., 0.3 ns < t < 0.5 ns, the effect of the hot electrons is found to be negligible because He-like ions begin to dominate the charge state distribution so that thermal electrons dominate the collisional excitation process (e.g., Ref. 21). Further, the same time-dependent calculations show that deviations from steady state are small for the gasbag plasma conditions and cannot account for the discrepancy observed in Figure 7.

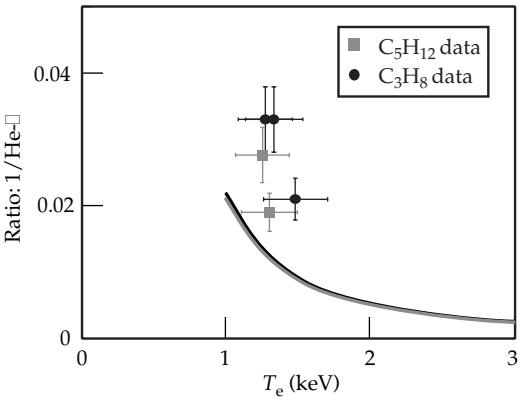

FIGURE 7. Comparison between the experimental line ratios from gasbags with steady-state kinetics (collisional-radiative) model calculations. The intensity ratio between the He-β transition (resonance plus intercombination line) to satellite feature 1, whose upper state is populated by inner-shell collisional excitation, shows discrepancies of up to a factor of two compared with the fully kinetics modeling. (NIF-0401-02075pb01)

The most likely explanation for the observed discrepancies arises from differences in the ion balance between model and experiment. The calculations indicate that at the time of the measurements about 80% of the argon ions are in the He-like ionization state while only 1%-2% of the ions remain in the Li-like state. Small errors in the calculation of the absolute number of Li-like ions can therefore result in large errors in the ratio of collisional excited satellites (e.g. feature 1) to the resonance transition (the He-β transition).

Conclusions

We have performed x-ray spectroscopic experiments in homogeneous gasbag plasmas where we independently measure the temperature with Thomson scattering. We find that collisional radiative (kinetics) modeling of the intensities of the He-β line and its dielectronic capture satellites is generally in agreement with the measured spectra. On the other hand, for the particular case of satellites arising from inner-shell electron collisional excitation, we find discrepancies of up to a factor of two between experiment and kinetics models. We have ruled out possible effects on the line emission due to plasma gradients, radiative transport, and suprathermal electron excitation, leaving errors in the atomic physics modeling to be the most likely explanation.

The determination that there are problems with the collisionally populated states is important for the interpretation of inertial confinement fusion capsule implosions where electron densities and temperature have been measured using

the spectral line shape of the He-β transition of Ar XVII. The analysis of the implosion data has required Stark broadening calculations coupled to a kinetics model to calculate the detailed line intensities and widths. Despite remaining discrepancies, the good agreement between the experimental dielectronic capture satellites and the HULLAC calculations suggests that HULLAC is a more appropriate code for the construction of the kinetics models of the He-β complex from high-density plasmas than previously used codes (e.g., MCDF). HULLAC results in somewhat higher temperatures for the implosion conditions of Refs. 5 and 6 that are in closer agreement with the 2D radiation hydrodynamic modeling and other spectroscopic techniques. These results indicate that benchmarking kinetics codes with Thomson scattering is an important area in present ICF research.

Acknowledgments

We would like to thank A. L. Osterheld, C. Decker, L. Lours, and P. E. Young for helpful discussions.

Notes and References

1. B. J. MacGowan et al., *Phys. Plasmas* **3**, 2029, (1996).
2. S. H. Glenzer et al., *Phys. Rev. E* **55**, 927 (1997).
3. P. G. Burkhalter et al., *J. Appl. Phys*. **50**, 4532 (1979).
4. V. A. Boiko et al., *Mont. Not. R. Astr. Soc.* **185**, 789 (1978).
5. B. A. Hammel et al., *Rev. Sci. Instrum.* **61**, 2774 (1990). B. A. Hammel et al., *Phys. Rev. Lett.* **70**, 1263 (1993). B. A. Hammel et al., *J. Quant. Spectrosc. Radiat. Transfer* **51**, 113 (1994).
6. N. C. Woolsey et al., *Phys. Rev. E* **56**, 2314 (1997). Ibid., *Phys. Rev. E* **57**, 4650 (1998). N. C. Woolsey et al., *Phys. Rev. E* **53**, 3696 (1996). Ibid., *J. Quant. Spectrosc. Radiat. Transfer* **58**, 975 (1997).
7. M. D. Cable et al., *Phys. Rev. Lett.* **73**, 2316 (1994).
8. A. H. Gabriel, *Mon. Not. R. Astron. Soc.* **160**, 99 (1972).
9. R. W. Lee, B. L. Whitten, and R. E. Strout, II, *J. Quant. Spectrosc. Radiat. Transfer* **32**, 91 (1984).
10. C. F. Hooper, Jr., et al., *Phys. Rev. Lett.* **63**, 1267 (1989). C. F. Hooper et al., *Quant. Spectrosc. Radiat. Transfer* **44**, 79 (1990).
11. R. C. Mancini et al., *Rev. Sci. Instrum.* **63**, 5119 (1992). D. A. Haynes et al., *Phys. Rev. E* **53**, 1042 (1996). I. E. Golovkin and R. C. Mancini, *J. Quant. Spectrosc. Radiat. Transfer* **65**, 273 (2000).
12. H.-J. Kunze, in *Plasma Diagnostics*, edited by W. Lochte-Holtgreven (North-Holland, Amsterdam, 1968), p. 550.
13. S. H. Glenzer et al., *Phys. Plasmas* **6**, 2117 (1999). S. H. Glenzer et al., *Rev. Sci. Intrum.* **70** 1089 (1999). S. H. Glenzer et al., *Phys. Rev. Lett.* **82** 97 (1999).
14. G. Zimmerman and W. Kruer, *Comments Plasma Phys. Controlled Fusion* **2**, 85 (1975).
15. A. Bar-Shalom and M. Klapisch, *Computer Phys. Comm.* **50**, 375 (1988). M. Klapisch, *Computer Phys. Comm.* **2**, 239 (1971). M. Klapisch et al., *J. Opt. Soc. Am.* **67**, 148 (1977). J. Oreg et al., *Phys. Rev. A* **44**, 1750 (1991). A. Bar-Shalom et al., *Phys. Rev. A* **38**, 1773 (1988).
16. E. M. Campbell et al., *Rev. Sci. Intrum.* **57**, 2101 (1986).
17. C. A. Back et al., *Rev. Sci. Instrum.* **66**, 764 (1995).
18. J. D. Kilkenny, *Laser Part. Beams* **9**, 49 (1991).
19. J. A. Fejer, *Can. J. Phys.* **39**, 716 (1961). D. E. Evans, *Plasma Phys.* **12**, 573 (1970). S. H. Glenzer et al., *Phys. Rev. Lett.* **77**, 1496 (1996).
20. P. Beiersdorfer et al., *Phys. Rev. E* **52**, 1980 (1995).
21. F. B. Rosmej, *J. Phys. B* **28**, L747 (1995). F. B. Rosmej, *J. Quant. Spectrosc. Radiat. Transfer* **51**, 319 (1994).

Demonstration of Time-Dependent Symmetry Control in Hohlraums by Drive-Beam Staggering

R. E. Turner *P. Amendt* *O. L. Landen* *S. G. Glendinning* *P. Bell*

C. Decker *B. A. Hammel* *D. Kalantar* *D. Lee* *R. Wallace*

*D. Bradley** *M. Cable* *R. S. Craxton** *R. Kremens** *W. Seka**

*J. Schnittman** *K. Thorp** *T. J. Murphy*† *N. Delamater*† *C. W. Barnes*†

A. Hauer† *G. Magelssen*† *J. Wallace*†

In indirect-drive inertial confinement fusion (ICF), x-rays are used to deliver energy to the surface of a capsule which contains deuterium-tritium fuel.[1] The capsule surface is ablated by the x-rays, and the resulting pressure implodes the remaining capsule and fuel to the densities and temperatures required for efficient thermonuclear fusion.

The x-rays are produced by directing multiple laser beams onto specific locations on the interior wall of a high-Z cavity (hohlraum) surrounding the capsule, where they are efficiently absorbed, reradiating much of the energy as soft x-rays.[1, 2] These x-rays, in turn, heat the remainder of the hohlraum wall, which then reradiates as well. The centrally located implosion capsule is thus heated by radiation from the laser absorption region ("hot spot") and the less intense radiation from the heated hohlraum wall, while the laser-entrance holes (LEHs) in the hohlraum produce no radiation. Different points on the capsule's surface view different solid angle-weighted proportions of hot spots, wall, and LEH. The objective is to have any point on the capsule's surface absorb the same amount of drive energy, at any given time, as any other point, in order to produce a uniform implosion. Analytic calculations and simulations[1-4] have shown that high spatial frequency drive variations are effectively smoothed by the hohlraum environment. What remains is to smooth the lowest spatial frequency variations, which, for the cylindrical hohlraum geometry considered here, are usually expressed in terms of a Legendre series [$\Sigma A_n P_n(\cos\theta)$, ($n$ = 0, 2, 4, …), where θ is the angle relative to the symmetry axis]. The odd terms vanish due to the basic symmetry of the geometry. It has been shown[2] that for a given wall-to-hot spot temperature ratio, and hohlraum geometry, the lowest (P_2) mode coefficient can be made equal to zero by an appropriate choice of hot spot location.

Unfortunately, these parameters change with time. For example, the power fraction reradiated by the indirectly heated wall ("albedo") rises with time. Also, the hohlraum wall expands inwardly, intercepting the laser beams at new locations and thus causing the hot spots to move closer to the hohlraum axis. It is this latter effect that is of interest to us in this article. An example of this spot motion is shown in Figure 1. The concern is that the resulting large P_2 excursions are predicted to lead to intolerable higher spatial order capsule shell density and velocity perturbations which will impede full convergence and thwart fusion ignition. The obvious solution—to change the pointing of the beams in a time-dependent fashion—can effectively be accomplished by pointing

*Laboratory for Laser Energetics, University of Rochester, Rochester, NY

†Los Alamos National Laboratory, University of California, Los Alamos, NM

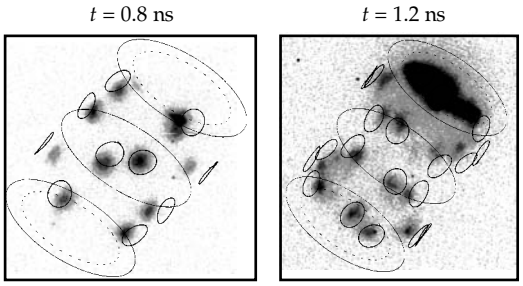

FIGURE 1. Gated x-ray images (hν ~ 5 keV) of laser–plasma interaction regions, with original wall positions superimposed, show movement of x-ray emission region due to wall motion for early beams (left) and later beams (right). Note the strong x-ray emission from the laser entrance hole obscures some spots in the late-time image. (NIF-0401-02055pb01)

different beams to different locations, while tailoring the pulse shape differently on the different beams, so that the average laser pointing moves in time, as required, to counteract the wall motion and maintain drive symmetry. This technique is referred to as beam phasing.[1]

Experiment

In the experiments reported here we have used a simpler variation, referred to as beam staggering. Different pointings are used for different sets of beams, and there is a timing offset between the two groups of beams. However, there is no individual laser pulse shape control for the different groups of beams. This technique provides a single, midcourse correction for the time-dependent drive symmetry.

To demonstrate the effect, we have made time-resolved drive symmetry measurements for two different sets of laser pointings. Both are calculated to give time-integrated symmetry for implosion times of order 2 ns. One set of pointings ("reduced swing") is designed to give good drive symmetry (low P_2) at all times, while the second ("enhanced swing") is calculated to give significant P_2 symmetry swings in time. The results are in good agreement with calculations.

The experiments were conducted on the University of Rochester's OMEGA laser system,[5,6] using 30 of the possible 60 beams to drive a cylindrical gold hohlraum[7] 1.6 mm in diameter, 2.1 mm in length, with 1.2-mm-diameter laser entrance holes at either end. The geometry, shown in Figure 2, is such that five laser beams at each end are incident at 42 degrees to the hohlraum axis, and are designated as "cone 2." The remaining ten beams at each end are incident at 58.8 degrees and are designated as "cone 3." The cone 3 beams are further subdivided into two, interleaved in azimuth, referred to as cones 3a and 3b. All beams had similar power profiles: 480 J per beam at 351 nm, in a 1.1-ns-long, constant power pulse. The cone 3a beams were on from time zero to t = 1.1 ns; the cone 3b and cone 2 beams were on from t = 1 to t = 2.1 ns. The resulting total laser power is a 2.1-ns-long stepped pulse, with a 1:2 contrast ratio, as shown by the dashed line in Figure 3.

One measure of symmetry is the shape of the fuel region in imploded capsules[8,9] obtained by direct pinhole imaging of the x-ray emission (3- to 6-keV photons) onto a gated microchannel plate (MCP) camera.[10] The emission is enhanced by doping the 50 atmospheres of deuterium fuel in the 440-µm-inner-diameter capsule with 0.8 atmospheres of argon. (In the thinnest walled capsules, deuterium fill pressure was limited to 10 atmospheres due to material strength concerns.) The convergence ratio of the targets is limited by design to ⊕8, leading to an ⊕55-µm-diameter imploded core, easily resolved by a 12-µm resolution pinhole camera. The observed asymmetry of the core is the result of the drive asymmetry integrated over the duration of the implosion. For these experiments this integration time was varied by changing the capsule wall thickness from 10 µm to 55 µm. The

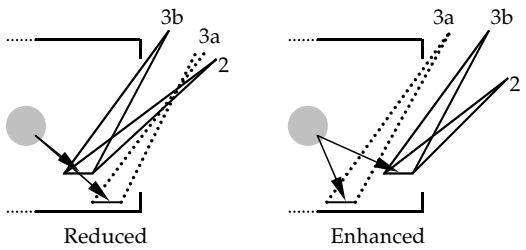

FIGURE 2. Schematic of OMEGA hohlraum geometry, showing laser pointing for the three cones in the two configurations. Cone 3a is the "early" cone. (Only right half is shown.) (NIF-0401-02056pb01)

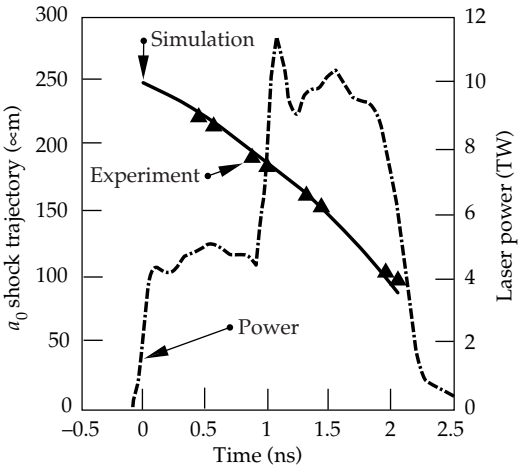

FIGURE 3. Total laser power (dashed), and measured and simulated average ablation front trajectory, versus time. Data is from enhanced swing configuration; reduced swing configuration gives identical results. (NIF-0401-02057pb01)

size (FWHM) of the implosion core's vertical (a) and horizontal (b) axes was recorded, and the ellipticity ratio (a/b) was used as a measure of the lowest order P_2 asymmetry averaged over the implosion time. Knowledge of the time-dependent asymmetry can be inferred by examining the results of targets with varying implosion times, as shown in Figure 4.

The second technique uses an x-ray backlit surrogate foam (0.3 g/cm^3 SiO_2 aerogel) ball, which yields a continuous record of hohlraum asymmetry.[11,12] As the x-ray drive ablates the foam ball's surface, the ablation pressure drives a shock front into the ball. Simulations show that the asymmetry of the ball, as measured by the x-ray transmission inflection points in a backlit image, is a good measure of the drive asymmetry imposed up to that time. The asymmetry of the ball at differing times is obtained from analysis of backlit images recorded with the time-resolved pinhole camera described previously. Examples of these images are shown in Figure 5. The x-ray backlighting source is a titanium foil which, in a novel arrangement, is mounted directly over a hole in the side of the hohlraum wall. The foil is illuminated for 2 ns with eight staggered laser beams on its rear surface. The Ti is 5 μm thick, which allows the 4.7-keV He-like line radiation generated on the outside to pass through the foil and backlight the foam ball. At the same time, the inner side of the Ti absorbs and reemits, with reasonable efficiency, the softer drive radiation, reducing the asymmetry an open hole would produce. The diagnostic observation hole, opposite the Ti foil, is covered with a very thin (0.2-μm) layer of Ta, to help reduce the drive perturbation due to that hole.

The two diagnostic techniques are complementary in time. The foam ball works well for the first 2 ns, but after that the shock has reached the center. The capsules of varying wall thickness ("symmetry capsules") work well for the time-integrated measurements ending between 1.4 to 2.7 ns; it is not possible to make capsule shells thin enough to integrate over an earlier time frame.

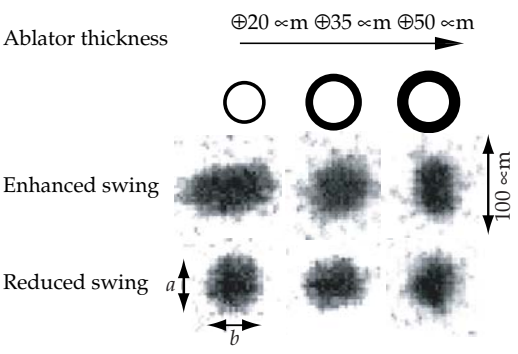

FIGURE 4. Schematic of symmetry capsule principle. Thicker capsules integrate over longer times; ratio of vertical to horizontal size of imploded image (a/b) is used as a measure of symmetry. (NIF-0401-02058pb01)

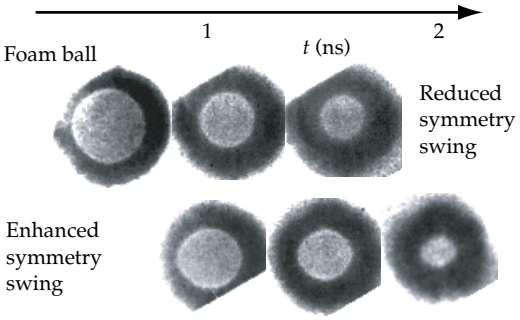

FIGURE 5. Examples of time-resolved x-ray backlit images of foam ball targets. Enhanced swing case shows observable P_2 (note horizontal size > vertical) at early times, and observable P_4 asymmetry at 2 ns (note diamond shape). (NIF-0401-02059pb01)

In all shots, the beams were pointed to positions which produce a nearly round implosion for capsules designed to implode in approximately 2 ns. For the experiment attempting to minimize P_2 symmetry swings, the cone 3a beams are turned on first, and are aimed at the location which minimizes P_2 during the first nanosecond. During that time, the gold wall expands inward, and the hot spot, as seen from the capsule, moves back toward the laser-entrance holes. At the end of the first nanosecond, the cone 3a beams are turned off, and the remainder of the beams are turned on. These are aimed at a new location—more inward, or toward the capsule—to account for the fact that the gold wall has moved, and will continue to move, inward some 150 μm. As seen from the capsule, the hot spot from these later beams begins in approximately the same angular position as the initial cone 3a hot spot location. This is shown schematically in Figure 2. This midcourse repointing acts to restore the drive symmetry which would have otherwise been lost due to wall motion, had all the beams been pointed similarly. The actual pointings, defined as the point of intersection of the laser beam with the hohlraum symmetry axis, measured from the hohlraum center, are shown in Table 1.

For the experiment designed to enhance the time-dependent symmetry swing, the beams were repointed to positions which would give poor symmetry over any given half of the pulse while still maintaining time-integrated symmetry over the whole pulse. This was accomplished by pointing the early cone 3a beams further inward. The later cones 2 and 3b beams were then pointed more outward, to compensate in a time-averaged sense (see Figure 2). Beam timing and pulse shape were not changed between experiments.

TABLE 1. Laser beam pointing configurations for the two cases studied. Numbers shown are the distances from the center of the hohlraum to the points where the beams cross the axis of symmetry.

Experiment	Cone 2 (μm)	Cone 3a (μm)	Cone 3b (μm)
Reduced swing	1175	1100	900
Enhanced	1450	950	1150

Simulations and Analysis

The above-described experimental conditions are simulated with a two-dimensional radiation-hydrodynamics code.[13] Integrated modeling techniques, which treat the hohlraum, capsule or surrogate target, laser deposition, and x-ray conversion as a coupled physical system, are used.[14] Following completion of the simulations, postprocessing is used to generate synthetic images of the capsule or surrogate target for direct comparison with experiment.

For the low-convergence implosions, the ellipticity ratio (a/b) of the synthetic image's 50%-of-peak-emission contour is extracted, in the same manner as is done for the data, as shown in Figure 4.

For the foam ball simulations, the inflection point contour for transmissivity through the target is extracted and written as a partial sum of Legendre polynomials with coefficients a_n (n = 0, 2, 4).[12,15] For each Legendre coefficient, a fit through the simulated data is performed and then differentiated in order to extract information about the ablation pressure history. For a constant or increasing pressure, the shock speed in a material is proportional to the square root of the pressure. Expanding this relationship in a Legendre series and keeping only the lowest order terms, the various Legendre coefficients of ablation pressure P_{An} are related to the shock front trajectory as follows[15]:

$$P_{A0} = \left[2\rho / (\gamma + 1)\right] \dot{a}_0^2 \quad (1a)$$

$$P_{A2} / P_{A0} = 2\,\dot{a}_2 / \dot{a}_0 \quad (1b)$$

$$P_{A4} / P_{A0} = 2\,\dot{a}_4 / \dot{a}_0 \quad (1c)$$

where ρ is the foam ball density, γ is the ratio of specific heats, and overdots denote

differentiation with respect to time. However, we do not measure the shock front trajectory but rather the x-ray transmissivity inflection point trajectory. Simulation studies indicate that this latter quantity provides a representative measure of the location of the shock.[15] Although not strictly correct, the association of shock front and inflection point provides a simple relation for estimating ablation pressure asymmetry without invoking detailed radiation-hydrodynamic simulations. In fact, comparison of this estimate of instantaneous ablation pressure asymmetry with such simulations shows fairly good agreement for the second order coefficient, as shown in Figure 6. It is in this spirit that shock front and inflection point are used interchangeably.

The measured average ablation front trajectory $a_0(t)$ provides a direct means of diagnosing the x-ray drive.[16] Figure 3 shows the measured and simulated trajectories, and the laser power history, for the enhanced swing case. We note an increase in velocity after 1 ns, indicating the nearly instantaneous onset of increased x-ray drive. A direct measurement of the emitted x-rays[17] is shown in Figure 7. It shows the drive rising from an effective blackbody temperature of 130 eV during the foot to 190 eV by the end of the pulse, in good agreement with the $a_0(t)$ data and simulation shown in Figure 3. The error in measuring a_0 is small, and does not significantly contribute to the error in deducing P_{A2} from equation (1b).

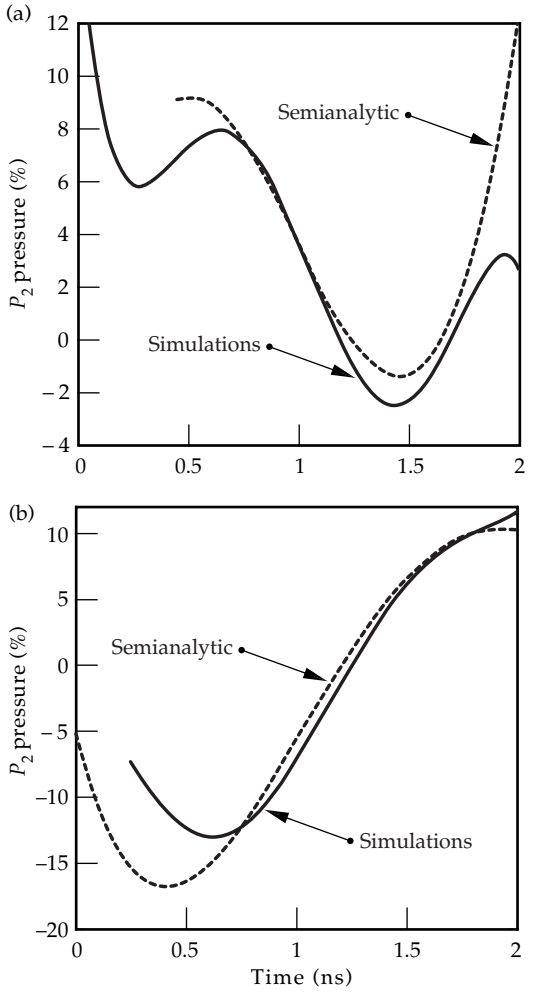

FIGURE 6. Comparison between hydrodynamic code simulations and simple analytic expression for 2nd order coefficient; (a) reduced swing case, (b) enhanced swing case (note expanded vertical scale). (NIF-0401-02060pb01)

Results

Figure 4 shows examples, and Figure 8 shows the quantitative results, of the symmetry capsule experiments and simulations, plotting the (a/b) eccentricity of the imploded cores as defined earlier versus the observed x-ray emission time. The simulations are overplotted on Figure 8. Each data point is the average of two shots. Note that the (a/b) distortions for the two pointing schemes cross each

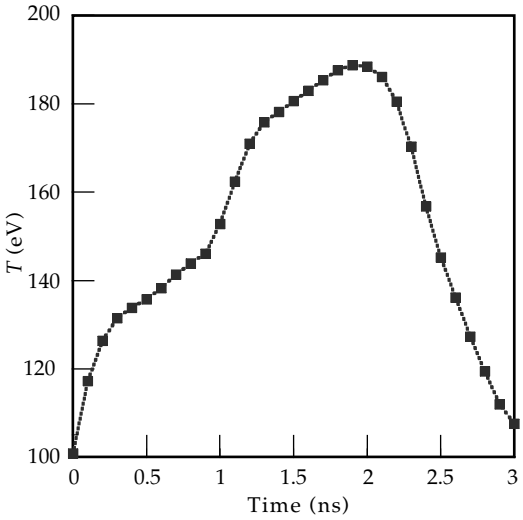

FIGURE 7. Measured x-ray drive flux as a function of time, expressed as an effective Planckian temperature. (NIF-0401-02061pb01)

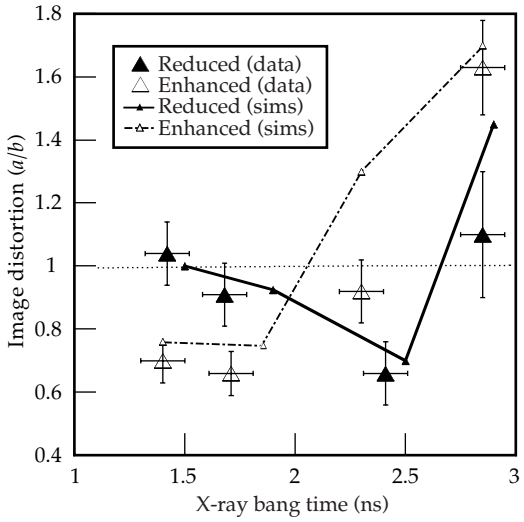

FIGURE 8. Measured and simulated *a/b* elliptical distortion of imploded capsule core versus peak x-ray emission time, for the different pointings. (NIF-0401-02062pb01)

other at ⊕2 ns, as designed. However, the capsules driven with reduced-swing beam pointing show good implosion symmetry for shorter implosion times, while the enhanced P_2 swing pointing case does not. The experiment attempting to reduce the symmetry swing shows (a/b) decreasing between 1.5 and 2 ns, a clear qualitative indication that the normal symmetry swing due to spot motion, which would increase (a/b), has been reversed. It should be noted that the thickest capsules shown imploded long (>0.8 ns) after all laser beams were off. For these capsules, symmetry control is not maintained after 2 ns for either pointing.

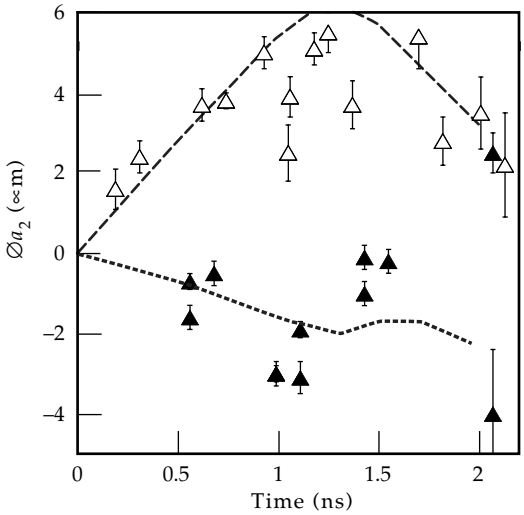

FIGURE 9. Time variation of second Legendre coefficient of ablation front trajectory, with inferred $t = 0$ offsets subtracted (see text). Solid (short-dashed line) and open (long-dashed line) symbols show data (simulations) from the reduced swing and enhanced swing pointings, respectively. (NIF-0401-02063pb01)

Figures 3, 9, and 10 show the reduced data from the foam balls; a_0 (Figure 3), a_2 (Figure 9), and a_4 (Figure 10) are the zeroth, second, and fourth order Legendre polynomial coefficients, respectively, of the fit to the inflection point contours of the backlit images. The simulation results are overplotted on these figures. The time-dependence of the zeroth order coefficient (corresponding to an average radius) yields information on the average x-ray power, as previously discussed. The second order coefficient a_2 quantifying ellipticity, yields continuous information on the time-integral of the P_2 flux asymmetry experienced near the center of the hohlraum.[15] For the data presented here, the values of $a_2(t)$ are small enough that any initial $a_2(0)$ distortion present in the foam ball can cause a substantial offset in the results. We have removed this offset from the data, to clarify the important result, the demonstrated control of time-dependent variations in a_2. The offsets are too small (0, 0.5, 0.5, and 2.5 μm) to have been noticed during initial target characterization; we have inferred them from the values required to make the changes in a_2 extrapolate to zero, at time zero, for each shot. In any case, the instantaneous flux asymmetry is derived from the slope of the $a_2(t)$ history and not its absolute value. The error bars shown are statistical only, from the curve fitting process for each image.[11,12]

The results show a large excursion in a_2 for the case where the symmetry swing was intentionally enhanced, reaching a peak of ⊕5 μm, or 3% of the average radius at that time. For the case attempting to reduce the symmetry swing, the a_2 variation is significantly reduced in magnitude, and shows the expected shift following the change in beam pointing at $t = 1$ ns. The following simple argument[18] shows that applying a single midterm pointing correction should significantly reduce (by ⊕4×) the maximum a_2. Consider the P_2 swing approximated as linear in time.[2] Then a_2 is $\alpha \int P_2 dt$, hence αt^2. Therefore, halving the time over which the P_2 swing is left uncorrected reduces the a_2 by 4×. Generalizing, applying n corrections by staggering beams n times would reduce a_2 by n^2.

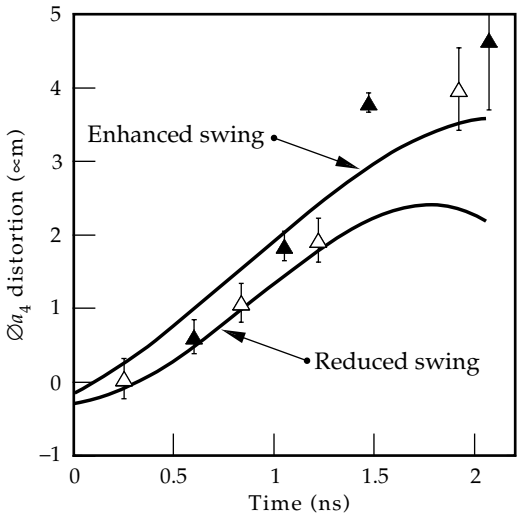

FIGURE 10. Time variation of fourth Legendre coefficient of ablation front trajectory. Each data point (symbols) has been averaged over several shots and corrected for initial offset. Solid and open symbols show data from the reduced swing and enhanced swing pointings, respectively. Solid lines show simulations. (NIF-0401-02064pb01)

The fourth order coefficients shown in Figure 10 have been adjusted for an initial offset (up to 1.5 μm) in the same manner as described above for the second order data. The simulations are overplotted. As the results indicate, this experiment did not attempt to control the fourth order coefficients; that will be the subject of future work.

Conclusions

The simulations of $a_2(t)$ for the two different pointings are, as shown in Figure 9, in good agreement with the measurements. The inferred ablation pressure asymmetries $P_{A2}(t)$, obtained by differentiating the simulations as described above, are shown in Figure 6. The ratio of the P_2/P_0 pressure coefficients vary from –0.13 to +0.12 for the enhanced swing case, while the maximum extremes for the reduced swing case are –.025 and +.08, a factor of two and one-half reduction in total symmetry swing. The magnitude of the P_{A2} symmetry swing for the reduced swing case is less than 10% over a 2-ns duration, which is the required level of control calculated for ignition targets on the National Ignition Facility.[1,2]

In summary, we have shown how lowest order hohlraum drive asymmetries due to plasma wall motion and changing wall-to-hot spot temperature ratios can be controlled in a time-dependent fashion, using a multicone beam geometry.

Acknowledgments

We wish to thank the OMEGA operations staff, led by S. Loucks, S. Morse, and G. Pien, for their work in support of this experiment.

Notes and References

1. J. Lindl, *Phys. Plasmas* **29**, 3933 (1995).
2. L. J. Suter et al., *Phys. Rev. Lett*. **73**, 2328 (1994).
3. S. Haan, *Radiation Transport between Concentric Spheres*, Lawrence Livermore National Laboratory, Livermore, CA, UCRL-ID-118152 (1994); reprints available to the public from the National Technical Information Service, U.S. Department of Commerce, 5285 Port Royal Rd., Springfield, VA 22161.
4. A. Caruso and C. Strangio, *Jpn. J. Appl. Phys*. **30**, 1095 (1991); J. A. Fleck, Jr., and J. D. Cummings, *J. Comput. Phys*. **8**, 313 (1971).
5. T. R. Boehly et al., *Opt. Commun*. **133**, 495 (1997).
6. J. M. Soures et al., *Phys. Plasmas* **3**, 2108 (1996).
7. T. J. Murphy et al., *Phys. Rev. Lett*. **81**, 108 (1998).
8. A. Hauer et al., *Rev. Sci. Instrum*. **66**, 672 (1995).
9. A. Hauer et al., *Phys. Plasmas* **2**, 2488 (1995).
10. J. D. Kilkenny et al., *Rev. Sci. Instrum*. **59**, 1793 (1988).
11. P. Amendt et al., *Rev. Sci. Instrum*. **66**, 785 (1995).
12. S. G. Glendinning et al., *Rev. Sci. Instrum*. **70**, 536 (1999).
13. G. B. Zimmerman and W. L. Kruer, *Comments Plasma Phys. Control. Fusion* **2**, 51 (1975).
14. J. D. Kilkenny, *Laser Part. Beams* **9**, 49 (1991).
15. P. Amendt et al., *Phys. Plasmas* **4**, 1862 (1997).
16. P. Amendt et al., *Phys. Rev. Lett*. **77**, 3815 (1996).
17. C. Decker et al., *Phys. Rev. Lett* **79**, 1491 (1997).
18. O. L. Landen et al., *Phys. Plasmas* **6**, 2137(1999).

Intense High-Energy Proton Beams from Petawatt Laser Irradiation of Solids

R. A. Snavely[a,b] *M. H. Key*[a] *S. P. Hatchett*[a] *T. E. Cowan*[a]

M. Roth[c] *T. W. Phillips*[a] *M. A. Stoyer*[a] *E. A. Henry*[a]

T. C. Sangster[a] *M. S. Singh*[a] *S. C. Wilks*[a] *A. MacKinnon*[a]

A. Offenberger[d] *D. M. Pennington*[a] *K. Yasuike*[e] *A. B. Langdon*[a]

B. F. Lasinski[a] *J. Johnson*[f] *M. D. Perry*[a] *E. M. Campbell*[a]

We report an experiment which demonstrated for the first time that exceptionally intense and well-collimated proton beams are produced when thin-foil targets are irradiated at ultrahigh intensity with ultrashort laser pulses.[1]

The generation of fast protons from laser-irradiated solid surfaces is well understood[2,3] and attributable to electrostatic fields produced by hot electrons acting on protons from adsorbed hydrocarbons.[3] An empirical power law relationship between the mean proton energy and intensity × (wavelength)^2 ($I\lambda^2$) was identified, and proton energies up to a few MeV were observed for $I\lambda^2$ up to 10^{18} W cm^{-2} μm^2 in nanosecond pulses.[2] Chirped pulse amplification (CPA) laser technology[4] enabled widespread generation of terawatt (TW) power and the first petawatt (PW) laser.[5] CPA lasers generate pulses in the range 20 fs to 1 ps. Protons with 10-MeV energy were observed with a 1-ps CPA laser at $I\lambda^2 = 10^{19}$ W cm^2 μm^2, consistent with the previous scaling.[6]

New mechanisms of ion acceleration have been studied with CPA lasers. Ponderomotive pressure of the laser radiation causes radial acceleration when laser beams are focused in gas jets and in subcritical density plasmas[7] and also causes axial acceleration into solid targets.[8] Coulomb explosion of molecules[9] and clusters[10] has produced energetic ions. The ion energies from these newly studied processes have been <1 MeV/nucleon.

We report a laser-induced proton beam with much higher particle energy and better collimation than previously observed with the distinctive feature that it is emitted perpendicular to the rear unirradiated surface(s) of the target. The high proton energy, up to 58 MeV, opens up access to nuclear processes.

The experiments used a CPA laser system generating 1-PW pulses of 500-fs duration.[5] With $f/3$ parabolic mirror focusing, the peak intensity was 3×10^{20} W cm^{-2} in a focal spot of 9-μm full width at half maximum (FWHM), with 30% of the energy inside the first minimum. Amplified spontaneous emission in a 4-ns period before the main pulse had 10^{-4} of the main pulse energy, and there was a 3×10^{-4} prepulse 2 ns before the main pulse. This precursor radiation generated a plasma that was measured by subpicosecond optical interferometry. The on-axis electron density was 3×10^{19} cm^{-3} in a plane 70 μm from a

[a]University of California, Lawrence Livermore National Laboratory, PO Box 808, Livermore, CA 94550

[b]University of California, Davis, Department of Physics, Davis, CA 94616

[c]Visiting from GSI Laboratory, Darmstadt, Germany

[d]Visiting from University of Alberta, Edmonton, Alberta, T6G 2G7, Canada

[e]Visiting from ILE, Osaka University, Suita, Osaka 565, Japan

[f]University of Texas, Huntsville, Texas

flat CH target with an approximately exponential fall to lower densities having a scale length of 40 μm.[11]

The proton beam was recorded with radiochromic (RC) film, which changes through polymerization of a diacetylene active layer from transparent to dark blue (dark to white in Figures 1 and 4) in proportion to the dose (rads) of ionizing radiation (1 rad = 100 ergs/g). A 90° conical assembly of alternating Ta foils and sheets of RC film was used. The cone is 4 cm deep at its apex, which was placed 4.2 cm behind the target on the laser axis so the detector covered the forward hemisphere. The RC film response was calibrated absolutely, and the image data were analyzed by digital densitometry and transformed geometrically to produce contour plots of dose as a function of angle illustrated in Figure 1.

The data in Figure 1 show a collimated intense proton beam emitted perpendicular to the rear target surface of a target at 45° to the laser axis. Its angular width narrows to 10° in the image through 600 μm of Ta. The beam is rather uniform in intensity with near-circular, sharp boundaries. There is a low-intensity wide-angle background, discussed elsewhere, that is due to escaping relativistic electrons.[12] Similar results are seen for normal incidence, S polarization, and target thickness down to 20 μm. The beam profiles from CH targets have nonuniform edges and exhibit internal fine structure as illustrated in Figure 2 for a 100-μm-thick CH target at normal incidence. There was typically a 5 times greater dose recorded from CH relative to Au targets. The proton identity of the beam was first suggested by analysis of etched tracks in CR39 plastic behind 7 mm of Al, which gave evidence of >30-MeV protons.

The response of each RC film layer as a function of proton energy was calculated from stopping powers obtained with the SRIM code.[13] (An example for a similar detector package is shown in Figure 2.) The integrated rad cm^2 in each image of the proton beam was determined from the RC film data. A deconvolution procedure was then used to relate these data to the film response (in rad cm^2 per proton) to give the absolute proton energy spectrum. Figure 3a shows an example in which the energy spectrum has a cutoff at about 58 MeV, with a near-exponential slope temperature of 4 MeV. The conversion fraction of laser energy to protons $E > 10$ MeV is 12% at 48 J. The extrapolation of the energy spectrum below 10 MeV is uncertain because the detector did not record protons of lower energy.

The sharp cutoff of the energy spectrum was also measured at 45° to the laser axis via a hole in the RC film detector using a magnetic spectrometer. These energy spectra were obtained from densitometry of photographic film as illustrated in Figure 3b. For targets irradiated at 45° incidence, the recorded spectrum was on

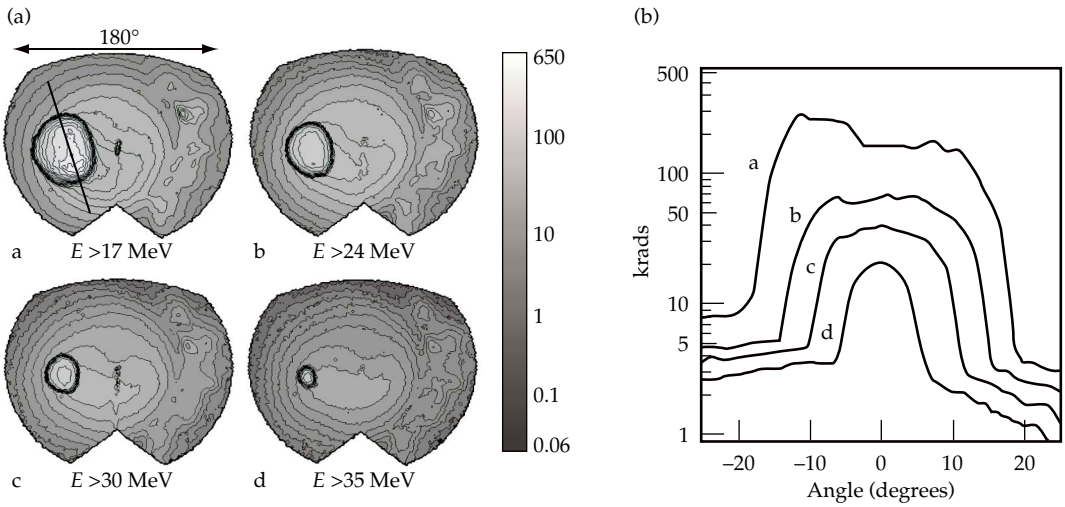

FIGURE 1. (a) Contour plots (a to d) of dose in kilorads (color bar units) as a function of angle after penetration through respectively 0.2-, 0.4-, 0.6-, and 0.8-mm Ta in the detector. The target was a 1-mm-square, 125-μm-thick Au foil irradiated with 465 J at 45° P polarized incidence. (b) Plot of beam profile lineouts showing kilorads as a function of angle in the vertical direction through the center of the proton beam along path as indicated in (a). (NIF-0401-02065pb01)

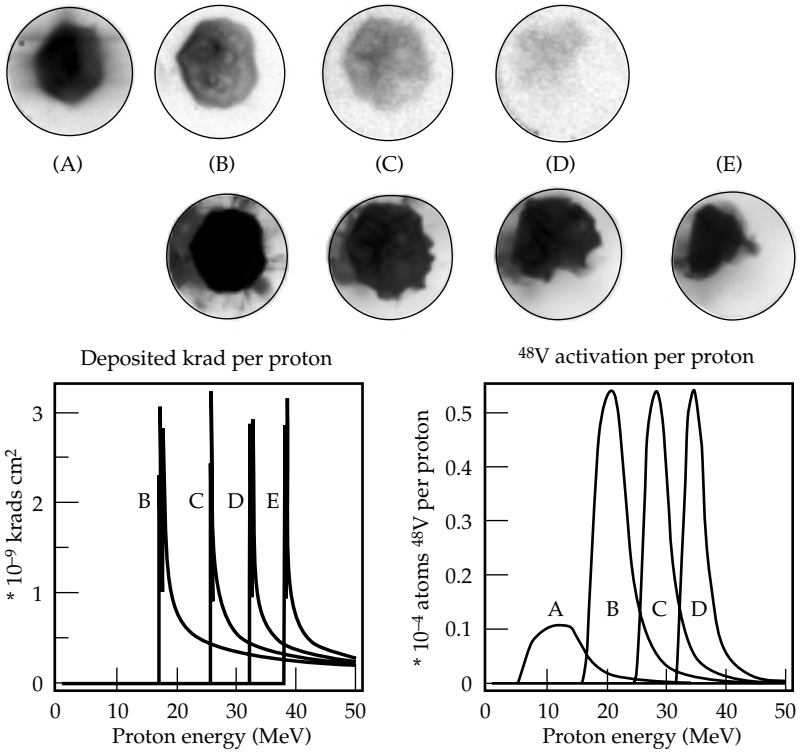

FIGURE 2. Data for a normal incidence, 445-J shot on 100-µm CH from the Ti nuclear activation and RC film detector described later in the text: Ti foil autoradiographs (top row) and RC film images (middle row). The plots show Monte Carlo modeling (bottom left) of the RC film detector response in kilorad cm^2 per proton, normally incident in the film layers, and the nuclear activation response (bottom right) of the Ti layers to protons through the successive filter layers of the detector.
(NIF-0401-02066pb01)

the axis of the proton beam, and in the example shown, there is a cutoff at 55 MeV. For normal incidence, the recorded spectrum was at 45° off axis, and the example shown has a cutoff at 15 MeV, consistent with the reduced cone angle for higher proton energies seen in Figure 1. The photographic film is saturated so only the cutoffs in energy are significant in the plots. An estimate of the apparent source size of the proton emission (400 µm) was obtained from penumbral shadowing at the edge of the high-energy end of the spectrum when a rectangular slit aperture was used, and a 4-mm-square, 125-µm-thick Au foil was irradiated.[14]

Direct evidence that the beam is made up of protons rather than other ion species was obtained from observation of nuclear reactions induced by protons. A multilayer detector was used consisting of 3-cm-diameter flat discs of 50-µm Ti, followed by three repeats of 1.2-mm Be, 250-µm Ti, and 250-µm RC film, then

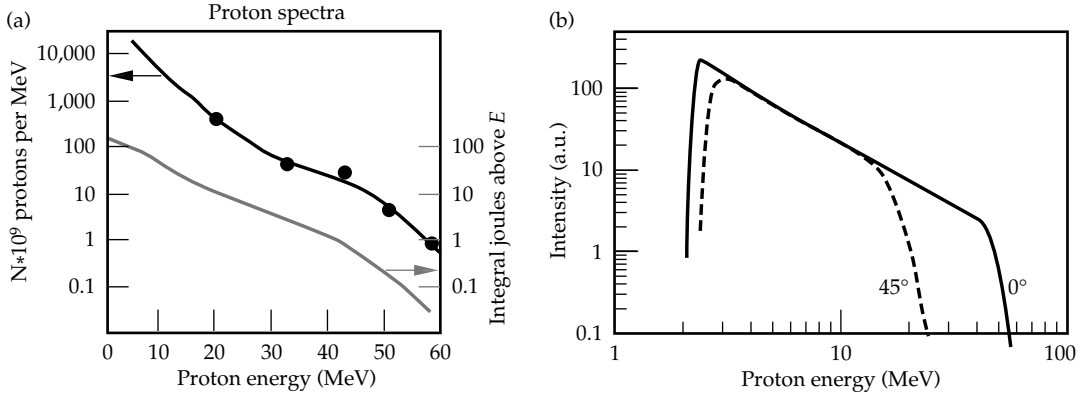

FIGURE 3. (a) Proton energy spectrum deduced from radiochromic film images for a 423-J shot at normal incidence on 100-µm CH. (b) Spectrum of proton energy recorded on film with a magnetic deflection spectrometer. Plots show the spectrum on axis and from another shot at 45°. The detector is saturated above the cutoff region.
(NIF-0401-02067pb01)

1.5-mm Be and 250-µm RC film, placed 4.5 cm behind the target. The yield of the nuclear process, ^{48}Ti(p,n)^{48}V was measured absolutely from the characteristic gamma emission of the activated ^{48}V nuclei. The cross section has a threshold at 5 MeV and peaks at 13 MeV, 500 mbarn.[15] The number of activated nuclei in each Ti layer was determined from the gamma emission. The activation was modeled using the stopping powers[13] and cross sections[15] to give the response of the detector in activations per proton in each Ti layer, as in Figure 2. A deconvolution procedure similar to that used for the RC film gave the absolute energy spectrum of the protons, and close agreement was obtained comparing both methods.

In the example shown in Figure 2 (445 J at normal incidence on 100-µm CH), there was an integrated energy of 30 J (3.5×10^{13} protons or 7% of the laser energy), and the Boltzmann temperature was 6 MeV. Autoradiographic images of the ^{48}V activation in the Ti foils shown in Figure 2 show a one-to-one correspondence to the RC film images recorded on the same shot from adjacent layers in the detector, giving further evidence that the RC film shows a proton beam. Another nuclear process observed was the production of 3×10^{10} neutrons on this shot (data from an Ag activation detector). This efficient yield (7×10^7 neutrons per joule) was from the several neutron-producing channels of proton interaction with Be nuclei[16] and was an order of magnitude greater than neutron yields observed on shots without the Be discs.

Whether the beam was normal to the front or the rear surface of the target was assessed using a 2-mm-wide, 30° wedge target of CH, as illustrated in Figure 4. That the emission was normal to the rear surface is seen in the two separate proton beams in directions corresponding to the normals to major and minor "rear" surfaces of the wedge.

RC images from 1-mm-square thin foil targets through 25-µm Al (recording protons with energy >4 MeV) showed in addition to the intense beam, a weaker sheet of proton emission in the horizontal plane. We attribute this emission to the vertical edges of the target. This suggests that there is proton emission from an extended area of the rear surface of the target with lower-energy protons emitted further from the center of the emitting surface.

Cones of RC film placed both behind and (with a central hole for the laser beam) in front of a CH target for a target at 45° established that protons above the 12-MeV threshold energy for detection integrated over the forward hemisphere had less than 5% of the energy recorded in the proton beam from the rear surface.

We interpret the process generating the proton beam as electrostatic acceleration following hot electron generation. The focused main pulse generates an intense relativistic electron source. Relativistic self-focusing in the preformed plasma[17]

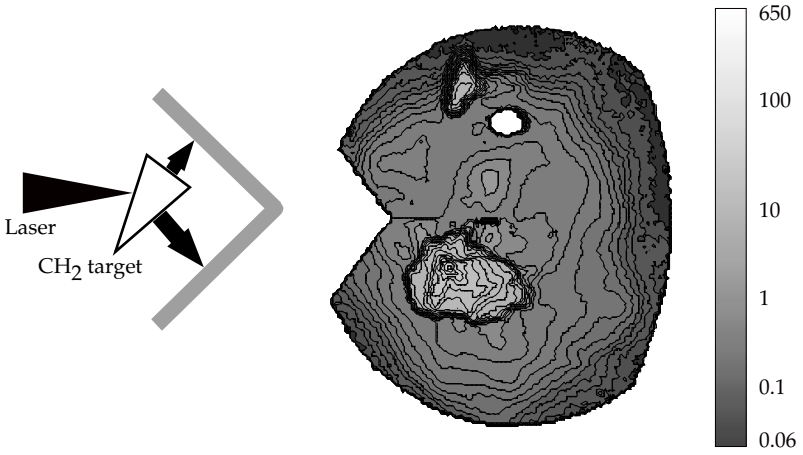

FIGURE 4. Contours of dose in kilorads as a function of angle recorded on an RC film through 300-µm Ta (proton $E >$ 18 MeV). The image clearly shows two proton beams, the larger from the major face and the smaller from the minor face of the wedge. (NIF-0401-02068pb01)

enhances the intensity. This is evidenced in our work by an invariant x-ray emission spot of about 20-μm diameter, as the focal plane was displaced as much as 300 μm in front of the target.[18] We have previously reported on measurements of the energy spectrum of electrons emitted from the rear surface of Au targets.[18] Data show electron energies up to 100 MeV with an exponential slope temperature of 5 to 10 MeV. The RC film data shown in Figure 1 revealed the angular pattern of relativistic electron emission as a diffuse background. The approximate source temperature and energy content of this electron emission were determined by comparison of quantitative analysis of the RC film and Monte Carlo modeling. Typical results were 1 to 2 J of electrons and a Boltzmann temperature of 3 to 4 MeV. The total emitted energy corresponds to the maximum charge that can leave the target before the Coulomb potential traps the major fraction of the electrons. The angular pattern is broad. A similar pattern of >100° cone angle was observed in bremsstrahlung x-rays emitted from thick Au targets. Analysis of the measured total yield of bremsstrahlung at photon energies >0.5 MeV suggests that more than 40% of the laser energy is converted to relativistic electrons.[12,19]

We have adapted the standard model of fast ion generation by hot electrons[3] for very short pulse duration and for the existence at the time of creation of the hot electrons of a preformed long-scale-length plasma on the front of the target and a short-scale-length at the unirradiated back surface.

A full discussion of the acceleration model has been presented elsewhere.[19,20] Briefly described, electrons penetrating through the target ionize H and other atoms at the rear surface. Although the hot electron temperature T_h, the ion scale length L_i, and the Debye scale length L_d rapidly change with time, one can estimate the accelerating field by considering their initial values. By applying Poisson's equation and assuming a Boltzmann distribution for the hot electrons, one obtains the result that the electric field acting on the ions[21] is given by $E = T_h/e \max(L_i, L_d)$. This shows there will be much stronger acceleration at the sharp density interface on the back of the target than on the front, where the preformed plasma scale length is very long as shown by our optical probe data discussed previously. The rate of energy transfer to the ions is therefore initially much greater on the back of the target. Since the initial scale length on the back of the target is roughly a micron, we see that electric fields of MeV/micron are generated. This model, modified by the fact that there are two electron temperatures present,[3,22] is qualitatively consistent with our data. Two-dimensional particle-in-cell simulations have further confirmed these findings and begin to address the relation between cutoff energy and angle in our data (e.g., Figure 1).

We have concluded that processes at the front surface focal spot on the target could not generate the observed ions because of the clear evidence that the protons are emitted perpendicular to the rear surface of the target. The observation of proton emission from the edges of the target supports a model of emission over an extended area much larger than the focal spot. The protons detected from Au targets could not come from the front surface focal region of our targets because of the prepulse-induced blowoff-adsorbed monolayers of hydrocarbon. Moreover, an area that is much larger than the 10^{-6} cm^2 focal spot area is needed to supply the observed number of protons from an adsorbed layer.

Proton beams of the high energy, power, and collimation observed here could be of interest for numerous applications. They may be applicable to medical proton beam cancer therapy or to the production of short-lived radionuclides. More work is needed to characterize the emittance, which will determine the focusability of the beam and its usefulness, for example, in replacing the front end of large accelerators or as an ignitor in fast ignition. The ion acceleration process is not restricted to protons, and with suitable preparation of the target surface, more massive ions could be accelerated to similar energy per nucleon.

Acknowledgment

We are grateful to C. Brown for his skilled operation of the Petawatt Laser System.

Notes and References

1. R. Snavely et al., *Phys. Rev. Lett.* **85**, 2945 (2000).
2. S. J. Gitomer et al., *Phys. Fluids* **29**, 2679 (1986).
3. Y. Kishimoto et al., *Phys. Fluids* **26**, 2308 (1983), and references therein.
4. M. D. Perry and G. Morou, *Science* **264**, 917 (1994).
5. M. Perry et al., *Opt. Lett.* **24**, 160 (1999).
6. A. P. Fews et al., *Phys. Rev. Lett.* **73**, 1801 (1994), and F. N. Beg et al., *Phys. Plasmas* **4**, 447 (1997).
7. G. Pretzler et al., *Phys. Rev. E* **58**, 1165 (1998).
8. M. Zepf et al., *Phys. Plasmas* **3**, 3242, (1996).
9. K. Codling and L. J. Frazinski, *Contemp. Phys.* **35**, 243 (1994).
10. T. Ditmire et al., *Nature* **398**, 489 (1999).
11. A. J. MacKinnon et al., UP2.65, *Bull. Am. Phys. Soc*. **44**, 7 (1999).
12. M. H. Key et al., *Inertial Fusion Sciences and Applications '99*, C. Labaune, W. Hogan, and K. Tanaka, Eds., Publ. Elsevier, p. 392 (1999).
13. J. F. Ziegler et al., *The Stopping and Range of Ions in Solid*s (Pergamon Press, New York, 1996).
14. T. E. Cowan et al., *Nucl. Instr. and Methods in Phys. Res. A* **455**, 130 (2000).
15. H. I. West, Jr., et al., Lawrence Livermore National Laboratory, Livermore CA, UCRL-ID-115738 (1993).
16. J. K. Blair et al., *Nuc. Phys.* **53**, 209 (1964).
17. A. Pukhov and J. Meyer-ter-Vehn, *Phys. Rev. Lett*. **76**, 3975 (1996).
18. M. H. Key et al., *Proc. of 17th IAEA Fusion Energy Conference*, Publ. IAEA Vienna, Vol. 3. p. 1093 (1999).
19. S. Hatchett et al., *Phys. Plasmas* **7**, 2076 (2000).
20. S. Wilks et al., *Phys. Plasmas* **8**, 542 (2001).
21. J. Denavit, *Phys. Fluids* **22**, 1384 (1979).
22. L. M. Wickens et al., *Phys. Rev. Lett*. **41**, 243 (1978).

PUBLICATIONS AND PRESENTATIONS OCTOBER 1999–MARCH 2000

A

Adams, J. J., Bibeau, C., Page, R. H., Krol, D. M., Furu, L. H., and Payne, S. A., *4.0–4.5 m Lasing of Fe:ZnSe below 180 K, a New Mid-Infrared Laser Material*, Lawrence Livermore National Laboratory, CA, UCRL-JC-135419; also in *Opt. Lett.* **24**(23), 1720–1722 (1999).

Amendt, P., Landen, O., Pollaine, S., Suter, L. J., and Hammel, B., *Implosion Target Surrogacy Studies on OMEGA for the National Ignition Facility: Backlit Foamballs and Thinshells*, Lawrence Livermore National Laboratory, Livermore, CA, UCRL-JC-138241-ABS. Prepared for *30th Annual Anomalous Absorption Conf*, Ocean City, MD, May 21–26, 2000.

Amendt, P., Turner, R. E., Bradley, D., Landen, O., Haan, S., Suter, L. J., Wallace, R., Morse, S., Pien, G., Seka, W., and Soures, J. M., *High-Convergence Indirect-Drive Implosions on OMEGA in the Absence of Argon Fuel-Dopant*, Lawrence Livermore National Laboratory, Livermore, CA, UCRL-JC-138240-ABS. Prepared for *30th Annual Anomalous Absorption Conf*, Ocean City, MD, May 21–26, 2000.

B

Back, C. A., Bauer, J. D., Landen, O. L., Turner, R. E., Lasinski, B. F., Hammer, J. H., Rosen, M. D., Suter, L. J., and Hsing, W. H., *Detailed Measurements of a Diffusive Supersonic Wave in a Radiatively Heated Foam*, Lawrence Livermore National Laboratory, Livermore, CA, UCRL-JC-135062; also in *Phys. Rev. Lett*. **84**(2), 274–277 (2000).

Back, C. A., Grun, J., Decker, C. D., Davis, J., Laming, M., Feldman, U., Landen, O. L., Suter, L. J., Miller, M., Serduke, F., and Wuest, C., *X-Ray Sources Generated from Gas-Filled Laser-Heated Targets*, Lawrence Livermore National Laboratory, Livermore, CA, UCRL-JC-138111-ABS. Prepared for *12th American Physical Society Topical Conf on Atomic Processes in Plasma*, Reno, NV, Mar 19–24, 2000.

Baker, K. L., Drake, R. ., Estabrook, K. G., Sleaford, B., Prasad, M. K., La Fontaine, B., and Villeneuve, D. M., "Measurement of the Frequency and Spectral Width of the Langmuir Wave Spectrum Driven by Stimulated Raman Scattering," *Phys. Plasmas* **6**(11), 4284–4292 (1999).

Banks, P. S., Dinh, L., Stuart, B. C., Feit, M. D., Komashko, A. M., Rubenchik, A. M., Perry, M. D., and McLean, W., *Short-Pulse Laser Deposition of Diamond-Like Carbon Thin Films,* Lawrence Livermore National Laboratory, CA, UCRL-JC-134974; also in *Appl. Phys. A* **69**(SUPPS), S347–S353.

Banks, P. S., Feit, M. D., Rubenchik, A. M., Stuart, B. C., and Perry, M. D., *Material Effects in Ultra-Short Pulse Laser Drilling of Metals,* Lawrence Livermore National Laboratory, CA, UCRL-JC-133743; also in *Appl. Phys. A* **69** (SUPPS), S377–S380 (1999).

Bayramian, A. J., Bibeau, C., Schaffers, K. I., Marshall, C. D., and Payne, S. A., *Gain Saturation Measurements of Ytterbium-Doped $Sr_5(PO_4)_3F$*, Lawrence Livermore National Laboratory, Livermore, CA, UCRL-JC-133980; also in *Appl. Optics* **39**(6), 982–985 (2000).

Berger, R. L., Divol, L., Hinkel, D. E., Kirkwood, R. K., Glenzer, S., Langdon, A. B., Moody, J. D., Still, C. H., Suter, L., Williams, E. A., and Young, P E., *Modeling the Backscatter and Transmitted Light Spectra of High Power Smoothed Beams with pF3D, a Massively Parallel Laser Plasma Interaction Code*, Lawrence Livermore National Laboratory, Livermore, CA, UCRL-JC-137900-ABS. Prepared for *26th European Conf on Laser Interaction with Matter*, Prague, Czech Republic, Jun 12–16, 2000.

Berger, R. L., Langdon, A. B., Hinkel, D. E., Still, C. H., and Williams, E. A., *Influence of Nonlocal Electron Heat Conduction on the Induced Incoherence of Light Transmitted through Plasma,* Lawrence Livermore National Laboratory, Livermore, CA, UCRL-JC-136373. Submitted to *Phys. Rev. Lett*.

Bernat, T., Nobile, A., and Schultz, K., *Fabrication of Indirect Drive Ignition Targets for the NIF: Recent Developments*, Lawrence Livermore National Laboratory, Livermore, CA, UCRL-JC-138259-ABS. Prepared for *18th IAEA Fusion Energy Conf*, Sorrento, Italy, Oct 4–10, 2000.

Boehly, T. R., Bradley, D. K., Fisher, Y., Meyerhofer, D. D., Seka, W., and Soures, J. M., *Effects of Optical Prepulse on Direct-Drive Inertial Confinement Fusion Target Performance*, Lawrence Livermore National Laboratory, Livermore, CA, UCRL-JC-137876. Submitted to *Phys. Plasmas.*

Bradley, D. K., Bell, P. M., Dymoke-Bradshaw, A. K. L., Hares, J. D., and Bahr, R., *Development and Characterization of a Single Line of Sight Framing Camera*, Lawrence Livermore National Laboratory, Livermore, CA, UCRL-JC-138002-ABS. Prepared for *High Temperature Diagnostics Mtg*, Tucson, AZ, Jun 18–22, 2000.

Bryant, R., *NIF ICCS Network Design and Loading Analysis*, Lawrence Livermore National Laboratory, Livermore, CA, UCRL-ID-135920.

Bullock, A. B., Landen, O. L., and Bradley, D. K., *10 m and 5 m Pinhole-Assisted Point-Projection Backlit Imaging for NIF*, Lawrence Livermore National Laboratory, Livermore, CA, UCRL-JC-137904-ABS. Prepared for *High Temperature Diagnostics Mtg*, Tuscon, AZ, Jun 18–22, 2000.

Bullock, A. B., Landen, O. L., and Bradley, D. K., *Relative X-Ray Backlighter Intensity Comparison of Ti and Ti/Sc Combination Foils Driven in Double-Sided and Single-Sided Laser Configuration*, Lawrence Livermore National Laboratory, Livermore, CA, UCRL-JC-137906-ABS. Prepared for *High Temperature Diagnostics Mtg*, Tuscon, AZ, Jun 18–22, 2000.

Burnham, A., Runkel, M., Demos, S., Kozlowski, M., and Wegner, P., *Effect of Vacuum on the Occurrence of UV-Induced Surface Photoluminescence, Transmission Loss, and Catastrophic Surface Damage*, Lawrence Livermore National Laboratory, Livermore, CA, UCRL-JC-137123-ABS. Prepared for *Society of Photo-Optical Instrumentation Engineers 45th Annual Mtg*, San Diego, CA, Jul 30–Aug 4, 2000.

C

Campbell, J. H., and Suratwala, T. I., *Nd-Doped Phosphate Glasses for High-Energy/High-Peak-Power Lasers*, Lawrence Livermore National Laboratory, Livermore, CA, UCRL-JC-132911 Rev 1; also in *J. Non-Cryst. Solids* **263**(1-4), 318–341 (2000).

Campbell, J. H., Suratwala, T. I., Thorsness, C. B., Hayden, J. S., Thorne, A. J., Cimino, J. M., Marker, A. J., Takeuchi, K., Smolley, M., and Ficini-Dorn, G. F., *Continuous Melting of Phosphate Laser Glass*, Lawrence Livermore National Laboratory, Livermore, CA, UCRL-JC-134194; also in *J. Non-Cryst. Solids* **263**(1-4), 342–357 (2000).

Cauble, R., Remington, B. A., and Campbell, E. M., *Laboratory Measurements of Materials in Extreme Conditions: The Use of High Energy Radiation Sources for High Pressure Studies*, Lawrence Livermore National Laboratory, CA, UCRL-JC-131079; also in *J. Impact Engr.* **23**(1) Pt.1, 87–99 (1999).

Celliers, P. M., Collins, G. W., Da Silva, L. B., Cauble, R., Moon, S. J., Wallace, B. A., Hammel, B. A., and Hsing, W. W., *Multiple-Shock Compression of Liquid Deuterium*, Lawrence Livermore National Laboratory, Livermore, CA, UCRL-JC-136861 ABS. Prepared for *American Physical Society March Mtg*, Minneapolis, MN, Mar 20, 2000.

Cherfils, C., Glendinning, S. G., Galmiche, D., Remington, B. A., Richard, A. L., Haan, S., Wallace, R., Dague, N., and Kalantar, D. H., *Convergent Rayleigh–Taylor Experiments on the Nova Laser*, Lawrence Livermore National Laboratory, CA, UCRL-JC-135371; also in *Phys. Rev. Lett.* **83** (26), 5507–5510 (1999).

Collins, G. W., Bradley, D. K., Celliers, P., Silva, L. B., Cauble, R., Moon, S. J., Hammel, B. A., Wallace, R. J., Koenig, M., and Benuzzi-Mounaix, A., *Shock Compressing H_2O into an Electronic Conductor*, Lawrence Livermore National Laboratory, Livermore, CA, UCRL-JC-136738 ABS. Prepared for *American Physical Society March Mtg*, Minneapolis, MN, Mar 20, 2000.

Colvin, J. D., Remington, B. A., Kalantar, D. H., and Weber, S. V., *Experimental Evidence for Shock Softening and Hardening of Metals at High Strain Rate,* Lawrence Livermore National Laboratory, Livermore, CA, UCRL-JC-136707. Submitted to *Phys. Rev. Lett.*

Cook, R., *Models of Polyimide Spray Coatings*, Lawrence Livermore National Laboratory, Livermore, CA, UCRL-JC-136289. Submitted to *Fusion Technol.*

Crichton, S. N., Tomozawa, M., Hayden, J. S., Suratwala, T. I., and Campbell, J. H., *Subcritical Crack Growth in a Phosphate Laser Glass*, Lawrence Livermore National Laboratory, CA, UCRL-JC-131864; also in *J. Am. Ceramic. Soc.* **82**(11), 3097–3104 (1999).

D

Dattolo, E., Suter, L., Monteil, M.-C., Jadaud, J.-P., Dague, N., Glenzer, S., Turner, R., Juraszek, D., Lasinski, B., Decker, C., Landen, O., and MacGowan, B., *Status of Our Understanding and Modeling of X-Ray Coupling Efficiency in Laser Heated Hohlraums*, Lawrence Livermore National Laboratory, Livermore, CA, UCRL-JC-137622. Submitted to *Phys. Plasmas*.

Delage, O., Lerche, R. A., Sangster, T. C., and Arsenault, H. H., *SIRINC: a Code for Assessing and Optimizing the Neutron Imaging Diagnostic Capabilities in ICF Experiments*, Lawrence Livermore National Laboratory, Livermore, CA, UCRL-JC-137922-ABS. Prepared for *13th Topical Conf on High-Temperature Plasma Diagnostics*, Tucson, AZ, Jun 18–22, 2000.

E

Eder, D. C., Pretzler, G., Fill, E., Eidmann, K., and Saemann, A., *Spatial Characteristics of K Radiation from Weakly Relativistic Laser Plasmas*, Lawrence Livermore National Laboratory, Livermore, CA, UCRL-JC-133236; also in *Appl. Phys. B* **70**(2), 211–217 (2000).

Edwards, J., Glendinning, S. G., Suter, L. J., Remington, B. A., Landen, O., Turner, R. E., Shepard, T. J., Lasinski, B., Budil, K., Robey, H., Kane, J., Lewis, H., Wallace, R., Graham, P., Dunne, M., and Thomas, B. R., *Turbulent Hydrodynamic Experiments Using a New Plasma Piston*, Lawrence Livermore National Laboratory, Livermore, CA, UCRL-JC-136317-REV-2; also in *Phys. Plasmas* **7**(5), 2099–2107 (2000).

Ehrmann, P. R., Campbell, J. H., Suratwala, T. I., Hayden, J. S., Krashkevich, D., Takeuchi, K., *Optical Loss and Nd^{3+} Non-Radiative Relaxation by Cu, Fe and Several Rare Earth Impurities in Phoshate Laser Glasses,* Lawrence Livermore National Laboratory, Livermore, CA, UCRL-JC-132910 Rev 1; also in *J. Non-Cryst. Solids* **263**(1-4), 251–262 (2000).

G

Glendinning, S. G., Cherfils, C., Colvin, J., Divol, L., Galmiche, D., Haan, S., Marinak, M. M., Remington, B. A., Richard, A. L., and Wallace, R., *Ablation Front Rayleigh–Taylor Growth Experiments in Spherically Convergent Geometry*, Lawrence Livermore National Laboratory, Livermore, CA, UCRL-JC-134966. Prepared for *41st Annual Mtg of the Div of Plasma Phyics*, Seattle, WA, Nov 15, 1999.

Glenzer, S. H., Berger, R. L., Divol, L. M., Kirkwood, R. K., MacGowan, B. J., Moody, J. D., Rothenberg, J. E., Suter, L. J., and Williams, E. A., *Laser–Plasma Interactions in Inertial Confinement Fusion Hohlraums,* Lawrence Livermore National Laboratory, Livermore, CA, UCRL-JC-136632. Submitted to *Phys. Rev. Lett*.

Glenzer, S. H., Chambers, D., Wolfrum, E., Wark, J., and Young, P. E., *Thomson Scattering on Astrophysical Plasmas*, Lawrence Livermore National Laboratory, Livermore, CA, UCRL-JC-137687-ABS. Prepared for *3rd Intl Conf on Laboratory Astrophysics with Intense Laser*, Houston, TX, Mar 30–Apr 1, 2000.

Glenzer, S. H., Fournier, K. B., Decker, C., Hammel, B. A., Lee, R. W., Lours, L., MacGowan, B. J., and Osterheld, A. L., *Accuracy of K-Shell Spectra Modeling in High-Density Plasmas,* Lawrence Livermore National Laboratory, Livermore, CA, UCRL-JC-137905. Submitted to *Phys. Rev. E*.

Glenzer, S. H., Fournier, K. B., Hammel, B. A., Lee, R. W., MacGowan, B. J., and Wilson, B. G., *Accuracy of X-Ray Spectra Modeling for Inertial Confinement Fusion Plasmas*, Lawrence Livermore National Laboratory, Livermore, CA, UCRL-JC-137557-ABS. Prepared for *12th American Physical Society Topical Conf on Atomic Processes in Plasmas,* Reno, NV, Mar 19–23, 2000.

Glenzer, S. H., Suter, L. J., Berger, R. L., Estabrook, K. G., Hammel, B. A., Kauffman, R. L., Kirkwood, R. K., MacGowan, B. J., Moody, J. D., and Rothenberg, J. E., *Holhraum Energetics with Smoothed Laser Beams,* Lawrence Livermore National Laboratory, Livermore, CA, UCRL-JC-136356. Submitted to *Contrib. Plasma Phys.*

Goldman, S. R., Barnes, C. W., Caldwell, S. E., Wilson, D. C., Batha, S. H., Grove, J. W., Gittings, M. L., Hsing, W. W., Kares, R. J., Klare, K. A., Kyrala, G. A., Margevicius, R. W., Weaver, R. P., Wilke, M. D., Dunne, A. M., Edwards, M. J., Graham, P., and Thomas, B. R., *Production of Enhanced Pressure Regions due to Inhomogeneities in Inertial Confinement Fusion Targets*, Lawrence Livermore National Laboratory, Livermore, CA, UCRL-JC-137588. Submitted to *Phys. Plasmas.*

Goldman, S. R., Caldwell, S. E., Wilke, M. D., Wilson, D. C., Barnes, C. W., Hsing, W. W., Delamater, N. D., Schappert, G. T., Grove, J. W., Lindman, E. L., Wallace, J. M., Weaver, R. P., Dunne, A. M., Edwards, M. J., Graham, P., and Thomas, B. R., *Shock Structuring due to Fabrication Joints in Targets*, Lawrence Livermore National Laboratory, Livermore, CA, UCRL-JC-137462. Submitted to *Phys. Plasmas.*

H

Haan, S. W., Dittrich, T. R., Marinak, M. M., and Hinkel, D. E., *Design of Ignition Targets for the National Ignition Facility,* Lawrence Livermore National Laboratory, Livermore, CA, UCRL-JC-133510. Prepared for *1st Intl Conf on Inertial Fusion Sciences and Applications,* Bordeaux, France, Sep 12, 1999.

Haan, S. W., Dittrich, T., Hinkel, D., Marinak, M., Munro, D., Strobel, G., Suter, L., Pollaine, S., Jones, O., and Lindl, J., *Hydrodynamic Instabilities and Thermonuclear Ignition on the National Ignition Facility*, Lawrence Livermore National Laboratory, Livermore, CA, UCRL-JC-137000-ABS. Prepared for *American Physical Society April Mtg 2000*, Long Beach, CA, Apr 29–May 2, 2000.

Haber, I., Callahan, D. A., Friedman, A., Grote, D. P., and Langdon, A. B., *Transverse-Longitudinal Temperature Equilibration in a Long Uniform Beam*, Lawrence Livermore National Laboratory, Livermore, CA, UCRL-JC-136630. Prepared for *Inst of Electrical and Electronics Engineers, Inc. Particle Accelerator Conf*, Dallas, TX, May 1, 1995.

Hammel, B. A., *Recent Advances in Indirect Drive ICF Target Physics*, Lawrence Livermore National Laboratory, Livermore, CA, UCRL-JC-138130-ABS. Prepared for *18th Fusion Energy Conf*, Sorrento, Italy, Oct 4–10, 2000.

Hartemann, F. V., Landahl, E. C., Troha, A. L., Van Meter, J. R., Baldis, H. A., Freeman, R. R., Luhman, N. C., Song, L., Kerman, A. K., and Yu, D. U. L., *The Chirped-Pulse Inverse Free-Electron Laser: A High-Gradient Vacuum Laser Accelerator*, Lawrence Livermore National Laboratory, CA, UCRL-JC-134073; also in *Phys. Plasmas* **6**(10), 4104–4110 (1999).

Hatchett, S. P., Brown, C. G., Cowan, T. E., Henry, E. A., Johnson, J., Key, M. H., Koch, J. A., Langdon, A. B., Lasinski, B. F., and Lee, R. W., *Electron, Photon, and Ion Beams from the Relativistic Interaction of Petawatt Laser Pulses with Solid Targets*, Lawrence Livermore National Laboratory, Livermore, CA, UCRL-JC-135029. Prepared for *41st Annual Mtg of the Div of Plasma Physics*, Seattle, WA, Nov 15, 1999.

Hawley-Fedder, R., Robey, H., Biesiada, T., DeHaven, M., Floyd, R., and Burnham, A., *Rapid Growth of Very Large KDP and KD*P Crystals in Support of the National Ignition Facility*, Lawrence Livermore National Laboratory, Livermore, CA, UCRL-JC-137102-ABS. Prepared for *Society of Photo-Optical Instrumentation Engineers 45th Annual Mtg*, San Diego, CA, Jul 30–Aug 4, 2000.

Hayden, J. S., Marker, A. J., Suratwala, T. I., and Campbell, J. H., *Surface Tensile Layer Generation during Thermal Annealing of Phosphate Glass*, Lawrence Livermore National Laboratory, Livermore, CA, UCRL-JC-134690; also in *J. Non-Cryst. Solids* **263**(1-4), 228–239 (2000).

Hayden, J. S., Tomozawa, M., and Crichton, S., *OH Diffusion Measurements in Phosphate Laser Glasses*, Lawrence Livermore National Laboratory, Livermore, CA, UCRL-ID-136007.

Hicks, D. G., Li, C. K., Seguin, F. H., Ram , A. K., Petrasso, R. D., Soures, J. M., Meyerhofer, D. D., Roberts, S., Schnittman, J. D., and Sorce, C., *Studies of MeV Fast Protons Produced in Laser Fusion Experiments*, Lawrence Livermore National Laboratory, Livermore, CA, UCRL-JC-136746. Submitted to *Phys. Rev. Lett.*

Hinkel, D. E., Haan, S. W., Pollaine, S. M., Dittrich, T. R., Jones, O. S., Suter, L. J., and Langdon, A. B., *Scaled Targets for the National Ignition Facility*, Lawrence Livermore National Laboratory, Livermore, CA, UCRL-JC-138284-ABS. Prepared for *30th Annual Anomalous Absorption Conf*, Ocean City, MD, May 21–26, 2000.

K

Kalantar, D. H., Belak, J., Colvin, J. D., Remington, B. A., Weber, S. V., Allen, A. M., Loveridge, A., Wark, J. S., Boehly, T. R., and Paisley, D., *Dynamic X-Ray Diffraction to Study Compression of Si and Cu beyond the Hugoniot Elastic Limit*, Lawrence Livermore National Laboratory, Livermore, CA, UCRL-JC-138108-ABS. Prepared for *High-Temperature Plasma Diagnostics Mtg*, Tucson, AZ, Jun 18–20, 2000.

Kalantar, D. H., Bell, P. M., Perry, T. S., Sewall, N., Diamond, C., Piston, K., *Optimizing Data Recording for the NIF Core Diagnostic X-Ray Streak Camera*, Lawrence Livermore National Laboratory, Livermore, CA, UCRL-JC-138107-ABS. Prepared for *High Temperature Plasma Diagnostics Mtg*, Tucson, AZ, Jun 18–20, 2000.

Kalantar, D. H., Remington, B. A., Chandler, E. A., Colvin, J. D., Gold, D. M., Mikaelian, K. O., Weber, S. V., Wiley, L. G., Wark, J. S., Hauer, A. A., and Meyers, M. A., *High Pressure Solid State Experiments on the Nova Laser*, Lawrence Livermore National Laboratory, CA, UCRL-JC-129810; also in *J. Impact Engr*. **23**(1) Pt. 1, 409–419 (1999).

Kalantar, D. H., Remington, B. A., Colvin, J. D., Mikaelian, K. O., Weber, S. V., Wiley, L. G., Wark, J. S., Loveridge, A., Allen, A. M., and Hauer, A., *Solid State Experiments at High Pressure and Strain Rates,* Lawrence Livermore National Laboratory, Livermore, CA, UCRL-JC-136355. Prepared for *41st Annual Mtg of the Div of Plasma Physics,* Seattle, WA, Nov 15, 1999.

Kauffman, R., *Inertial Confinement Fusion Monthly Highlights*, November 1999, Lawrence Livermore National Laboratory, Livermore, CA, UCRL-TB-128550-00-02.

Kauffman, R., *Inertial Confinement Fusion Monthly Highlights*, October 1999, Lawrence Livermore National Laboratory, Livermore, CA, UCRL-TB-128550-00-01.

Kauffman, R., *Inertial Confinement Fusion Monthly Highlights,* September 1999, Lawrence Livermore National Laboratory, Livermore, CA, UCRL-TB-128550-99-12.

Key, M. H., Campbell, E. M., Cowan, T. E., Hatchett, S. P., Henry, E. A., Koch, J. A., Langdon, A. B., Lasinski, B. F., Lee, R. W., and Mackinnon, A., *Studies of the Relativistic Electron Source and Related Phenomena in Petawatt Laser–Matter Interactions,* Lawrence Livermore National Laboratory, Livermore, CA, UCRL-JC-135477 Rev 1. Prepared for *1st Intl Conf on Inertial Fusion Sciences and Applications*, Bordeaux, France, Sept 12, 1999.

Kirkwood, R. K., Montgomery, D. S., Afeyan, B. B., Moody, J. D., MacGowan, B. J., Joshi, C., Wharton, K. B., Glenzer, S. H., Williams, E. A., Young, P. E., Kruer, W. L., Estabrook, K. G., and Berger, R. L., *Observation of the Nonlinear Saturation of Langmuir Waves Driven by Ponderomotive Force in a Large Scale Plasma*, Lawrence Livermore National Laboratory, Livermore, CA, UCRL-JC-128298; also in *Phys. Rev. Lett*. **83**(15), 2965–2968 (1999).

Koch, J. A., Presta, R., Sacks, R., Zacharias, R., Bliss, E., Dailey, M., Feldman, M., Grey, A., Holdener, F., and Salmon, T., *Experimental Comparison of a Shack-Hartmann Sensor and a Phase-Shifting Interferometer for Large-Optics Metrology Applications,* Lawrence Livermore National Laboratory, Livermore, CA, UCRL-JC-136743. Submitted to *Appl. Opt*.

Koch, J. A., Sater, J., Bernat, T., Bittner, D., Collins, G., Hammel, B., Lee, Y., and Mackinnon, A., *Quantitative Analysis of Backlit Shadowgraphy as a Diagnostic of Hydrogen Ice Surface Quality in ICF Capsules,* Lawrence Livermore National Laboratory, Livermore, CA, UCRL-JC-136266. Prepared for *13th Target Fabrication Mtg,* Catalina Island, CA, Nov 8, 1999.

Koch, J., *X-Ray Interferometry with Spherically Bent Crystals*, Lawrence Livermore National Laboratory, Livermore, CA, UCRL-JC-138023-ABS. Prepared for *13th Topical Conf on High-Temperature Plasma Diagnostics*, Tucson, AZ, Jun 18–22, 2000.

Komashko, A. M., Feit, M. D., Rubenchik, A. M., Perry, M. D., and Banks, P. S., *Simulation of Material Removal Efficiency with Ultrashort Laser Pulses,* Lawrence Livermore National Laboratory, CA, UCRL-JC-133744; also in *Appl. Phys. A* **69**(SUPPS), S95–S98 (1999).

Kozlowski, M. R., Battersby, C. L., and Demos, S. G., *Luminescence Investigation of SiO_2 Surfaces Damaged by 0.35 mm Laser Illumination,* Lawrence Livermore National Laboratory, Livermore, CA, UCRL-JC-136870. Prepared for *31st Annual Symp on Optical Materials for High Power Lasers,* Boulder, CO, Oct 4, 1999.

L

Landahl, E. C., Hartemann, F. V., Le Sage, G. P., White, W. E., Baldis, H. A., Bennnett, C. V., Heritage, J. P., Kolner, B. H., Luhman, N. C., and Ho, C. H., *Phase Noise Reduction and Photoelectron Acceleration in a High-Q RF Gun*, Lawrence Livermore National Laboratory, CA, UCRL-JC-139029; also in *IEEE Trans. Plasma Sci.* **27**(5), 1547 (1999).

Landen, O. L., Amendt, P. A., Back, C. A., Berger, R. L., Bradley, D. K., Bullock, A. B., Cauble, R. C., Chandler, G. A., Collins, G. W., Decker, C. D., Edwards, M. J., Glendinning, S. G., Glenzer, S. H., Haan, S. W., Kalantar, D. H., Kirkwoood, R. K., Moody, J. M., Munro, D. H., Olson, R. E., Perry, T. S., Pollaine, S. M., Remington, B. A., Robey, H. R., Sanchez, J., Suter, L. J., Turner, R. E., Young, P. E., Wallace, R. J., Hammel, B. A., and Hsing, W. W., *Recent Progress in ICF and High Energy Density Experiments*, Lawrence Livermore National Laboratory, Livermore, CA, UCRL-JC-138000-ABS. Prepared for *26th European Conf on Laser Interaction with Matter*, Prague, Czech Republic, Jun 12–16, 2000.

Landen, O. L., and Glenzer, S. H., *Warm, Dense Matter Characterization by X-Ray Thomson Scattering*, Lawrence Livermore National Laboratory, Livermore, CA, UCRL-JC-138258-ABS. Prepared for *Intl Workshop on Warm Dense Matter*, Vancouver, Canada, May 29–31, 2000.

Landen, O. L., Bradley, D. K., Amendt, P. A., Pollaine, S. M., Glendinning, S. G., Bullock, A. B., Turner, R. E., Suter, L. J., Jones, O. S., Wallace, R. J., and Hammel, B. A., *Symmetry Diagnosis and Control for NIF-Scale Hohlraums*, Lawrence Livermore National Laboratory, Livermore, CA, UCRL-JC-137874-ABS. Prepared for *26th European Conf on Laser Interaction with Matter*, Prague, Czech Republic, Jun 12–16, 2000.

Landen, O. L., Bradley, D. K., Pollaine, S. M., Amendt, P. A., Glendinning, S. G., Suter, L. J., Turner, R. E., Wallace, R. J., Hammel, B. A., and Delamater, N. D., *Indirect-Drive Time-Dependent Symmetry Diagnosis at NIF-Scale,* Lawrence Livermore National Laboratory, Livermore, CA, UCRL-JC-136297. Prepared for *1st Intl Conf on Inertial Fusion Sciences and Applications,* Bordeaux, France, Sep 12, 1999.

Landen, O. L., Ze, F., Lobban, A., Tutt, T., Bell, P. M., and Costa, R., *Angular Sensitivity of Gated Micro-Channel Plate Framing Cameras*, Lawrence Livermore National Laboratory, Livermore, CA, UCRL-JC-137879-ABS. Prepared for *13th Topical Conf on High-Temperature Plasma Diagnostics*, Tucson, AZ, Jun 18–22, 2000.

Langdon, A. B., Berger, R. L., Cohen, B. I., Decker, C. D., Hinkel, D. E., Kirkwood, R. K., Still, C. H., and Williams, E. A., *Power Transfer between Smoothed Laser Beams*, Lawrence Livermore National Laboratory, Livermore, CA, UCRL-JC-138282-ABS. Prepared for *30th Annual Anomalous Absorption Conf*, Ocean City, MD, May 21–26, 2000.

Lehmberg, R. H., and Rothenberg, J. E., "Comparison of Optical Beam Smoothing Techniques for Inertial Confinement Fusion and Improvement of Smoothing by the Use of Zero-Correlation Masks," *J. Appl. Phys.* **87**(3), 1012–1022 (2000).

Lukasheva, N. V., Niemela, S., Neelov, I. M., Darinskii, A. A., Sundholm, F., and Cook, R., *Conformational Variability of Helix Sense Reversals in Poly(Methly Isocyanates)*, Lawrence Livermore National Laboratory, Livermore, CA, UCRL-JC-137206. Submitted to *Macromolecules*.

M

McCallen, D., *Acceleration Amplifications in NIF Structures Subjected to Earthquake Base Motions,* Lawrence Livermore National Laboratory, Livermore, CA, UCRL-ID-136812.

McKinnon, A., Shigemori, K., Ditmire, T., Remington, B. A., Yanovsky, V., Ryutov, D., Estabrook, K. G., Edwards, M. J., Keilty, K. A., and Liang, E., *Radiative Shock Experiments Relevant to Astrophysics*, Lawrence Livermore National Laboratory, Livermore, CA, UCRL-JC-137569-ABS. Prepared for *3rd Intl Conf on Laboratory Astrophysics on Intense Lasers*, Houston, TX, Mar 29–Apr 1, 2000.

Montgomery, D. S., Johnson, R. P., Cobble, J. A., Fernandez, J. C., Lindman, E. L., Rose, H. A., and Estabrook, K. G., "Characterization of Plasma and Laser Conditions for Single Hot Spot Experiments," *Laser and Particle Beams* **17**(3), 349–359 (1999).

Moody, J. D., MacGowan, B. J., Glenzer, S. H., Kirkwood, R. K., Kruer, W. L., Montgomery, D. S., Schmitt, A. J., Williams, E. A., and Stone, G. F., *Experimental Investigation of Short Scalelength Density Fluctuations in Laser-Produced Plasmas*, Lawrence Livermore National Laboratory, Livermore, CA, UCRL-JC-136401-REV-1. Prepared for *41st Annual Mtg of the Div of Plasma Physics*, Seattle, WA, Nov 15–19, 1999.

Murray, J. E., Milam, D., Boley, C. D., and Estabrook, K. G., *Spatial Filter Pinhole Development for the National Ignition Facility,* Lawrence Livermore National Laboratory, Livermore, CA, UCRL-JC-134647; also in *Appl. Optics* **39**(9), 1405–1420 (2000).

N

Noble, C. R., Hoehler, M. S., and Sommer, S. C., *NIF Ambient Vibration Measurements,* Lawrence Livermore National Laboratory, Livermore, CA, UCRL-ID-136914.

P

Perry, M. D., and Shore, B. W., *Petawatt Laser Report,* Lawrence Livermore National Laboratory, Livermore, CA, UCRL-ID-124933.

Pollaine, S., Bradley, D., Landen, O., Amendt, P., Jones, O., Wallace, R., Glendinning, G., Turner, R., and Suter, L., *P6 and P8 Modes in NIF Hohlraums*, Lawrence Livermore National Laboratory, Livermore, CA, UCRL-JC-133888-ABS. -REV-2. Prepared for *30th Annual Anomalous Absorption Conf*, Ocean City, MD, May 21–26, 2000.

Pollaine, S., *Radiation Transport between Two Concentric Spheres*, Lawrence Livermore National Laboratory, Livermore, CA, UCRL-JC-137279. Submitted to *Nuclear Fusion.*

R

Regan, S. P., Delettrez, J. A., Yaakobi, B., Bradley, D. K., Bahr, R., Millecchia, M., Meyerhofer, D. D., and Seka, W., *Spectroscopic Analysis of Electron Temperature in Laser Driven Burnthrough Experiments*, Lawrence Livermore National Laboratory, Livermore, CA, UCRL-JC-137875-ABS. Prepared for *12th Topical Conf on Atomic Processes in Plasmas*, Reno, NV, Mar 19–23, 2000.

Remington, B. A., Drake, R. P., Takabe, H., and Arnett, D., *Review of Astrophysics Experiments on Intense Lasers*, Lawrence Livermore National Laboratory, Livermore, CA, UCRL-JC-134961-REV-1. Prepared for *41st Annual Mtg of the Division of Plasma Physics*, Seattle, WA, Nov 15–19, 1999.

Remington, B. A., Kalantar, D. H., Weber, S. V., and Colvin, J. D., *Experimental Path to Deep Earth Interior Physics and Hypervelocity Micro-Flier Plates*, Lawrence Livermore National Laboratory, Livermore, CA, UCRL-JC-138109-ABS. Prepared for *3rd Intl Workshop on Laboratory Astrophysics on Intense Lasers*, Houston, TX, Mar 31–Apr 2, 2000.

Remington, B. A., *Overview of Astrophysics Experiments on Intense Lasers*, Lawrence Livermore National Laboratory, Livermore, CA, UCRL-JC-137570-ABS. Prepared for *3rd Intl Conf on Laboratory Astrophysics on Intense Lasers,* Houston, TX, Mar 29–Apr 1, 2000.

Richard, A. L., Jadaud, J. P., Dague, N., Monteil, M. C., Turner, R. E., Bradley, D., Wallace, R. J., Landen, O. L., Pien, G., Morse, S., and Soures, J. M., *Symmetry Experiments on OMEGA with LMJ like Multiple Beam Cones Irradiation*, Lawrence Livermore National Laboratory, Livermore, CA, UCRL-JC-137873-ABS. Prepared for *26th European Conf on Laser Interaction with Matter*, Prague, Czech Republic, Jun 12–16, 2000.

Roberts, C. C., Orthion, P. J., Hassel, A. E., Parrish, B. K., Buck ley, S. R., Fearon, E., Letts, S. A., and Cook, R. C., *Development of Polyimide Ablators for NIF: Defect Analysis, Novel Smoothing Technique and Upilex Coatings*, Lawrence Livermore National Laboratory, Livermore, CA, UCRL-JC-137737. Submitted to *Fusion Technol*.

Robey, H. F., Kane, J., Remington, B. A., Hurricane, O., Drake, R. P., and Knauer, J., *Astrophysics Experiments on the OMEGA Laser: Interface Coupling in Supernovae Caused by Rippled Shock Imprinting*, Lawrence Livermore National Laboratory, Livermore, CA, UCRL-JC-137443-ABS. Prepared for *3rd Intl Conf on Laboratory Astrophysics with Intense Lasers*, Houston, TX, Mar 30–Apr 1, 2000.

Roth, M., Cowan, T. E., Brown, C., Christl, M., Fountain, W., Hatchett, S., Johnson, J., Key, M. H., Pennington, D. M., and Perry, M. D., *Intense Ion Beams Accelerated by Petawatt-Class Lasers*, Lawrence Livermore National Laboratory, Livermore, CA, UCRL-JC-136218-ABS. Prepared for *13th Intl Symp on Heavy Ion Inertial Fusion*, San Diego, CA, Mar 13, 2000.

Ryutov, D. D., and Remington, B. A., *Destabilizing Effect of Thermal Conductivity on the Rayleigh–Taylor Instability*, Lawrence Livermore National Laboratory, Livermore, CA, UCRL-JC-137568-ABS. Prepared for *3rd Intl Conf on Laboratory Astrophysics with Intense Lasers*, Houston, TX, Mar 30–Apr 1, 2000.

Ryutov, D., Ditmire, T., Edwards, J., Glendinning, G., Remington, B., and Shigemori, K., *Simple Description of the Blast Wave in the Medium with Y Close to 1*, Lawrence Livermore National Laboratory, Livermore, CA, UCRL-JC-137567-ABS. Prepared for *3rd Intl Conf on Laboratory Astrophysics with Intense Lasers*, Houston, TX, Mar 30–Apr 1, 2000.

S

Sangster, T. C., Ahle, L. A., Halaxa, E. F., Karpenko, V. P., Olddaker, M. E., Thompson, J., Beck, D. N., Bieniosek, F. M., Henestroza, E., and Kwan, J. W., *New 500-keV Ion Source Test Stand for HIF*, Lawrence Livermore National Laboratory, Livermore, CA, UCRL-JC-136744-ABS. Prepared for *13th Intl Symp on Heavy Ion Inertial Fusion*, San Diego, CA, Mar 13, 2000.

Sangster, T. C., Glebov, V., Lerche, R. A., Phillips, T. W., Stoekl, C., Padalino, S. J., Olliver, H., and Thompson, S., *Calibration of the Medusa Neutron Spectrometer at the OMEGA Laser*, Lawrence Livermore National Laboratory, Livermore, CA, UCRL-JC-137923-ABS. Prepared for *13th Topical Conf on High-Temperature Plasma Diagnostics*, Tucson, AZ, Jun 18–22, 2000.

Sharp, R., and Runkel, M., *Automated Damage Onset Analysis Techniques Applied to KDP Damage and the Zeus Small Area Damage Test Facility*, Lawrence Livermore National Laboratory, Livermore, CA, UCRL-JC-134765. Prepared for *31st Boulder Damage Symposium: Annual Symposium on Optical Materials for High Power Lasers*, Boulder, CO, Oct 4–7, 1999.

Still, C. H., Berger, R. L., and Langdon, A. B., *pF3D, version 2.0*, Lawrence Livermore National Laboratory, Livermore, CA, UCRL-CODE-2000-019.

Still, C. H., Berger, R. L., Langdon, A. B., Hinkel, D. E., and Williams, E. A., *Filamentation and Forward Brillouin Scatter of Entire Smoothed and Aberrated Laser Beams*, Lawrence Livermore National Laboratory, Livermore, CA, UCRL-JC-135006. Prepared for *41st Annual Mtg of the Div of Plasma Physics*, Seattle, WA, Nov 15, 1999.

Still, C. H., Berger, R. L., Langdon, A. B., Hinkel, D. E., and Williams, E. A., *Laser Plasma Simulations Using Entire Smoothed and Aberrated Laser Beams*, Lawrence Livermore National Laboratory, Livermore, CA, UCRL-JC-138283-ABS. Prepared for *30th Annual Anomalous Absorption Conf*, Ocean City, MD, May 21–26, 2000.

Strobel, G. L., *M Dependence of Surface Expansion Coefficients*, Lawrence Livermore National Laboratory, Livermore, CA, UCRL-JC-137516-ABS. Prepared for *Sherwood 2000*, Los Angeles, CA, Mar 27–29, 2000.

Suratwala, T. I., Steele, R. A., Wilke, G. D., Campbell, J. H., and Takeuchi, K., *Effects of OH Content, Water Vapor Pressure, and Temperature on Sub-Critical Crack Growth in Phosphate Glass*, Lawrence Livermore National Laboratory, Livermore, CA, UCRL-JC-132912; also in *J. Non-Cryst. Solids* **263**(1-4), 213–227 (2000).

Suter, L., Rothenberg, J., Munro, D., Van Wonterghem, B., Haan, S., and Lindl, J., *Feasibility of High Yield/High Gain NIF Capsules,* Lawrence Livermore National Laboratory, Livermore, CA, UCRL-JC-136784. Prepared for *1st Intl Conf on Inertial Fusion Sciences and Applications,* Bordeaux, France, Sep 18, 1999.

Suter, L., Rothenberg, J., Munro, D., Van Wonterghem, B., and Haan, S., *Exploring the Limits of the National Ignition Facility's Capsule Coupling*, Lawrence Livermore National Laboratory, Livermore, CA, UCRL-JC-136319-REV-1; also in *Phys. Plasmas* **7**(5), 2092–2098 (2000).

T

Takagi, M., Cook, R., Stephens, R., Gibson, J., and Paguio, S., *Decreasing Out-of-Round in P MS Mandrels by Increasing Interfacial Tension*, Lawrence Livermore National Laboratory, Livermore, CA, UCRL-JC-135539. Submitted to *Fusion Technol*.

Takagi, M., Cook, R., Stephens, R., Gibson, J., and Paguio, S., *Effects of Controlling Osmotic Pressure on a P MS Microencapsulated Shell during Curing*, Lawrence Livermore National Laboratory, Livermore, CA, UCRL-JC-135540. Submitted to *Fusion Technol*.

Takagi, M., Cook, R., Stephens, R., Gibson, J., and Paguio, S., *Stiffening of P MS Mandrels during Curing*, Lawrence Livermore National Laboratory, Livermore, CA, UCRL-JC-135545. Submitted to *Fusion Technol*.

Turner, R. E., Landen, O. L., Bradley, D. K., Bell, P. M., Costa, R., Moody, J. D., and Lee, D., *Comparison of CCD vs Film Readouts for Gated MCP Cameras*, Lawrence Livermore National Laboratory, Livermore, CA, UCRL-JC-138003-ABS. Prepared for *High-Temperature Diagnostics Mtg,* Tucson, AZ, Jun 18–22, 2000.

W

Warwick, P. J., Demir, A., Kalantar, D. H., Key, M. H., Kim, N. S., Lewis, C. L. S., Lin, J., MacPhee, A. G., Neely, D., and Remington, B. A., *Radiography Measurements of Direct Drive Imprint in Thin Al Foils Using a Bright XUV Laser,* Lawrence Livermore National Laboratory, Livermore, CA, UCRL-JC-136395. Prepared for *5th Intl Conf on X-Ray Lasers,* Lund, Sweden, Jun 10, 1996.

Williams, W., *NIF Large Optics Metrology Software; Description and Algorithms*, Lawrence Livermore National Laboratory, Livermore, CA, UCRL-MA-137950.

Wolfrum, E., Allen, A., Barbee, T. W., Jr., Burnett, P., Djaoui, A., Kalantar, D., Keenan, R., Key, M. H., Lewis, C. L. S., Machacek, A., Remington, B., Rose, S. J., O'Rourke, R., and Wark, J. S., *Measurements of the XUV Opacity of a Strongly-Coupled Aluminum Plasma*, Lawrence Livermore National Laboratory, Livermore, CA, UCRL-JC-137262. Submitted to *Phys. Rev. Lett*.

Wu, Z. L., Stolz, C. J., Weakley, S. C., Hughes, J. D., and Zhao, Q., *Damage Threshold Prediction of Hafnia/Silica Multilayer Coatings by Nondestructive Evaluation of Fluence-Limiting Defects*, Lawrence Livermore National Laboratory, Livermore, CA, UCRL-JC-137089. Submitted to *Appl. Opt*.

Y

Yatsenko, L. P., Shore, B. W., Halfmann, T., Bergmann, K., and Vardi, A., "Source of Metastable H(2*s*) Atoms Using the Stark Chirped Rapid-Adiabatic-Passage Technique," *Phys. Rev. A* **60**(6), R4237–4240 (1999).

ICF/NIF and HEDES Program
Lawrence Livermore National Laboratory
P.O. Box 808, L-475
Livermore, California 94551

Address Correction Requested